Development of a THGEM Imaging Detector with Delay Line Readout

DEVELOPMENT OF A THGEM IMAGING DETECTOR WITH DELAY LINE READOUT

BY

ANDREI R. HANU, B.Sc.

A THESIS

SUBMITTED TO THE SCHOOL OF GRADUATE STUDIES

OF MCMASTER UNIVERSITY

IN PARTIAL FULFILMENT OF THE REQUIREMENTS

FOR THE DEGREE

DOCTOR OF PHILOSOPHY

McMaster University

DOCTOR OF PHILOSOPHY (2013) McMaster University

(MEDICAL PHYSICS) Hamilton, Ontario

TITLE:	Development of a THGEM Imaging Detector with Delay Line Readout
AUTHOR:	Andrei R. Hanu B.Sc., (Medical Physics & Applied Radiation Science) McMaster University, Hamilton, Canada
SUPERVISOR:	Dr. Soo-Hyun Byun
NUMBER OF PAGES:	xvi, 160

I dedicate this thesis in honour of

my mother, ***Mihaela Hanu****, and father,* ***Marin Hanu****.*

Had it not been for the sacrifices you made to come to this wonderful country, I would not be where I am today. For this, I am forever thankful.

Thank You!

Abstract

Position sensitive detectors represent a class of particle detectors widely used in high-energy physics, astrophysics, biophysics and medicine for imaging the spatial distribution of various radioactive sources. In recent years, a new class of gas based detectors, so-called micropattern gas detectors (MPGDs), has emerged. While modern MPGDs rival solid state detectors in terms of spatial and temporal resolution, their cost of production is significantly lower. A Thick Gaseous Electron Multiplier (THGEM) imaging detector, with a two-dimensional delay line readout, has been constructed as a concept for a large area imaging detector with reasonable spatial resolution. The delay line based THGEM imaging detector is robust, easy to manufacture and cost effective alternative to direct readout techniques which frequently employ a large number of channels. Featuring an active area of 40 x 40 mm^2, the prototype has been constructed using two 0.4 mm THGEMs and successfully operated in a low pressure, propane based, gas mixture. Two sets of orthogonal electrodes, connected to individual delay lines, serve as a two-dimensional anode readout. Adjacent electrodes are separated by approximately 3.4 ns of time delay and allow the interaction position to be calculated by measuring the time difference between delay line output signals corresponding to a common axis. Using modern field programmable gate arrays (FPGAs), a time-to-digital (TDC) data acquisition (DAQ) system has been developed. The TDC DAQ performs the position reconstruction algorithm and is capable of continuous event rates up to 1.8 MHz. The imaging capabilities of the detector have been assessed using a collimated alpha source and a wide X-ray beam. Under these aforementioned conditions, the detector was able to successfully resolve 1 mm diameter holes spaced 3 mm apart. With higher operating pressures, and using Xenon based gas mixture, it is expected the imaging detector should achieve sub-mm spatial resolution. The investigations presented in this thesis serve as a framework for the development of future THGEM imaging detectors.

Acknowledgements

I would like to express my deepest gratitude to my supervisor, Dr. Soo-Hyun Byun, for making my graduate experience a pleasant one. Byun, your positive outlook motivated me to always find a solution even when it was not entirely obvious. Primarily, I appreciate your ability to support ideas which were clearly above my skill level but allowed me to reach my full potential. During the last few years, you were both a great supervisor and friend. Thank You!

To Dr. William V. Prestwich. Our discussions at tea time were not only a welcome break from research, but very often they resulted in some great ideas. Your always positive attitude is contagious and I hope to someday inspire future students the way you have inspired me. Thank You!

I would also like to thank my committee members, Dr. Troy Farncombe, Dr. Michael Farquharson and Dr. Hao Peng. Your input during our meetings was instrumental in helping me finish my doctoral studies.

I also received extensive help and knowledge transfer from Kenrick Chin. Thank you for always having the patience to deal with me during the seemingly endless number of times I opened your door asking if you had a few minutes. Your extensive knowledge of electronics is surely the reason I was able to build some of the things described in this thesis. Thank you for motivating me to experiment with electronics.

During the last five years, I was fortunate enough to share my time at McMaster with some wonderful friends and colleagues. Among them are Witold Matysiak, Gloria Orchard, Arjit Baghwala, Hedieh Mohseni, Michelle Le, Farshad Mostafaei, Eric Johnston, Elstan Desouza, Justin Bennett, Zahra Anjomani, Sahar Darvish Molla and many more. Graduate school would've been a lonely experience without you guys. Thanks for sharing this time with me! I would also like to thank the ladies in the Medical Physics office. From undergrad to grad school, you guys have provided me with almost a decade of laugher and happy faces. Thank You!

To my friends who have stuck by me all of these years: Eric Cicero, Michael De Rubeis and Zach MacLellan. Thank you for keeping me grounded. A special thank you to Zach for giving me the moral support I needed during my comprehensive exam.

To my parents and family. Thank you for being the support I needed to pursue these studies. Mom, thank you for not allowing me to be a chemist and helping me

discover the medical physics program. Dad, thank you for always pushing me to be better and never allowing me to settle for just good enough. What I have achieved thus far is without a doubt due to the loving care you have shown me. Your hard work, and integrity, is something I will continue to strive for. My accomplishments during these last few years wouldn't have been possible without the foundation you guys have instilled in me. Jürgen, no amount of adjectives can describe the influence you've had on my life. Thank you for introducing me to the freedom of flying and I certainly hope that one day, when I let go of my steering wheel, the car will drive itself to the nearest airport. Felicia, thank you for being the best aunt ever and a source of emotional support. Alex, you have been the best cousin I could ask for. I wish you blue skies and fair winds. You have a bright future ahead of you.

To my best friend and co-pilot in life, Christine, who somehow always managed to see the best in me. Your continuous love and support reminds me of how lucky we are to be together and that I would not be where I am today without you. I strongly believe my graduate experience has been a positive one because I was able to share it with you and hope to return the favour as you finish your studies. Finally, I would like to thank my furry best friend, Ollie, for being my outlet to the outside world as I wrote this thesis. He won't be able to read this anyway, so I'll just give him a hug.

Abbreviations and Symbols

CFD	Constant Fraction Discriminator
FPGA	Field-Programmable Gate Array
GEM	Gaseous Electron Multiplier
IC	Integrated Circuit
MPGD	Micropattern Gas Detector
PCB	Printed Circuit Board
PSD	Position Sensitive Detector
SPICE	Simulation Program with Integrated Circuit Emphasis
TDC	Time-to-Digital Converter
THGEM	Thick Gaseous Electron Multiplier

Contents

List of Figures

List of Tables

Chapter 1

Introduction

1.1 History and Motivation

Position sensitive detectors (PSDs) are a class of particle detectors widely used in high-energy physics, astrophysics, biophysics and medicine for imaging the spatial distribution of various radioactive sources. Applications requiring PSDs are often interested in event counting with excellent spatial, temporal and energy resolution. The earliest particle tracking/imaging detector is the so-called multiwire proportional counter (MWPC) and was developed by Charpak *et al.* (1968). The revolutionary MWPC allowed imaging of thousands of particles per second with millimeter scale spatial resolution. Over the years, the spatial resolution of MWPCs has improved down to a few hundred microns. However, difficulties associated with wire assembly, and rate induced space charge effects, promoted research into other technologies. The 1980s saw a revolution in semiconductor detectors with the development of the silicon strip detector by Belau *et al.* (1983). Capable of spatial resolutions of a few tens of microns and energy resolution less than 1%, silicon strip detectors were considered the *de facto* standard in imaging and particle tracking applications for many years. Like most semiconductor detectors, silicon detectors must be cryogenically cooled and are costly to manufacture in large sizes; thus, the search for alternative technologies

continued.

The same technology which made manufacturing of silicon strip detectors possible also revolutionised the field of gas based detectors. By the mid 1990s, a new class of gas detectors, so-called micropattern gas detectors (MPGDs), had emerged. Constructed using modern photolitography techniques, current MPGDs are capable of spatial resolutions below 50 μm (Bressan *et al.*, 1999; Bellazzini *et al.*, 2007) and timing resolutions of few nanoseconds (Breskin *et al.*, 2002). The most popular MPGD to date is the Gaseous Electron Multiplier (GEM) invented by Sauli (1997). Constructed from copper-clad polyimide foils, GEMs are chemically etched to produce a large number of small holes ($<$70 μm diameter). When a potential difference is applied across the copper conductors, a strong electric field is established inside the holes and drifting electrons are amplified in an avalanche process. A remarkable property of GEMs is the ability to separate the amplification region from the readout structure. This feature allows optimization of the readout structure according to the requirements of the imaging application. More recently, a larger version of the GEM, known as the Thick Gaseous Electron Multiplier (THGEM), has been introduced. The construction method and properties of THGEMs will be discussed in detail throughout this thesis.

Position sensitive MPGDs can be constructed using one of two basic readout techniques. The most common method, known as the direct charge readout, requires that each pixel of the two-dimensional array have its own pulse processing chain. An impressive example of an MPGD using this technique has been presented by Bellazzini *et al.* (2007). A decade's worth of research has produced a triple-GEM detector which

uses an application specific integrated chip (ASIC) to readout more than 100,000 individual pixels with a spatial resolution nearing 50 μm. However, since this method often results in a large number of readout channels, it has associated with it a relatively high cost and is limited to small imaging areas. Additionally, there exists applications which would be willing to sacrifice spatial and temporal resolution in favour of reduced system complexity and cost. Such systems would benefit from the so-called interpolating readout technique. Interpolating readouts reduce the number of output channels by measuring a position dependent readout parameter, such as time or signal amplitude. In the past, systems employing interpolating readout techniques displayed poor rate capabilities due to the long dead time associated with the analog-to-digital conversion process (Sobottka and Williams, 1988). Whereas direct readout methods can resolve multiple independent events in the same time window, the maximum rate of the interpolating technique is limited by the length of the acquisition window. One of the most popular interpolating readout techniques is the delay line method and its properties will be discussed.

Modern time measure electronics, such as time-to-digital converters (TDC), are capable of timing resolutions down to a few picoseconds. Such timing capabilities permit building faster delay lines which in turn shorten the necessary acquisition window. When combined with high speed field programmable gate arrays (FPGAs), it is possible to design delay line based readouts which can process up to a few million events per second. In current literature there exists a few examples of delay line based GEM detectors (Bachmann *et al.*, 2002; Guedes *et al.*, 2003; Marinho *et al.*, 2005; Zhou *et al.*, 2009) and only one using THGEMs (Cortesi *et al.*, 2007). The aforementioned GEM and THGEM imaging detectors have demonstrated spatial resolutions

nearing 100 μm and 300 μm, respectively. Considering the relative simplicity of the delay line readout, such results are certainly inspiring.

The mechanical robustness of THGEMs, combined with their low cost per unit area, have motivated research into the development of our own large area imaging detector. To accomplish this, four main objectives have been set. First, THGEMs should be used to amplifying primary ionization electrons. Second, the interaction position should be inferred using a two-dimensional delay line readout. Next, image reconstruction hardware and software should be developed. Lastly, detector operation should be demonstrated using X-rays and alpha particles. This thesis attempts to accomplish the aforementioned objectives by describing the development of a prototype detector with an imaging area of 40 x 40 mm^2 and which can be operated under various gas mixtures and pressures. While not particularly optimized for a specific imaging application, this prototype serves as a framework for the development of future THGEM based imaging detectors.

1.2 Incident radiation interaction

To evaluate the performance of the prototype imaging detector, two radiation sources were used. The first was a ^{244}Cm source which decays to ^{240}Pu by emission of alpha particle. As shown by the decay scheme in Figure 1.1, the alpha particles can be emitted with two energies: 5.763 MeV and 5.806 MeV. The ^{244}Cm source had an activity of 3.7 kBq and was mounted directly above the THGEMs in a collimated assembly.

The second radiation source was an X-ray tube for which the accelerating potential could be varied between 20 to 160 kVp. For imaging, the accelerating potential was kept at or below 40 kVp. In this energy range, the incident X-rays interact primarily

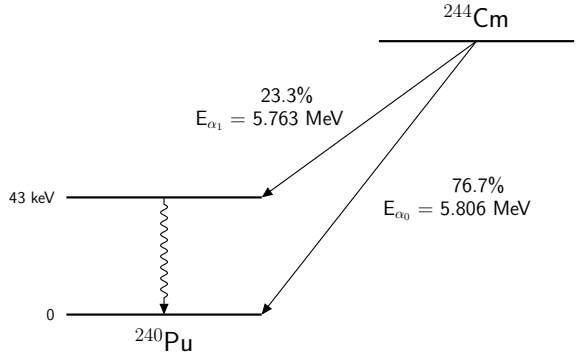

Figure 1.1: Decay scheme of ^{244}Cm.

through the photoelectic effect which describes the absorption of a low energy photon (X-ray or gamma-ray) by an atom. During this process, a portion of the photon energy is preferentially transferred to a bound K-shell electron which is subsequently ejected from the atom. This electron, labelled the *photoelectron*, is released with an energy E_{pe} equal to the incoming photon energy E_{γ} minus the binding energy E_{be} of the electron – see Equation 1.1.

$$E_{pe} = E_{\gamma} - E_{be} \tag{1.1}$$

Following the emission of a photoelectron, the atom rearranges its electronic structure to fill the inner shell vacancy. This de-excitation mechanism can occur via the emission of characteristic X-rays or Auger electrons. The photoelectron, as well as the Auger electron, go on to produce electron-ion pairs along their trajectory. The signal induced by these primary electron-ion pairs is used to determine the interaction position of the X-rays. The range and angular distribution of the photoelectrons are of particular interest for imaging applications since they fundamentally limit the spatial resolution of the detector.

The angular distribution of emitted photoelectrons is governed by the conservation of energy and momentum. The differential cross-section for the emissions of a K-shell photoelectron, following the absorption of an X-ray photon with energy $\mathtt{E}_\gamma$, is given in Equation 1.2 (Heitler, 1954).

$$\frac{\mathtt{d}\sigma}{\mathtt{d}\Omega} = \mathtt{r}_0^2 \frac{\mathtt{Z}^5}{137^4} \left(\frac{\mathtt{m_e c}^2}{\mathtt{E}_\gamma} \right)^{\frac{7}{2}} \frac{4\sqrt{2}\mathtt{sin}^2(\theta)\mathtt{cos}^2(\varphi)}{(1-\beta\mathtt{cos}(\theta))^4} \tag{1.2}$$

In the above equation, $\mathtt{r}_0$ is the classical electron radius, $\mathtt{Z}$ is the charge of the nucleus, $\mathtt{m_e}$ is the electron rest mass, θ is the azimuthal angle of the electron momentum, φ is the polar angle of the electron momentum and β is the ratio between the velocity of the photoelectron and the speed of light. For low energies, the photoelectron is emitted in a plane perpendicular to the incident photon direction and its angular distribution is governed by the $\mathtt{sin}^2(\theta)$ term. Due to the strong Z dependence of the interaction cross-section, heavy gas mixtures are desired for the detection of low energy X-rays.

Following its emission, the photoelectron ionizes gas molecules along its trajectory until it becomes thermalized. The radial distance from the point of interaction to the final stopping position is known as the photoelectron range. To improve the spatial resolution it is imperative that the photoelectron range be as short as possible. The actual path of the photoelectron is quite random and can be up to three times longer than its range. The range of electrons, in a few common detection gases, have been calculated using the collision stopping power of electrons (NIST ESTAR) and the continuous slowing down approximation (CSDA). The results are presented in Figure 1.2.

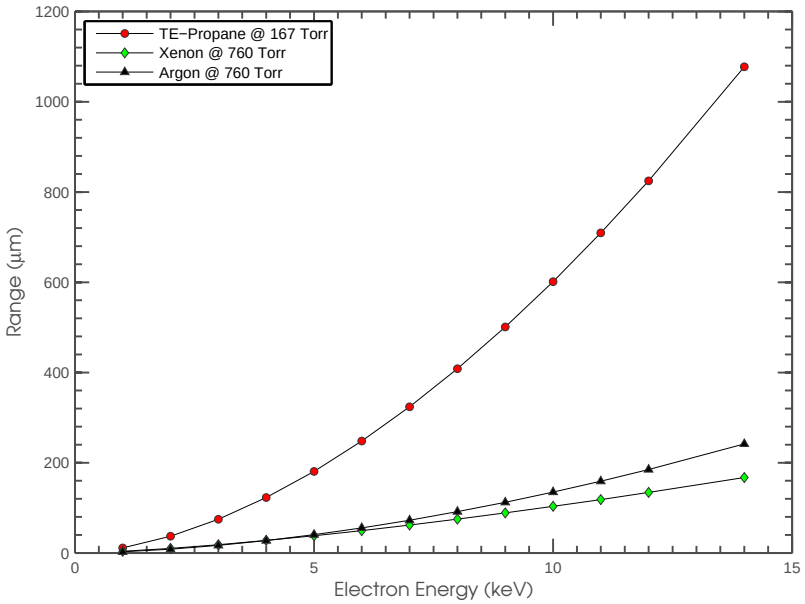

Figure 1.2: A plot of range versus electron energy for common detection gases.

1.3 General properties of MPGDs

1.3.1 Mean number of primary electron-ion pairs

As the primary charged particles move along their trajectory, they experience a series of collisions with the gas molecules inside the detector. In the case of heavy charged particles, such as alphas, energy loss is primarily dominated by inelastic collisions with the atomic electrons and result in a large number of electron-ion pairs. The maximum kinetic energy (T_{max}) transferred, in a single collision, from a particle of mass m_0 to an atomic electron of mass m_e is given by Equation 1.3. In this equation, c is the speed of light, $\beta = \frac{v}{c}$ is the relative velocity of the particle and $\gamma = \frac{1}{\sqrt{1-\beta^2}}$ is the relativistic factor.

$$T_{max} = \frac{2m_e c^2 \beta^2 \gamma^2}{1 + 2\gamma\frac{m_e}{m_0} + \left(\frac{m_e}{m_0}\right)^2} \tag{1.3}$$

For non-relativistic heavy charged particle, such as the alpha particles used to

characterize the THGEM imaging detector, the mean energy lost per unit path length ($\frac{dE}{dx}$) is given by the classic Bethe-Bloch equation – see Equation 1.4.

$$-\frac{dE}{dx} = \frac{4\pi N z^2 e^4}{m_e v^2 Z} \ln\left(\frac{2 m_e v^2}{I}\right) \tag{1.4}$$

In the above equation, z is the particle charge, v is the particle velocity, N is the electron density of the material and I is the mean excitation energy of the medium. In low density mediums, such as the one used in the THGEM imaging detector, only a small fraction of the incident alpha energy is deposited and energy loss can be approximated as constant over the trajectory of the particle.

The interactions of electrons differs significantly from that of heavy charged particles. This is primarily because electrons have small mass and only small amount of energy is necessary to accelerate them to relativistic velocities. Whereas heavy charged particles traverse a medium in a primarily linear fashion, the trajectory of electrons is often dominated by large angle changes. Energy loss by electrons can be classified as either collisional or radiative – see Equation 1.5. Collision interactions, such as Coulomb scattering and Möller scattering, are dominant at lower electron energies while radiative interactions, such as bremsstrahlung or Cherenkov, dominate the higher energies.

$$\left(\frac{dE}{dx}\right)_{tot} = \left(\frac{dE}{dx}\right)_{col} + \left(\frac{dE}{dx}\right)_{rad} \tag{1.5}$$

In a single collision, the maximum energy transfer (E_{max}) between an incident electron, with kinetic energy E, and an atomic electron is given by Equation 1.6.

$$E_{max} = E - m_e c^2 \tag{1.6}$$

If the kinetic energy of the incident electrons is greater than the electron binding energy of the gas molecules, energy loss is primarily characterized by the ionization and excitation of the gas molecules. In this situation, the energy lost per unit path length, due to collision interactions, is given by the Bethe-Bloch equation for electrons – see Equation 1.7.

$$-\left(\frac{dE}{dx}\right)_{col} = \frac{2\pi NZe^4}{\beta^2 m_e c^2}\left\{\ln\left[\frac{(\gamma-1)\beta^2 E^2}{2I^2}\right] + \frac{1}{\gamma^2}\left[\frac{\gamma^2-2\gamma+9}{8} - (2\gamma-1)\ln 2\right]\right\} \quad (1.7)$$

For the energies discussed in this thesis, the fraction of energy lost due to radiative processes is negligible. It is therefore expected that the photoelectrons undergo primarily collision interactions, which result in the production of electron-ion pairs. The number of electron-ion pairs produced depends on the trajectory of the primary ionizing particle, its energy and the gas medium. It is generally difficult to calculate the distribution of primary electron-ion pairs without the use of numerical methods. However, some generalizations can be made using the deposited energy (ΔE) and the W-value of the gas. The W-value is defined as the mean energy required for generating an electron-ion pair and is best determined experimentally. If the W-value for a specific radiation and gas type is known, the average number of electron-ion pairs ($\bar{N}$) can be calculated using Equation 1.8.

$$\bar{N} = \frac{\Delta E}{W} \quad (1.8)$$

1.3.2 Diffusion effects

In a gaseous environment, and the absence of an external electric field, the primary ionization electrons diffuse uniformly from their origin. The diffusion process can be

described by a time dependent Gaussian distribution with a spread σ_x along a given axis $\vec{x}$. As shown in Equation 1.9, the spread is given by the square root of the diffusion coefficient (D_x) and time (t).

$$\sigma_x = \sqrt{2D_x t} \tag{1.9}$$

The diffusion coefficient can be calculated given the diffusion velocity (u) and the mean free path (ξ) of the electrons in the gas – see Equation 1.10.

$$D_x = \frac{u\xi}{3} \tag{1.10}$$

To make any meaningful measurements regarding the radiation interaction, the primary electrons must be collected using an external electric field. An external electric field influences the motion of primary electrons by modifying the diffusion coefficient and diffusion velocity inside the gas. Under an electric field, the velocity of charges is known as the drift velocity (v) and the spread along a given axis is a function of distance travelled (l) and drift velocity – see Equation 1.11.

$$\sigma_x = \sqrt{\frac{2D_x l}{v}} \tag{1.11}$$

The drift coefficient, and drift velocity, can be used to describe the movement of charges in the absence of an external electric field . In an external electric field, it is convenient to define the transverse and longitudinal drift coefficients, D_T and D_L,

which are dependent on the electric field strength.

$$D_T = D_L = \sqrt{\frac{2D_x}{v}} \tag{1.12}$$

The resulting expressions for transverse and longitudinal spread are given in Equation 1.13 and Equation 1.14, respectively.

$$\sigma_T = D_T\sqrt{l} \tag{1.13}$$

$$\sigma_L = D_L\sqrt{l} \tag{1.14}$$

It is generally understood that as the electric field strength increases, the drift velocity also increases which subsequently reduces the observed drift coefficients. Additionally, drift has a square root dependence on the distance travelled. Therefore, to reduce drift effects one must increase the electric field in the drift region and decrease the drift gap.

1.3.3 Electron multiplication

In many cases, there are too few primary electrons to be directly measured in pulse mode operation. For example, if a 30 keV X-ray entirely deposits its energy within the sensitive region of the detector, it would produce 1.19×10^3 electron-ion pairs for a W-value of 25.2 eV/ion pair (Krajcar-Bronić and Srdoč, 1994). The sensitive region of the THGEM detector has a calculated capacitance of approximately 9 pF, resulting in a theoretical pulse amplitude of 21 μV. Such low signal amplitudes are extremely difficult to measure even with low noise pulse processing electronics.

All MPGDs, and conventional wire based proportional counters, take advantage

of internal charge multiplication to produce large signal amplitudes. In weak electric fields, the electrons and positive ions experience a series of weak collisions with neutral gas molecules. The kinetic energy exchanged in these collisions is small and the charges simply drift to their respective electrodes in a random fashion. However, in strong electric fields, electrons can attain high kinetic energies resulting in collisions which ionize the gas molecules. The secondary electrons will also experience the strong electric field and in turn create other ion pairs. This multiplication process is called a Townsend avalanche.

The Townsend equation, shown in Equation 1.15, describes the fractional increase in the number of electrons in terms of the first Townsend coefficient (α) for the gas, the number of electrons ($\mathtt{N_x}$) at a given position and the path length ($\mathtt{dx}$).

$$\mathtt{dN_x} = \alpha \mathtt{N_x dx} \tag{1.15}$$

For a constant electric field, such as in a parallel plate geometry, the number of electrons grows exponentially with distance – see Equation 1.16.

$$\mathtt{N_x} = \mathtt{N_0 exp}(\alpha \mathtt{x}) \tag{1.16}$$

It follows that the gas gain ($\mathtt{G}$) is given by the ratio of the number of electrons at a distance x to the number of primary electrons ($\mathtt{N_0}$) – see Equation 1.17.

$$\mathtt{G} = \frac{\mathtt{N_x}}{\mathtt{N_0}} \tag{1.17}$$

Therefore, the total electron charge ($\mathtt{Q}$) collected at the anode can be represented in

terms of the number of primary electrons (N_0) and the average gas gain ($\bar{G}$) – see Equation 1.18.

$$Q = N_0 e \bar{G} \tag{1.18}$$

In the case of MPGDs, the electric fields cannot be approximated as constant. For example, the electric field inside the GEM or THGEM holes is almost constant, while it diverges quite rapidly near the openings. Additionally, as the avalanche develops, the ions significantly distort the static electric field condition due to the so-called *space charge effect*. In this condition, the Townsend coefficient (α) varies during each step of the avalanche formation. Therefore, the avalanche growth of MPGDs is slightly different than the simple approximation in Equation 1.16. The true solution requires complicated path integrals which are frequently solved using numerical Monte Carlo techniques.

Nevertheless, under the right conditions, large electron clouds ($>10^6$) can be produced over only a few hundred microns of drift. The signals induced by these large avalanches are on the order of a few tens of millivolts; thus, reducing the demand for expensive preamplifiers and improving the signal-to-noise ratio.

1.3.4 Raether limit

In parallel plate detectors, it has been experimentally demonstrated that the avalanche growth stops after reaching approximately 10^8 electrons (Raether, 1964). As the avalanche size approaches the so-called *Raether limit*, the electric field at the head and tail of the avalanche induces the formation of secondary avalanches. These secondary avalanches, known as *streamers*, form long densely ionized channels between the anode and cathode of the detector. If the streamers are not quenched, the avalanche transitions to a spark. These types of discharges are harmful to charge

sensitive electronics, such as preamplifiers, since all of the electric energy stored in the detector capacitance is released in the spark.

Ivaniouchenkov *et al.* (1999) established that a similar limit exists for MPGDs. If the total avalanche size exceeds $10^6 - 10^7$ electrons, a spark discharge occurs within the small amplification structures of MPGDs. The onset of discharges limits the maximum achievable gain of MPGDs to approximately 10^4 for X-rays and 10^3 for alpha particles. If the discharges are quenched, by lowering the high voltage, the detector operation can return to normal. Continuous operation of MPGDs in the spark region accelerates the detector ageing process and very often results in irreversible damage to the detector.

1.3.5 Spatial resolution

The spatial resolution refers to the smallest distance between two high contrast objects which can be resolved by the imaging system. As shown in Figure 1.3, the spatial resolution of the THGEM imaging detector is governed by the photoelectron range ($\sigma_{\mathtt{pe}}$), the drift of primary electrons into the hole structure ($\sigma_{\mathtt{drift}}$), the size of the avalanche ($\sigma_{\mathtt{avalanche}}$) and the resolution of the readout structure ($\sigma_{\mathtt{readout}}$). Equation 1.19 presents the detector spatial resolution ($\sigma_{\mathtt{det}}$) as the sum of the square of the aforementioned terms. To best optimize the detector for a particular imaging application, it is important to understand how each parameter influences the spatial resolution.

$$\sigma_{\mathtt{det}} = \sqrt{\sigma_{\mathtt{pe}}^2 + \sigma_{\mathtt{drift}}^2 + \sigma_{\mathtt{avalanche}}^2 + \sigma_{\mathtt{readout}}^2} \tag{1.19}$$

Monte Carlo simulations of MSGCs, performed by Schmitz (1992), suggests there are two cases for determining the spatial resolution of MPGDs. The first scenario is where the electron cloud is undersampled by the readout structure. This occurs when

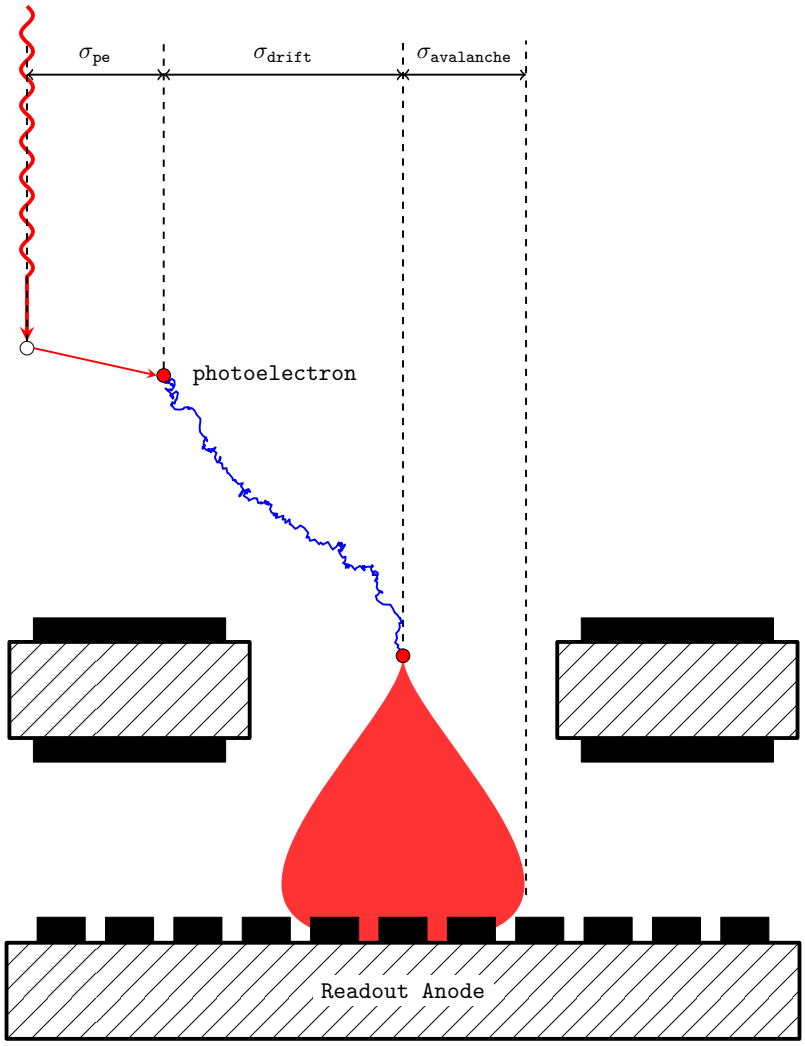

Figure 1.3: An illustration showing the contribution of the photoelectron range ($\sigma_{\mathtt{pe}}$), drift induced diffusion ($\sigma_{\mathtt{drift}}$) and avalanche cloud size ($\sigma_{\mathtt{avalanche}}$) to the spatial resolution of the imaging detector. Dimensions are exaggerated to allow visualization of all components.

the pitch ($\mathtt{p}$) of the readout is larger than the size of the electron cloud ($\sigma_{\mathtt{avalanche}}$) and only one readout strip, per axis, responds to an event. In this case, the spatial resolution of the detector can be approximated by the classical expression for a periodic structure with a pitch $\mathtt{p}$ (Bock and Vasilescu, 1998) – see Equation 1.20.

$$\sigma_{\mathtt{det}} \approx \sigma_{\mathtt{readout}} = \frac{\mathtt{p}}{\sqrt{12}} \tag{1.20}$$

The second scenario refers to a dense readout structure, where $\mathtt{p} \ll \sigma_{\mathtt{avalanche}}$. In this case the electron cloud can be effectively sampled and the avalanche starting point can be reconstructed using the center-of-charge method. The spatial resolution of such a detector is primarily limited by the range of the photoelectron ($\sigma_{\mathtt{pe}}$) and the drift of primary electrons into the hole structure ($\sigma_{\mathtt{drift}}$) – see Equation 1.21.

$$\sigma_{\mathtt{det}} \approx \sqrt{\sigma_{\mathtt{pe}}^2 + \sigma_{\mathtt{drift}}^2} \tag{1.21}$$

As previously discussed, both the photoelectron range and the diffusion constants are highly dependent on the gas mixture. To simultaneously increase the detection efficiency, reduce the photoelectron range and limit the diffusion of primary electrons, it is desirable to use heavy gas mixtures at high operating pressures.

1.4 Thesis Preface

In this thesis, the development of the two-dimensional delay line based THGEM imaging detector is presented. Chapter 2 gives a brief history of THGEM detectors and describes the operating principle of the imaging detector. The gas containment chamber, the manufacturing of THGEMs, the detector assembly and calibration of

the pulse processing chain are also described in this chapter. Finally, the effective gain and stability of various THGEM configurations are discussed. In Chapter 3, the two-dimensional delay line readout is presented. This chapter introduces properties of lumped parameter delay lines, construction methods for one- and two-dimensional readout anodes, the analog signal processing chain and calibration of the delay lines. Chapter 4 focuses on the development of the data acquisition (DAQ) system, which uses a TDC and an FPGA to acquire the digital radiographs. The hardware, firmware, software and performance of the TDC DAQ event reconstruction system will be presented. Lastly, Chapter 5 introduces the experimental methods used to measure the performance of the prototype imaging detector. Conclusions, a brief discussion and suggestions for future work are presented in Chapter 6.

Chapter 2

Design and characterization of the Thick Gaseous Electron Multipliers

Since the 1980s, with the development of the first microprocessors, the microelectronics industry has been pushing the limits of resolution. Fabrication processes, such as photolithography, could be applied to the construction of structures with sub-μm precision and capable of sustaining high electric fields. By the mid 1990s, the continuous advancement of photolithography, and other printed circuit board (PCB) technologies, had ignited a "*Renaissance*" in the field of gas based detectors. A new class of gas detectors, so-called micropattern gas detectors (MPGDs), had emerged. One of the first MPGDs developed was the microstrip gas chamber (MSGC) and its operation resembles that of a conventional wire chamber (Oed, 1988). The MSGC had many attractive features such as high rate capabilities, high gain, and excellent position resolution, which were beneficial for many applications. However, the issue with fatal discharges, induced by heavily ionizing particles or high rates, resulted in the eventual abandonment of the technology. In 1997, the gaseous electron multiplier (GEM) was introduced by Sauli as a pre-amplification stage to the MSGC. The GEM allowed the MSGC to work at a lower bias voltage, where the probability and energy released in discharges was lower. However, the scientific community soon realized the

GEM was a capable detector in its own right and the technology used in its fabrication was applied to the development of a wide range of electron multiplying structures. Such devices have been the subject of numerous studies with applications in particle tracking, calorimetry, photon detection and imaging.

In recent years, the so-called Thick Gaseous Electron Multiplier (THGEM) has emerged as an alternative to GEMs. Initially introduced by Periale *et al.* (2002) and extensively studied by Chechik *et al.* (2004); Shalem *et al.* (2006); Cortesi *et al.* (2007), the THGEM features a hole structure which is 5-10 times larger than a GEM and is manufactured by mechanically drilling a rigid substrate. The substrate used is the same copper clad FR4 glass-reinforced epoxy laminate sheets found in standard PCBs. Using standard PCB manufacturing techniques, along with economies of scale, results in structures which are mechanically rigid and cheap to produce. As a result, THGEMs are frequently found in applications requiring large detection areas with moderate timing and localization resolution.

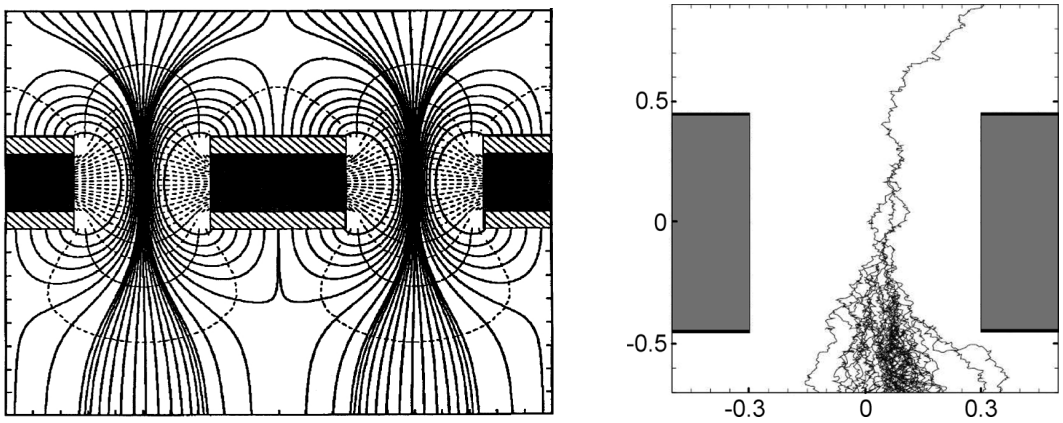

Figure 2.1: Electric field lines of a biased GEM detector (a), from Sauli (1998), and the formation of a Townsend avalanche inside a THGEM hole (b), from Byun *et al.* (2009).

Fundamentally, there exists very few operational differences between the THGEM and GEM structures. Biasing a THGEM, by applying a high potential difference between the copper electrodes, establishes a strong electric field within the holes which partially protrudes into adjacent volumes. The particular shape of the field, is similar to the GEM illustrated in Figure 2.1 (a) and is responsible for efficient focusing of primary ionization electrons into the hole structure. As a result of the strong electric field, electrons entering the THGEM holes undergo multiplication via a Townsend avalanche – see Figure 2.1 (b). The resulting charge cloud can then be collected by a wide array of anodes which are connected to an electronic pulse processing chain. Due to the larger dimensions, THGEMs can achieve higher gains and efficiencies than standard GEMs (Breskin *et al.*, 2009). However, their application is often limited to studies which favour high gain and mechanical ruggedness over position and time resolution.

Within the McMaster Nuclear Instrumentation and Microdosimetry group, THGEMs have been used primarily for the development of novel microdosimetry detectors. The first study, by Byun *et al.* (2009), describes the simulation and testing of a THGEM based microdosimetric detector. Orchard (2010) showed the performance of the detector matches that of traditional tissue-equivalent proportional counters (TEPCs). Using Geant4, I demonstrated that the simulated energy deposition pattern within the THGEM detector, for various neutron energies, shows reasonable agreement with experimental data and matches that of the ideal microdosimetric detector (Hanu *et al.*, 2010). Anjomani *et al.* (2013) used the same Geant4 code to study design parameters for a new multi-element THGEM based microdosimetric detector. The results from both simulations were used to construct an optimized multi-element detector which

is currently under development.

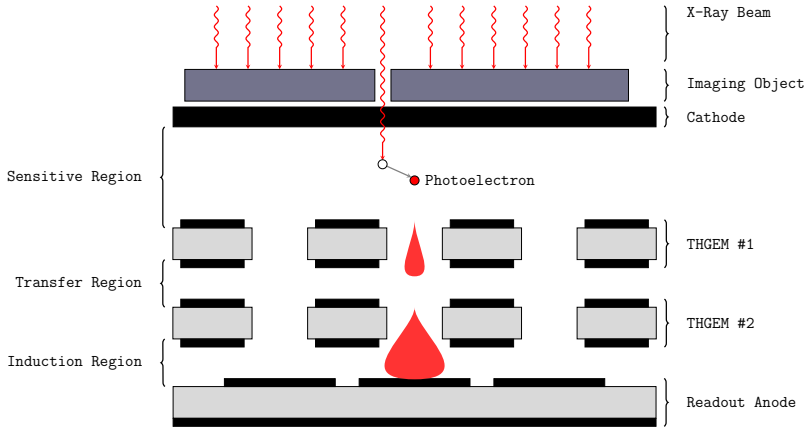

Figure 2.2: Illustration showing the operational principle behind the prototype THGEM imaging detector. Figure not to scale.

Although the current application of THGEMs is different from past projects, the fundamental parameters governing their operation and performance remains unchanged. In the prototype imaging detector, described henceforth, two THGEMs are cascaded to achieve higher gains and increased operation stability. The principle of operation behind the imaging detector is illustrated in Figure 2.2. Typically, an object of interest is placed upon the detector entrance window and exposed to a wide X-ray beam. Transmitted X-rays will pass into the sensitive region of the detector and interact via the photoelectric effect with the detection gas. The primary electrons (photoelectrons) are focused towards the strong dipole field of the THGEM holes where they experience a Townsend avalanche with high proportional gains. Upon leaving the last THGEM device, the electron charge cloud is collected by the sampling electrodes on a two-dimensional readout anode. Using fast electronics and a timing based interpolation technique, described in Chapter 3 and Chapter 4, a transmission radiograph of the object is constructed in real-time.

In this chapter, I will describe the use of THGEMs to amplify the primary electrons created in the interaction of X-rays, or alpha particles, with the sensitive region of the imaging detector. The first few sections will discuss the gas containment chamber, the fabrication of the THGEMs, the detector assembly and high voltage distribution. Next, the effective gain of the single and double THGEM configuration will be compared. Finally, the gain stability of the double THGEM configuration will be reported.

2.1 Gas Containment Chamber

To experiment with MPGDs, one must first construct the gas containment chamber which houses the detector assembly and all of the necessary connectors required for its operation. Since the design of positive pressure chambers is different than vacuum chambers, a range of operating pressures must be established prior to the construction of the chamber. For the THGEM studies, it was determined the intended operating pressure should vary from 60 Torr to 760 Torr. This allows the same chamber to be used in microdosimetry studies, which require low pressures, as well as the detection of X-rays, which generally require higher pressures.

The gas containment chamber, used by the THGEM imaging detector, has been constructed from 6061 aluminium alloy with an outer diameter of 10 inches and a height of approximately 6 inches. As illustrated in Figure 2.3, the sealed chamber consists of a main body, a covering lid with interchangeable entrance windows and a flange to seal the window. Technical drawings of the chamber parts are included in Appendix A.1. On the underside of the chamber body, there exists two SHV5 high voltage connectors, five BNC signal connectors, and a gas filling port. To allow for long operating times at low pressure, special high vacuum connectors were selected.

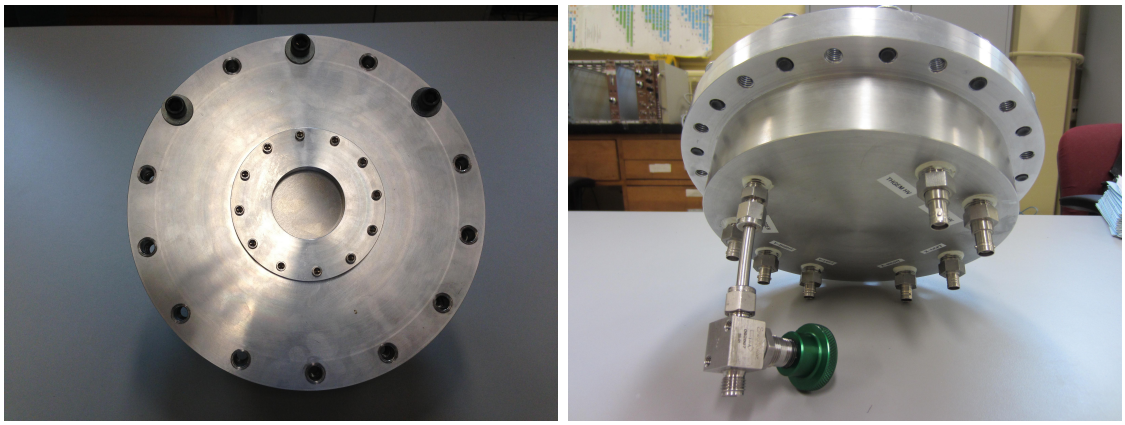

(a) **(b)**

Figure 2.3: Pictures of the covering lid (a) and the underside (b) of the gas containment chamber used in the THGEM imaging studies.

Additionally, a low outgassing epoxy (Loctite 1C Hysol) was used to hermetically seal the connector to the chamber body.

Prior to filling the detector with the operating gas, the chamber was connected to a vacuum pump to remove the air trapped inside. Using an oil diffusion pump, the chamber could be evacuated to a pressure below $1x10^{-4}$ Torr within 3 hours. Once a sufficient vacuum level was reached, the detection gas was pumped to the desired pressure and the chamber was sealed.

2.2 THGEMs

The first THGEMs, used by Orchard (2010), had a small number of holes and were manually fabricated with a homemade drilling machine in our lab. Although successful, it is impractical to apply such techniques for drilling a large number of holes (greater than 1,000). As such, it was decided to turn to the electronics industry for help. Using standard PCB manufacturing techniques, THGEMs such as the one illustrated in Figure 2.4 (a) were constructed. Fabricated from FR4 glass-reinforced

epoxy laminate sheets, the THGEMs have 0.03 mm copper clad on both sides and outer dimensions of 55 x 55 mm^2. To bias the THGEMs, small pads were included which allow soldering of high voltage wires to both sides. While the hole dimensions of the three THGEMs are different, they all share similar features regarding the hole structure. As illustrated by the scanning electron microscope (SEM) image in Figure 2.4 (b), all of the holes have the copper etched away from the edge exposing the bare dielectric.

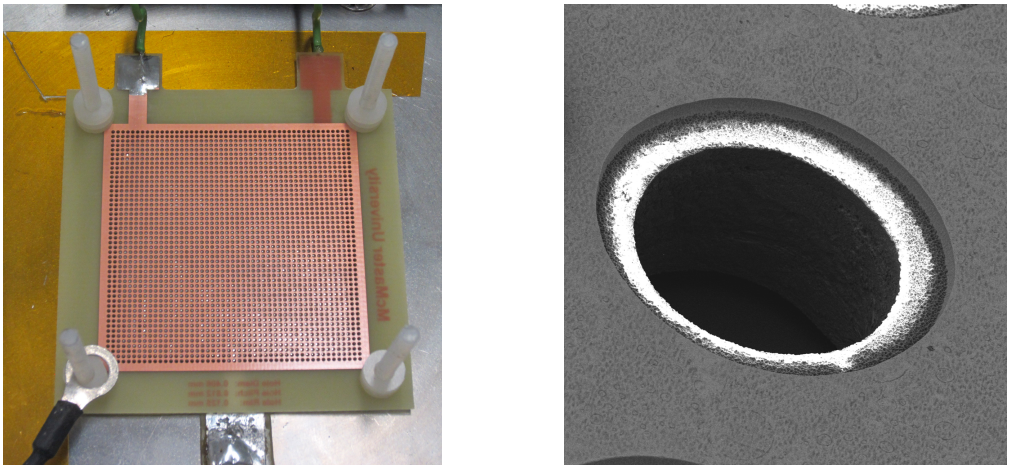

(a) **(b)**

Figure 2.4: Picture of a 0.5 mm THGEM (a) and a scanning electron microscope image (b) of the hole structure.

Fabrication of the many holes is accomplished via computer numerical controlled (CNC) drilling machines. Since CNC drilling is a standard process in any PCB manufacturing facility, THGEMs can be made in relatively large sizes and low unit costs. To guarantee quality over a large number of holes, frequent tooling changes are necessary. Small imperfections in the copper surrounding the holes can result in extremely high electric field gradients which can destroy the THGEM during a highly ionizing event. Issues with hole quality can be partially circumvented by etching a

small rim in the copper surrounding a hole. As noted by Orchard (2010), adding a small rim around the holes significantly improved the reliability of the detector. Similarly, Breskin *et al.* (2009) reported that THGEMs with etched rims can achieve 10-fold higher gains than without a rim and maximal gain is achieved from a 0.1 mm rim. Therefore, all of the THGEMs used in these experiments included a 0.1 mm etched rim around each hole.

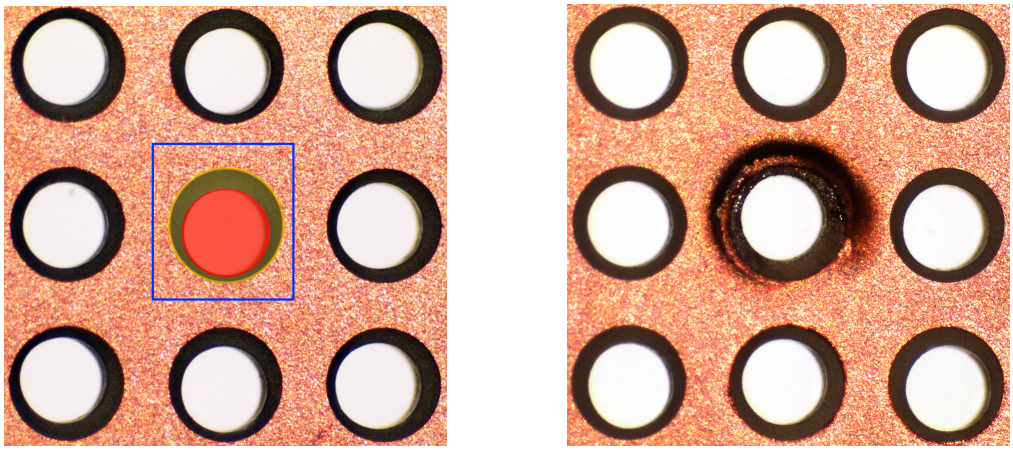

(a) **(b)**

Figure 2.5: Optical microscope images of the fabricated THGEMs (0.5 mm), showing the hole-rim eccentricity (a) and the resulting spark induced damage (b).

While THGEMs with etched rims can be operated at higher voltages and therefore higher gains, they are not without peculiarities. As shown in Figure 2.5 (a), it is rather difficult to achieve uniformly concentric rims and holes over the entire active area. This issue, referred to as hole-rim eccentricity, is a consequence of the fabrication method employed by the manufacturing company and is frequently the cause of spark induced damage – see Figure 2.5 (b). Additionally, the etched rim results in charging up and polarization of the exposed dielectric. For this reason, THGEMs with etched rims exhibit large gain variations, long stabilization times, and worse energy resolution

than THGEMs without a rim (Breskin *et al.*, 2010; Alexeev *et al.*, 2010). However, for the imaging application described in this thesis, higher gains are favourable due to the increased signal-to-noise ratio (SNR).

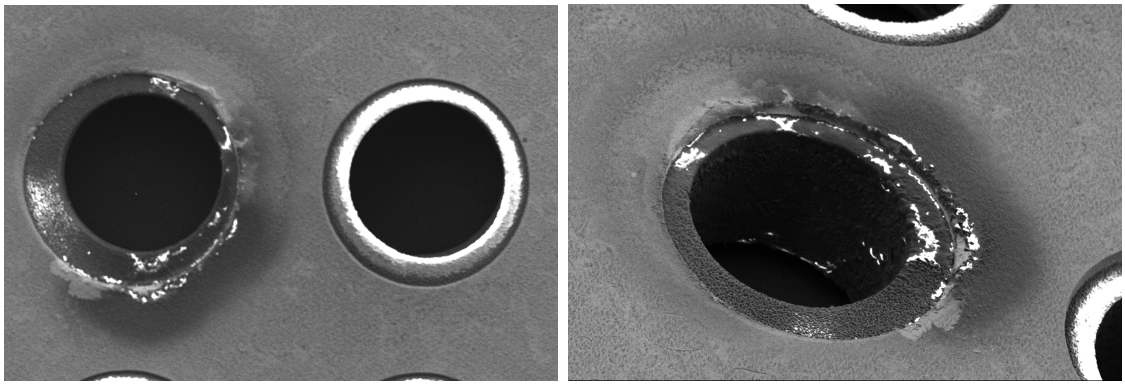

(a) **(b)**

Figure 2.6: SEM image comparing a normal and spark damaged 0.5mm hole (a). The isometric projection (b) of the spark damaged hole shows the partial melting of the FR4 insulator.

Spark induced discharges are catastrophic and render the THGEMs inoperable. As illustrated by the SEM images in Figure 2.6, following a spark, a layer of growth covers the dielectric and the copper conductor is partially eroded. Petrov *et al.* (2009) suggests that the growth layer is conductive and acts as a resistor in parallel with the capacitance of the THGEM. This hypothesis can be partially confirmed using the SEM images. In Figure 2.6 (a), the dielectric of the right most hole is primarily a white color. This indicates that the surface was charging up from the electron beam used during the SEM. The insulator of the spark damaged hole does not show the white coloration, indicating that the surface is conductive. As the conductive layer forms, the THGEM detector transitions from the glow discharge region to the arc region (Peskov and Fonte, 2009). Once the conductive growth layer forms, the bias voltage must be significantly reduced to stop the discharges. The lower operating

voltage does not produce a strong enough electric field for multiplication to occur and the device is rendered defective. Protected THGEMs, such as the Resistive Electrode Thick GEMs (RETGEMs) developed by Oliveira *et al.* (2007), prevent the transition from the glow discharge region to the arc region. For RETGEMs, the discharge is stopped by reducing the bias voltage and the devices can resume operation without any change in their characteristics. It is strongly recommended that such devices be investigated for future projects.

Table 2.1: A list of THGEM dimensions used to evaluate the electron multiplication stage of the imaging detector.

Diameter (mm)	Pitch (mm)	Etched Rim (mm)	Thickness (mm)
0.40 ± 0.03mm	0.81 ± 0.03mm	0.1mm	0.41 ± 0.01mm
0.51 ± 0.03mm	1.02 ± 0.03mm	0.1mm	0.48 ± 0.01mm
0.81 ± 0.03mm	1.63 ± 0.03mm	0.1mm	0.81 ± 0.01mm

The THGEMs used in this work were ordered via the online service offered through MyroPCB (`www.myropcb.com`) and feature an active amplification area of 42 x 42 mm^2. As listed in Table 2.1, three different THGEM configurations were studied. In each case, the insulator thickness is the same as the hole diameter while the hole pitch is exactly twice the hole diameter. Aside from evaluating each THGEM under a microscope, no special cleaning procedures were followed.

2.3 Detector Assembly

The THGEM detector assembly consists of the sensitive region, the charge amplification elements and the readout plane. The sensitive gap is the volume of gas between the cathode and the top THGEM structure in which primary ionizations are produced – see Figure 2.2. Constructed from a metallized Mylar foil, and assembled on a plastic support structure, the cathode establishes a weak electric field which

guides the primary ionizations towards the THGEM elements. The charge amplification elements consists of two THGEM structures separated by a small transfer gap. This gap should be large enough to allow for efficient movement of charges between the THGEM structures yet not so large for interactions in this region to be of concern. Lastly, the readout plane is defined by a two-dimensional readout anode and a small signal induction region. The readout anode, described in Chapter 3, collects the charge cloud and produces the four timing signals used in the position reconstruction. The induction region allows for decoupling the amplification elements from the readout anode, protecting the sensitive preamplifiers during discharges. A picture of the assembled THGEM imaging is included in Figure 2.7. The THGEM assembly is bolted inside the gas containment chamber using Teflon screws and spacers for the various gaps. A cross-sectional view of the detector assembly is shown in Figure 2.8.

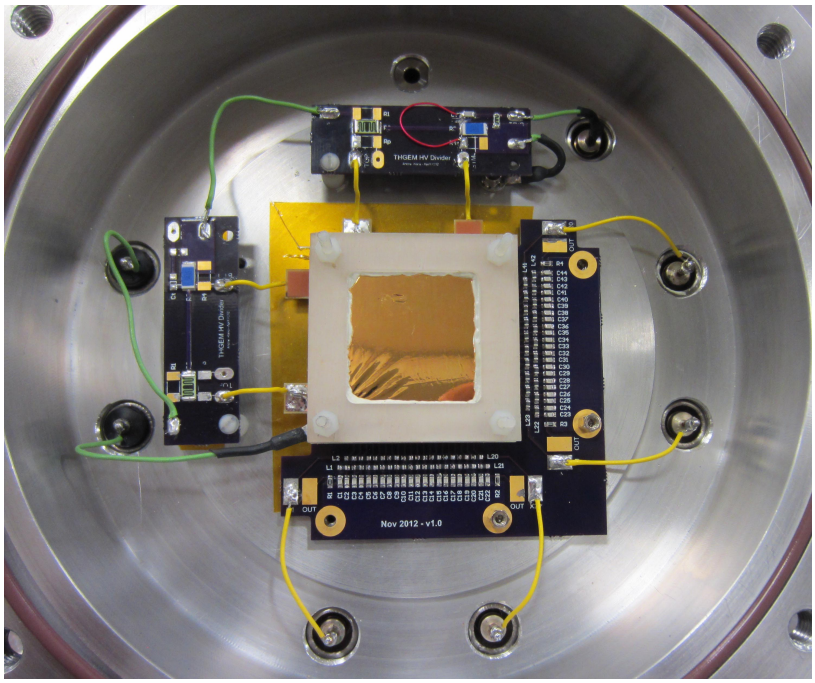

Figure 2.7: A picture of the open chamber showing the high voltage divider PCBs, the THGEM detector assembly and the two-dimensional readout board.

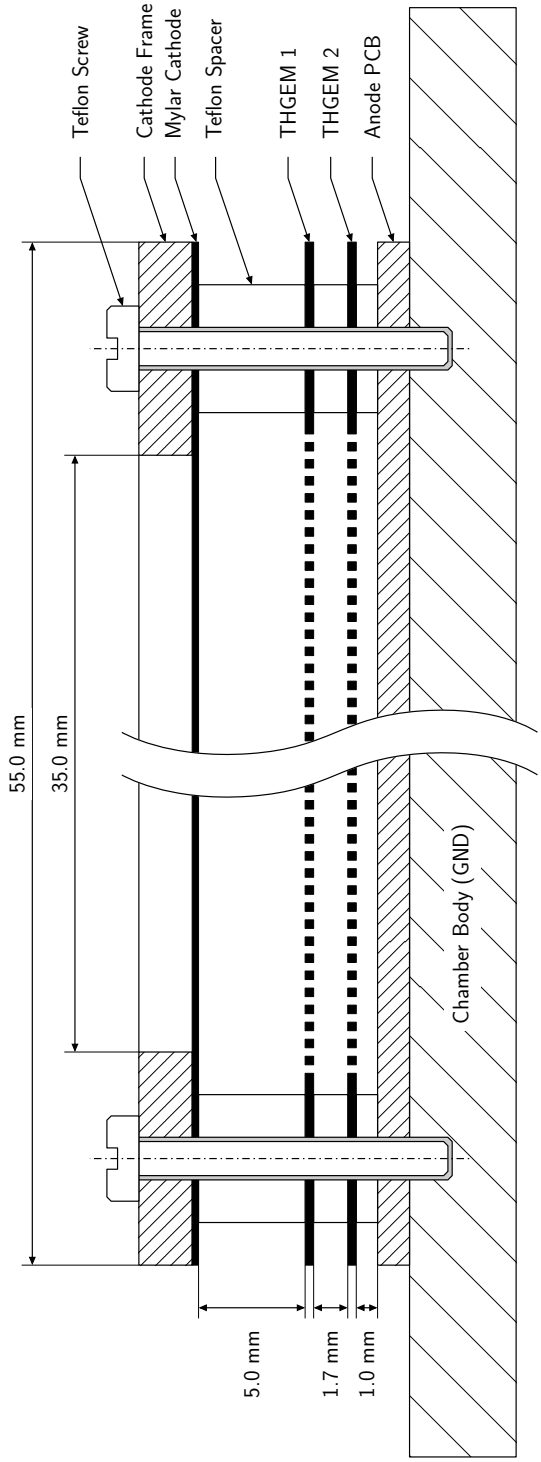

Figure 2.8: A cross-sectional view of the THGEM imaging detector. The entire assembly is bolted inside the gas containment chamber using Teflon screws and spacers for the various gaps.

Following the assembly of the THGEM detector, the chamber was pumped down to 10^{-5} Torr and filled with a propane based gas mixture to a pressure of 167 Torr. The gas mixture, known as tissue equivalent propane (TE-propane), consists of 55% C_3H_8, 39.6% CO_2 and 5.4% N_2. The choice of filling gas was primarily based on availability and previous experimentation by Orchard (2010). Although not ideal for the detection of X-rays, TE-propane is a stable gas mixture with excellent gain characteristics. After filling, the chamber was sealed by the valve on the underside of the gas containment chamber.

To generate the high electric fields necessary for multiplication, the THGEMs are biased to several hundred volts. Two negative power supplies (Bertan Associates Model 305), capable of output voltages within a range of 0 to - 5000 V, were used to bias the various regions of the THGEM imaging detector. While the cathode was independently biased, the two THGEMs were biased through a resistor ladder. Schematics for the high voltage connections are illustrated in Figure 2.9. To filter out some of the electronic noise, induced by the fast switching circuits inside the power supplies, two low pass filters were included. The filters for the cathode and THGEM bias have cutoff frequencies of 1.3 Hz and 10.6 Hz, respectively. The low pass filters significantly reduced the electronic noise in the anode signal and are also recommended for future experiments.

As illustrated in Figure 2.1, the diverging electric field lines near the openings of the THGEM holes cause a small fraction of the electrons produced in the avalanche to be lost to the bottom electrode. Normally, these loses are accounted for in the effective gain measurements and are of little concern. However, for applications such as the timing method used in this thesis, the signal induced in the bottom THGEM

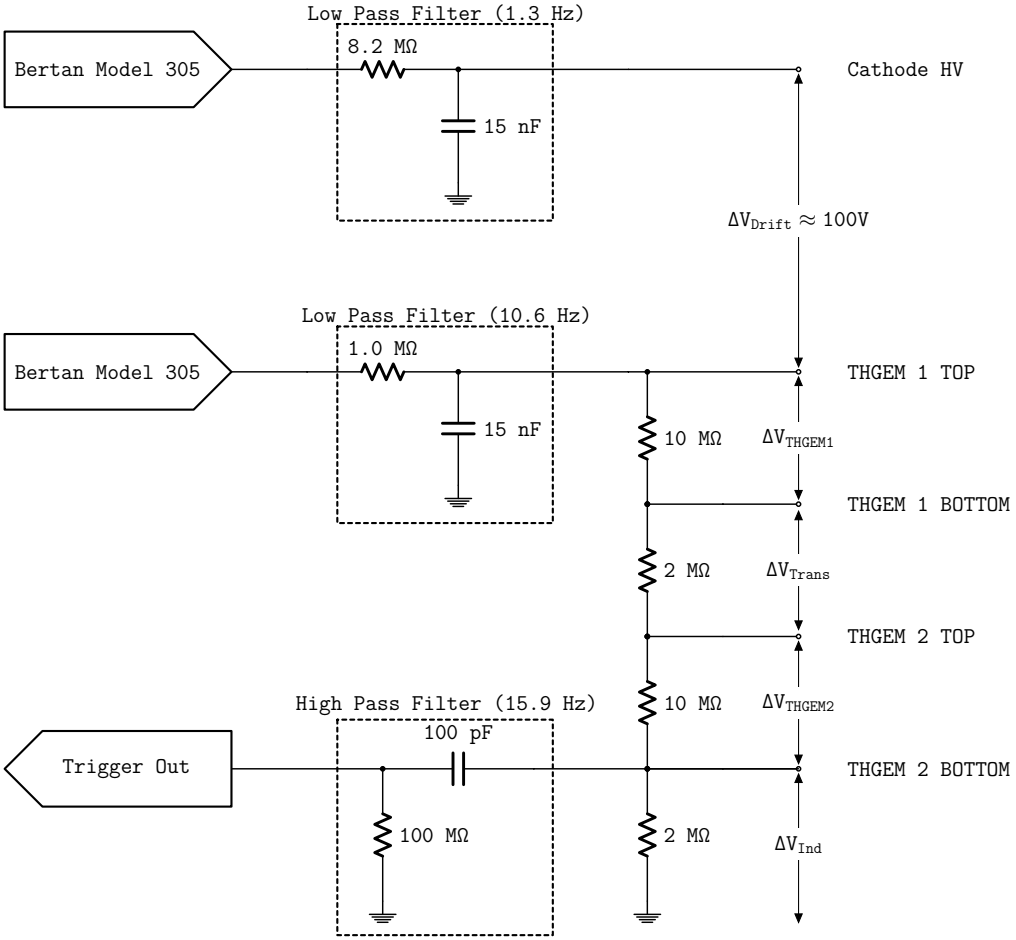

Figure 2.9: Schematic diagram of the high voltage (HV) circuit used to bias the THGEM imaging detector. The circuit is assembled using surface mount technology (SMT) components on a custom made PCB.

electrode can be used as a global trigger signal. This trigger signal is related to and precedes the anode signals by a few nanoseconds.

To extract the trigger signal from the bottom THGEM electrode, the DC component was filtered out using a high pass filter circuit. In the current configuration, the high pass filter was assembled using special high voltage capacitors and resistors. Mounted on the same PCB as the high voltage divider, the 100 pF capacitor and 100 MΩ resistor create a high pass filter with a low frequency cutoff at approximately 16 Hz. The resulting trigger signal, collected with a charge sensitive preamplifier, has a negative polarity and enough amplitude to discriminate it from the electronic noise.

2.4 Preamplifier Charge Calibration

To accurately measure the effective gain of the THGEMs, it was necessary to calibrate the electronics against known quantities of input charge. As illustrated in Figure 2.10, the pulse processing chain consists of a charge sensitive preamplifier (Ortec Model 109A), a linear pulse-shaping amplifier (Canberra Model 2020), and a multichannel analyzer (Ortec Model 927). Using a precision pulse generator (BNC PB-5), and an RC circuit, known quantities of charge can be injected directly at the preamplifier input. The RC circuit, housed in the charge injection box, is composed of a 1 pF capacitor and a 50 Ω resistor.

When the charge injection box is connected to the preamplifier input, the circuit behaves as an active differentiator. In this configuration, the output voltage (V_{OUT}) is directly proportional to the rate of change of the input voltage (V_{IN}) – see Equation 2.1.

$$V_{OUT} \propto \frac{dV_{IN}}{dt} \tag{2.1}$$

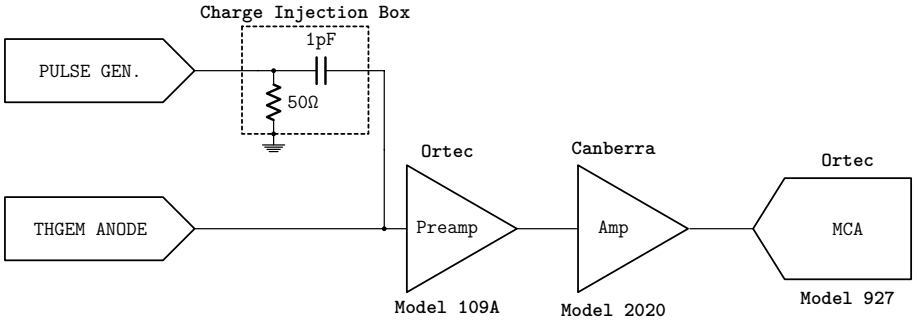

Figure 2.10: Pulse processing chain used to measure the effective gain of the THGEMs in the imaging detector.

Using either a square pulse or a tail pulse with a long decay time (>100 μs), the input pulse rate of change is equal to the rate of change in the charge (Q) stored across the input capacitor divided by the capacitance (C) – see Equation 2.2.

$$\frac{dV_{IN}}{dt} = \frac{1}{C} \times \frac{dQ}{dt} \tag{2.2}$$

Substituting Equation 2.2 into Equation 2.1 produces an expression for the output voltage in terms of the capacitance and the rate of change in charge.

$$V_{OUT} \propto \frac{1}{C} \times \frac{dQ}{dt} \tag{2.3}$$

If the RC time constant, of the charge sensitive preamplifier, is sufficiently longer than the rise time of the input voltage pulse, the output voltage is directly proportional to the charge stored on the input capacitor – see Equation 2.4. As an example, a 10 mV input voltage across a 1 pF capacitor will inject 10 fC of charge into the system.

$$V_{OUT} \propto \frac{Q}{C} \tag{2.4}$$

To calibrate the pulse processing chain, used in the effective gain measurements,

the amplitude of the pulse generator was varied between 20 mV and 200 mV producing input charges ranging from 20 fC to 200 fC. During this time, the linear amplifier was configured for a shaping time of 250 ns and a gain setting of 21. The resulting pulse height distribution was recorded for each input charge using the multichannel analyzer. By using a Gaussian function the centroid channel, corresponding to the average charge, could be calculated. The expression shown in Figure 2.11 was used to calculate the total collected charge following the amplification of primary electrons.

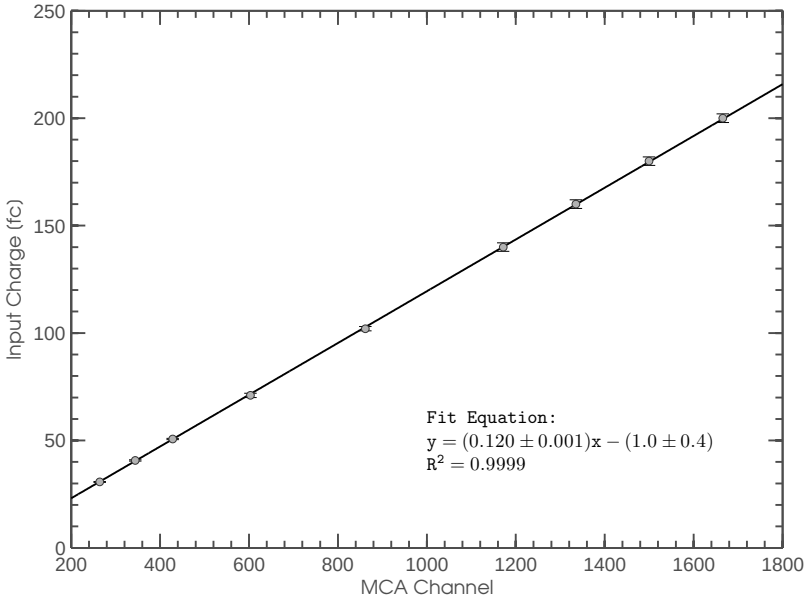

Figure 2.11: Charge calibration curve used to measure the effective gain of the THGEM amplifier. The linear amplifier had a shaping time of 250 ns and a gain setting of 21.

2.5 Effective Gain Measurements

With the pulse processing chain calibrated, the effective gain of the single and double THGEM configuration was measured. Defined as the ratio of collected charge to initial ionization charge, the effective gain is a metric frequently used to quantify

detector performance. To measure the effective gain, a Curium-244 source was located inside the detector. Curium-244 decays to Plutonium-240, by emission of an alpha particle, with a half-life of 18.11 years. The alpha particles, with a mean energy of 5.78 MeV, ionize the gas along their trajectory producing primary ionization electrons. These electrons are then focused towards the THGEM elements where they are multiplied through a Townsend avalanche and finally collected by the anode.

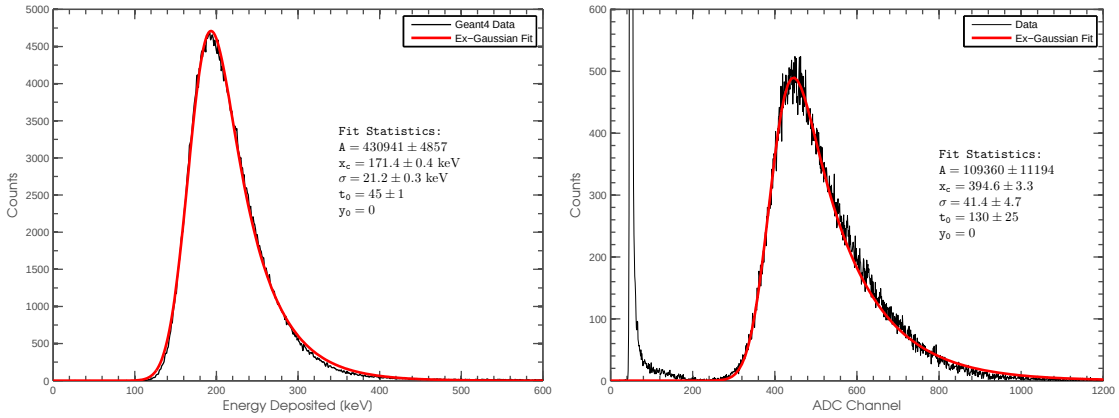

(a) **(b)**

Figure 2.12: Simulated (a) and measured (b) spectra of the energy deposition from ^{244}Cm alpha particles in the sensitive volume of a THGEM detector. The simulated spectrum was realized using a Geant4 simulation modelling a THGEM detector with 30% energy resolution. The measured results were collected from a 0.4 mm double THGEM setup biased to 1950 V.

To estimate the initial ionization charge, a Monte Carlo simulation was performed using the Geant4 toolkit. As illustrated by the spectrum in Figure 2.12 (a), the goal of the simulation was to determine the mean energy deposited in the sensitive volume from the ^{244}Cm alpha particles. Due to the energetic nature of the alpha particles and the low density of the detection gas, the mean energy deposited is 171.4 ± 0.4 keV. The average number of ion pairs can be estimated by dividing the mean energy deposited by the W-value of the gas. The W-value, defined as the

average energy lost by the incident particle per ion pair formed, is specific to gas composition. For TE-propane, various sources reference a W-value of 31.1 eV per ion pair per incident alpha particle (Kemmochi, 1976; Krajcar-Bronić and Srdoč, 1994). Using the aforementioned numbers, the average number of primary ion pairs formed is 5511. This value was used to compute the effective gain for each THGEM configuration.

$$\mathtt{f(x)} = \mathtt{y_0} + \frac{\mathtt{A}}{2\mathtt{t_0}}\mathtt{exp}\left(\frac{\sigma^2}{2\mathtt{t_0^2}} + \frac{\mathtt{x_c} - \mathtt{x}}{\mathtt{t_0}}\right)\left[1 + \mathtt{erf}\left(\frac{\mathtt{x} - \mathtt{x_c}}{\sigma\sqrt{2}} - \frac{\sigma}{\mathtt{t_0}\sqrt{2}}\right)\right] \tag{2.5}$$

A prominent feature in both the simulated and measured energy spectrum is the high energy tail – see Figure 2.12. The high energy tail is a consequence of imperfect collimation. Experimentally, the ^{244}Cm source was mounted above the Mylar cathode using a holder with a small collimation hole. Ideally, the ratio of hole diameter to depth would be really small for a good collimator. However, the count rate also suffers. As a compromise between count rate and collimation, the hole diameter and depth are both 3 mm. This geometry was also included in the simulation. The imperfect collimator allows alpha particle tracks which are longer than those emitted normal to the source surface. Since the stopping power is almost constant in this energy range, the energy deposited is directly proportional to the track length. Therefore, longer tracks deposit more energy. Due to the high energy tail, the spectrum could not be fit with a standard Gaussian function. To determine the peak position, it was necessary to fit the energy spectra with an Exponentially Modified Gaussian fit – see Equation 2.5. In this fit, $\mathtt{y_0}$ is the initial value, $\mathtt{A}$ is the area under the curve, $\mathtt{x_c}$ is the center of the Gaussian, σ is the standard deviation of the Gaussian and $\mathtt{t_0}$ is the skewness factor.

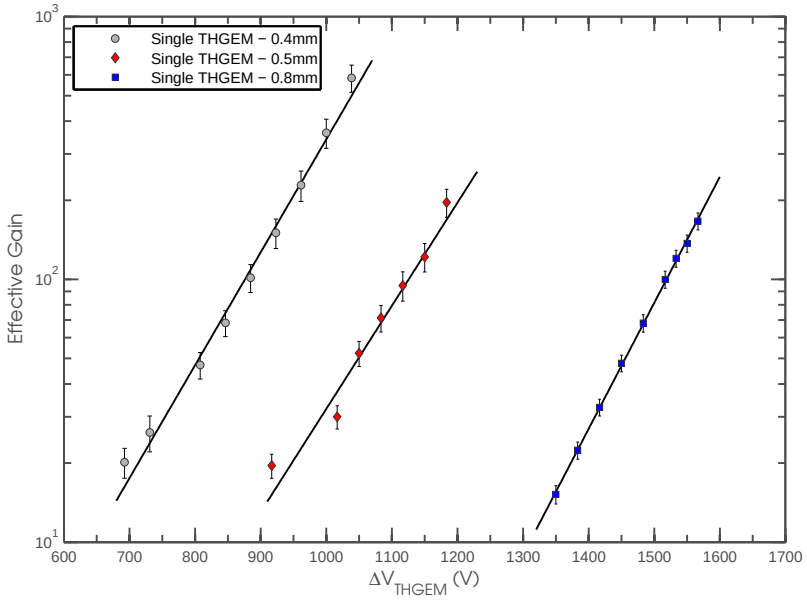

(a)

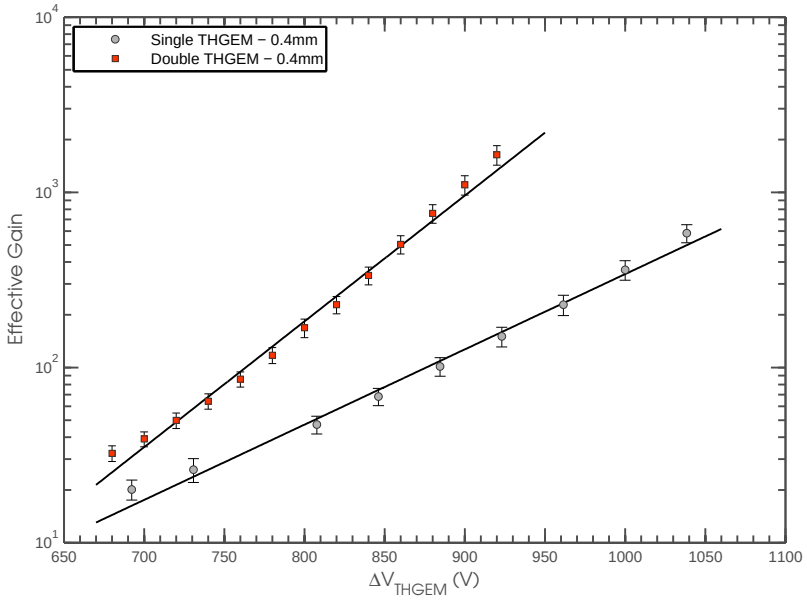

(b)

Figure 2.13: Effective gain curves of single (a) and double (b) THGEM configurations, in TE-propane at 167 Torr, measured with a ^{244}Cm source. Maximum achievable gains are limited by the onset of discharges due to reaching the Raether limit.

To measure the effective gain, the delay line anode was replaced with a large collection anode similar to the one described by Orchard (2010). With an active area of 42 x 42 mm^2, the collection anode integrates the charge emanating from the THGEM holes and sends the current pulse to the calibrated pulse processing chain. The results of the effective gain measurements for various configurations of single and double THGEMs are illustrated in Figure 2.13 (a) and Figure 2.13 (b), respectively. In all cases, the maximum achievable gain was determined by the onset of discharges due to reaching the Raether limit. In the single THGEM configuration, the highest gain was achieved by the 0.4 mm THGEM. This THGEM not only reached a gain three times higher than the others, but also proved to be the most stable. In the double THGEM configuration, the maximum effective gain was three times that of the single THGEM. However, the most important feature of this configuration is the ability to achieve a moderate effective gain (10^3) while keeping the bias relatively low.

2.6 Gain Stability

As previously mentioned, it has been reported that THGEMs with large etched rims (0.1 mm) have long stabilization times and large gain variations. In this thesis, the gain variation of the 0.4 mm THGEMs, in the single and double configuration, has been studied over a period of 24 hours. Using the same Cm-244 source, both configurations were biased for an effective gain which would give a peak sufficiently larger than the electrical noise but not high enough to be concerned with discharges. The single THGEM was biased for an effective gain of approximately 60 and the double configuration was biased for a gain of 120.

As illustrated by the plot in Figure 2.14, both configurations exhibit fairly long stabilization times. The double THGEM configuration was considered stable around

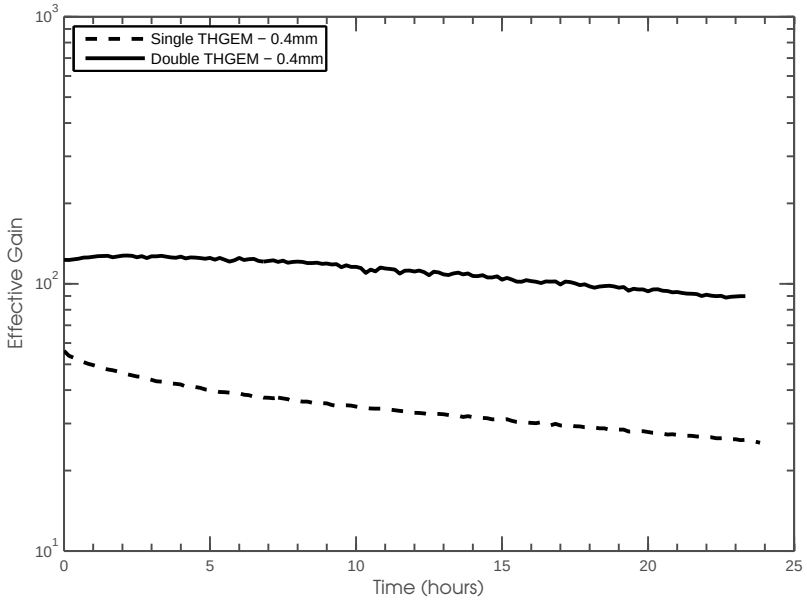

Figure 2.14: Gain stability of single and double THGEMs (0.4 mm), in TE-propane at 167 Torr, measured with a Cm-244 source over a period of 24 hours.

21–22 hours while the gain of the single THGEM continued to decline past 24 hours. Although the gain variation over a short time interval is negligible, the decline in gain over a long period is significant. At the end of the collection period, the gains of the single and double THGEMs had dropped to 33% and 66% of their respective initial values while the variation in high voltage was within 5% of the preset value. The long stabilization times are caused by the charging-up of the exposed insulator surface. Over time, slow positive ions accumulate on the top conductor, and exposed insulator surface, thereby reducing the local electric field. The reduced electric field manifests as a decrease in effective gain. This effect is not as prominent in the double THGEM configuration since there are two stages of amplification which can partially overcome the charging-up of the insulator. As a result of these measurements and the need for higher effective gain, it was decided the double THGEM (0.4 mm) configuration would be used for the electron amplification stage in the imaging detector.

Chapter 3

Development of the two-dimensional delay line based position sampling readout

A notable advantage of micropattern gas detectors (MPGDs), when applied to imaging studies, is in the diversity of two-dimensional readouts. By separating the electron multiplication stage from the readout stage, as in GEM/THGEM based detectors, the user has the flexibility of using any readout pattern which is appropriate for the specific application. Two of the most popular readout techniques, used in two-dimensional MPGDs, include the segmented anode and a timing based interpolation technique. In this chapter, I will contrast the two techniques by describing the development and performance of our two-dimensional delay line readout.

In the segmented anode readout, as described by Ziegler *et al.* (2001) and Bellazzini *et al.* (2007), the charge cloud formed following the amplification of primary electrons induces a current pulse on one or multiple readout pads. Using a reconstruction technique, such as the center-of-charge method, Bamberger *et al.* (2007) showed the interaction position can be determined with a spatial resolution nearing 50 μm. However, great care must be taken when designing the segmented anode. In a study performed by Kaminski *et al.* (2005), the authors suggest the shape of the readout pad limits the spatial resolution. An obvious solution to this problem is to

decrease the physical size of the pad and increase the number of pads at the readout anode. However, an increase in segmentation results in an increased number of readout channels, system complexity and cost. Consequently, segmented anode readouts are generally limited to small area imaging applications which desire multi-hit capabilities and the best spatial resolution.

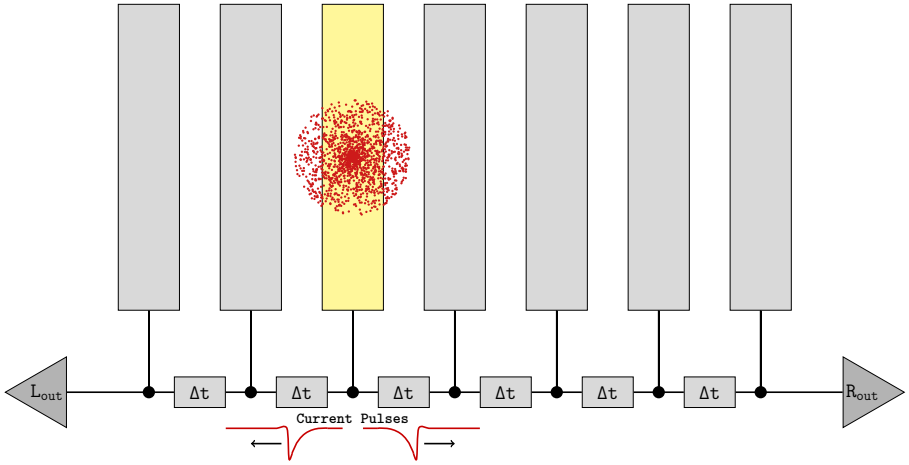

Figure 3.1: An example of an interaction collected with a one-dimensional readout based on the delay line method.

Timing based interpolation techniques, such as the delay line method, are frequently used in gas based position sensitive detectors (PSDs) for encoding the axial position of detected events. In a delay line readout, the charge sensing electrodes are directly connected to a transmission line. As illustrated in Figure 3.1, the charge cloud collected by one electrode induces two current pulses traveling towards opposite ends of the delay line. As the current pulses propagate through the delay lines, they experience a time delay proportional to the distance travelled from the point of incidence. Therefore, the interaction position can be interpolated from the relative time difference between pulse pairs corresponding to the same delay line.

A distinct advantage of delay line based charge sampling readouts is the reduced

system complexity associated with having a small number of readout channels. For a simple two-dimensional readout, the minimum number of readout channels is four. However, what this method gains in terms of reduced system complexity, it gives up in spatial resolution and multi-hit capability. Experiments by Guedes *et al.* (2003) and Zhou *et al.* (2009) have shown that a spatial resolution in the range of 150 μm to 300 μm is possible using standard GEMs with a dead time of a few microseconds. Consequently, delay line based charge sampling readouts have often been found in imaging applications which favour large active areas and reduced system complexity over spatial resolution and multi-hit capabilities.

The following sections describe the design, implementation and testing of our prototype two-dimensional, delay line based, charge sampling readout. The first two sections will focus on developing an understanding of the characteristics of electromagnetic delay lines and will describe an effective method for constructing these types of readouts. Next, the analog pulse processing chain and a custom amplifier circuit will be described. Lastly, a comparison will be made between the simulation results and experimental measurements of our delay line circuit.

3.1 Properties of the delay line

Depicted as passive four-terminal networks, electromagnetic delay lines have the property that signals impressed at the input terminals arrive at the output terminals with a characteristic time delay (Millman and Taub, 1956). Often created using inductors and capacitors, delays in the range of a few hundred picoseconds to hundreds of microseconds are possible. Longer delay times may be achieved using acoustical delay lines or active elements but they are outside the scope of this discussion.

Electromagnetic delay lines can be further classified as either distributed parameter or lumped parameter delay lines. Derived from the model of a uniform lossless transmission line, distributed parameter delay lines are often constructed using high quality coaxial cables. In coaxial cables, the central conductor possesses both inductance and resistance. Similarly, a capacitance is established as a result of the dielectric which separates the conductor from the outer shield. This combination of inductance and capacitance, distributed along the length of the coaxial cable, forms the distributed parameter delay line. However, relatively long cables are required to achieve delay lines of a few nanoseconds. Consequently, it is impractical to design a detector readout with a distributed parameter delay line.

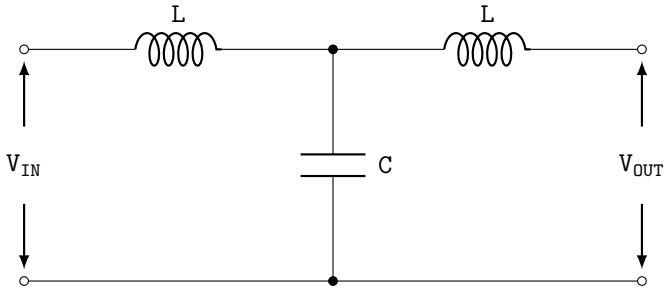

Figure 3.2: A single LC (T network) section of a lumped parameter delay.

Lumped parameter delay lines are an effective way of achieving delay lines with less attenuation and which occupy smaller volumes. Consisting of a series of symmetrical networks, such as the one illustrated in Figure 3.2, lumped parameter delay lines often resemble filters. When cascaded together, the inductors are connected in series while the capacitors connect between an inductor junction and ground. Lumped parameter delay lines can be connected along the various junctions (nodes) to produce incremental delay times. It is this property of lumped parameter delay lines which is used in the construction of our two-dimensional charge sampling readout.

In the sections to follow, the delay lines will often be discussed in terms of their nominal impedance (Z_0), the time delay per section of filter (t_d), and the cutoff frequency (ω_0). The cutoff frequency, ω_0, is the upper frequency below which the attenuation is zero. For a lumped parameter delay line, constructed from LC sections, the cutoff frequency is given as follows:

$$\omega_0 = \frac{1}{\sqrt{LC}} \tag{3.1}$$

If the spectral density (Fourier spectrum) of the input signal to the LC network consists of frequencies much less than ω_0, the output signal will be exactly the input signal except delayed by a time t_d.

$$t_d = \frac{1}{\omega}\left[\frac{\omega}{\omega_0} + \frac{1}{3}\left(\frac{\omega}{\omega_0}\right)^3 + ...\right] \approx \sqrt{LC} \tag{3.2}$$

Since the LC network is a filter, the characteristic impedance is not only a function of L and C, but also of the input frequency (ω) and the cutoff frequency.

$$Z_0 = \frac{\sqrt{\frac{L}{C}}}{\sqrt{1 - \left(\frac{\omega}{\omega_0}\right)^2}} \tag{3.3}$$

For input signals which contain frequencies much less than the cutoff frequency, the characteristic impedance is independent of frequency and reduces to the following.

$$Z_0 \approx \sqrt{\frac{L}{C}} \tag{3.4}$$

It is with the aforementioned characteristics of delay lines that our two-dimensional delay line based charged sampling readout was constructed.

3.2 Design of the one-dimensional delay line anode

Prior to designing the two-dimensional readout anode, a one-dimensional version was designed and fabricated. The purpose of the one-dimensional anode was to demonstrate the feasibility of using the delay line method for extracting positional information from detected events. Illustrated in Figure 3.3, the one-dimensional readout was realized on a 2-layer PCB with sampling electrodes which are 1.0 mm wide copper strips and have a pitch of 1.5 mm.

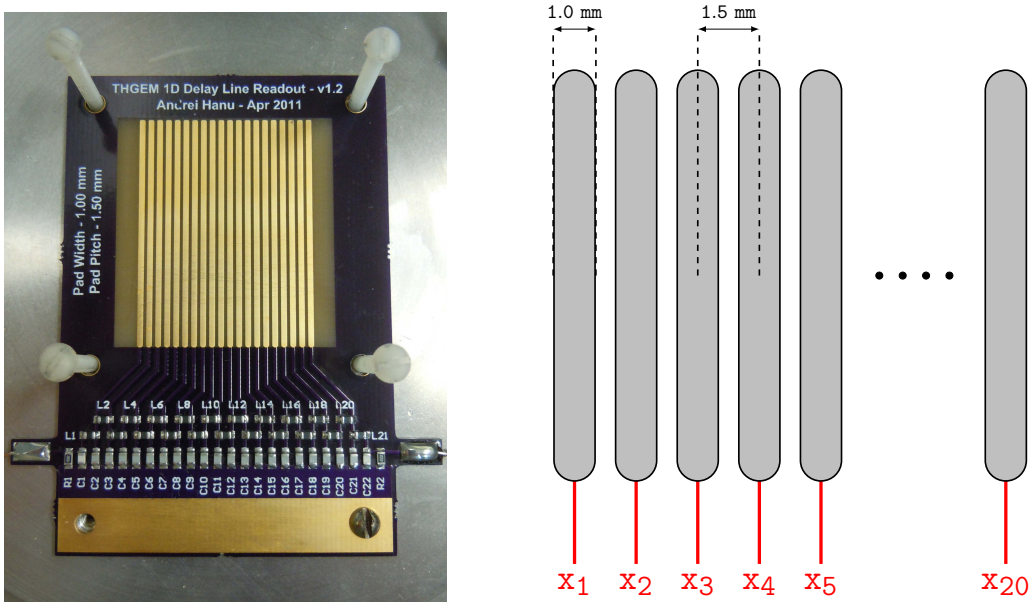

Figure 3.3: Image of the assembled one-dimensional delay line readout (a) realized on a 2-layer PCB. Illustrated in (b), the sampling electrodes are 1.0 mm wide copper strips with a pitch of 1.5 mm.

To extract positional information, the sensing electrodes are connected to a delay line consisting of 20 LC sections. As illustrated at the bottom of Figure 3.3 (a), the delay line is constructed using surface-mount (SMT) components. Due to their small size, SMT components are commonly found in modern electronics and are now the

standard method for producing delay lines which occupy small volumes. To extract the signals from the delay line, output pads are included at both ends which allow preamplifiers to be connected. Additionally, the delay line is physically grounded to the gas chamber with a small screw.

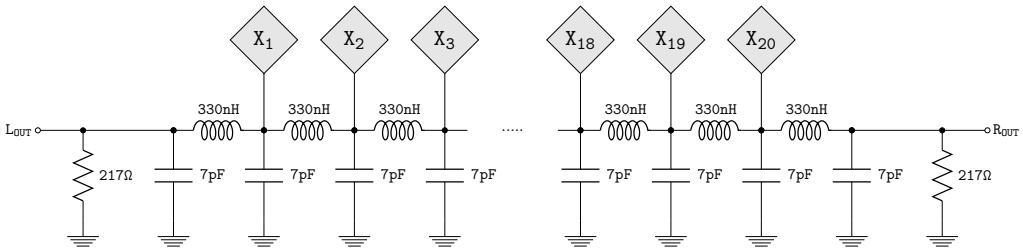

Figure 3.4: A circuit diagram of the delay line used in the one-dimensional readout anode. The 20 input nodes are individually connected to charge sensing electrodes.

Component values for our delay line are loosely based around LC values reported by Guedes *et al.* (2003). As illustrated in Figure 3.4, the delay line circuit consists of 20 LC sections ("*delay cells*") which are directly connected to the charge sensing electrodes. Using 0805 SMT components, each delay section has an inductor and capacitor with values of 330±33 nH and 7.0±0.5 pF, respectively. From the equations given in the previous section, this creates a delay line with a theoretical time delay per section of 1.5 ns, a cutoff frequency of 657 MHz, and a characteristic impedance of 217 Ω. To eliminate signal reflections, the delay lines are terminated inside the detector by a 217 Ω resistor. Prior to finalizing the component values used in the delay line, a simulation model of the circuit was constructed using the Tina-TI program, from Texas Instruments. The simulation model was used to measure the expected time delay as a function of input node and provided insight into the shaping of signals as they propagate through the delay line. In the last sections of this chapter, the results of the simulation model will be contrasted with experimental measurements.

3.3 Design of the two-dimensional delay line anode

An important step in designing the two-dimensional readout involves deciding on the size, shape, and orientation of the charge sensing electrodes. Many examples, including those described by Bachmann *et al.* (2002) and Guedes *et al.* (2003), have used sensing electrodes fabricated on two layer printed circuit boards (PCBs) and based around the image charge method. In such readouts, one set of sensing electrodes is placed on the top side of the anode while the other set is placed orthogonal to the first and on the bottom side of the anode. As the charge cloud induces a signal on the top electrodes, a similar signal of opposite polarity is induced on the bottom electrodes. However, due to unbalanced charge sharing between the top and bottom electrodes, these types of readouts are often plagued with signal-to-noise problems.

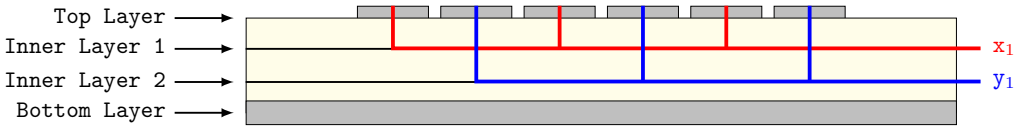

Figure 3.5: A schematic diagram showing the construction of a two dimensional charge sampling readout fabricated on a four layer PCB.

For our prototype THGEM based imaging detector, the two-dimensional readout board is based around a clever fabrication method first described by Barbosa (1996). In this method, a standard multilayer PCB is used in the construction of the readout anode. As illustrated in Figure 3.5, the charge sampling electrodes are implemented on the upper surface of a 4-layer PCB. Similar to a segmented anode, each element has a metal plated hole (via) connecting it to one of two sets of strips assembled on the inner layers. The first set of strips lie on the second layer and short circuit the electrodes which are related to one of the coordinates. The second set of strips lie on

the third layer and short circuit the electrodes related to the other coordinate. The bottom layer of the PCB is covered in a copper plane and forms the signal ground for the two-dimensional readout. Using this construction technique, the issue with charge sharing between coordinate electrodes has been circumvented.

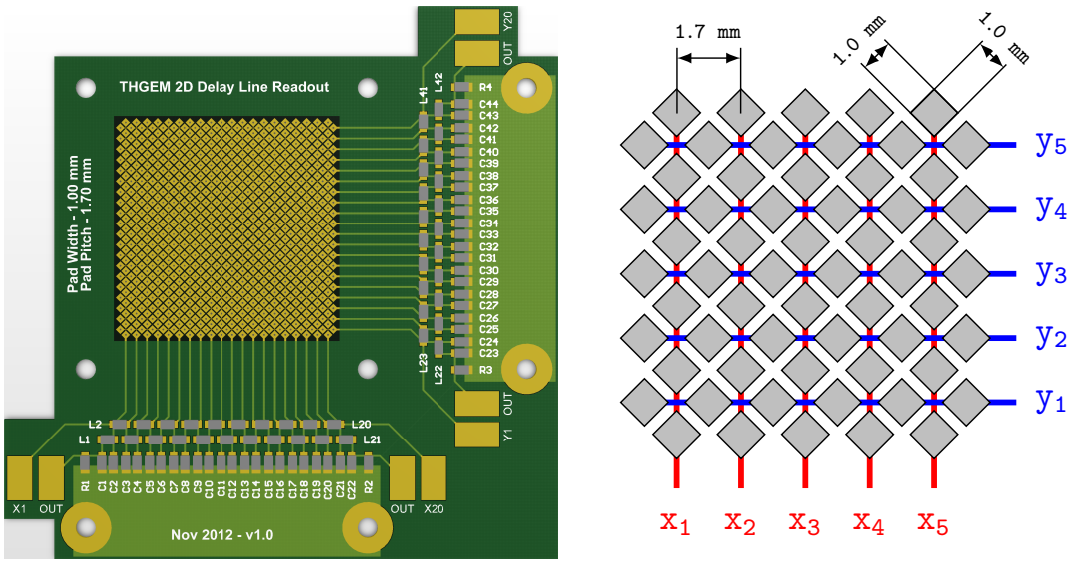

(a) (b)

Figure 3.6: The position sensing electrodes, shown in the 3D rendering (a), are constructed from diamond pads with plated holes connecting them to the internal traces of a 4-layer PCB. Illustrated in (b), a closeup of the sampling electrodes which are interconnected by orthogonal traces on the inner layers.

Following the aforementioned approach, our two-dimensional charge sampling readout was fabricated. As illustrated in Figure 3.6, the sensing electrodes are made from diamond pads with an area of 1.00 mm^2, a pitch of 1.70 mm, and cover a total area of 40 x 40 mm^2. Two-dimensional positional sensing was realized using two identical delay lines constructed using the same components as illustrated in Figure 3.4. Similar to the one-dimensional readout, each delay line has a pair of output signal pads and is physically grounded to the chamber body using a small screw.

3.4 Analog Signal Processing

As previously mentioned, the interaction position of an event in the THGEM imaging detector is obtained from the time taken by current pulses to travel to opposing ends of the delay line. Concerning our prototype two-dimensional readout, there are two delay line signals per axis for a total of four. As mentioned in Chapter 2, there exists an additional signal (trigger signal) from the bottom of the last THGEM which is coupled to and precedes the four timing signals. The pulse processing chain, illustrated in Figure 3.7 and described henceforth, generates the timing information necessary for the two-dimensional localization of each event.

The primary stage of the analog pulse processing chain, illustrated in Figure 3.8 (a), involves the extraction of signals from the bottom THGEM and the two delay lines. This step is accomplished with five Ortec VT120A preamplifiers. The VT120A preamps are fast timing preamps with 50Ω input and output impedance. As shown in Figure 3.10 (a), typical preamp output signals have an amplitude of a few tens of millivolts and are often buried in the electronic noise. To amplify the small preamp signals, and filter out some of the high frequency noise, a set of five homemade amplifiers was used. The homemade amplifiers, based around the OPA657 op-amp, have a bandwidth of approximately 80 MHz and a 50Ω input/output impedance. Following amplification from the homemade amplifiers, the signals are large enough to be discriminated out of the electronic noise by five Ortec Model 584 constant fraction discriminators (CFDs). The purpose of the CFDs is to extract arrival time information while negating the "*amplitude walk*" problem often found in leading edge timing. Output signals from the CFDs are logic signals and constitute the end of the analog pulse processing.

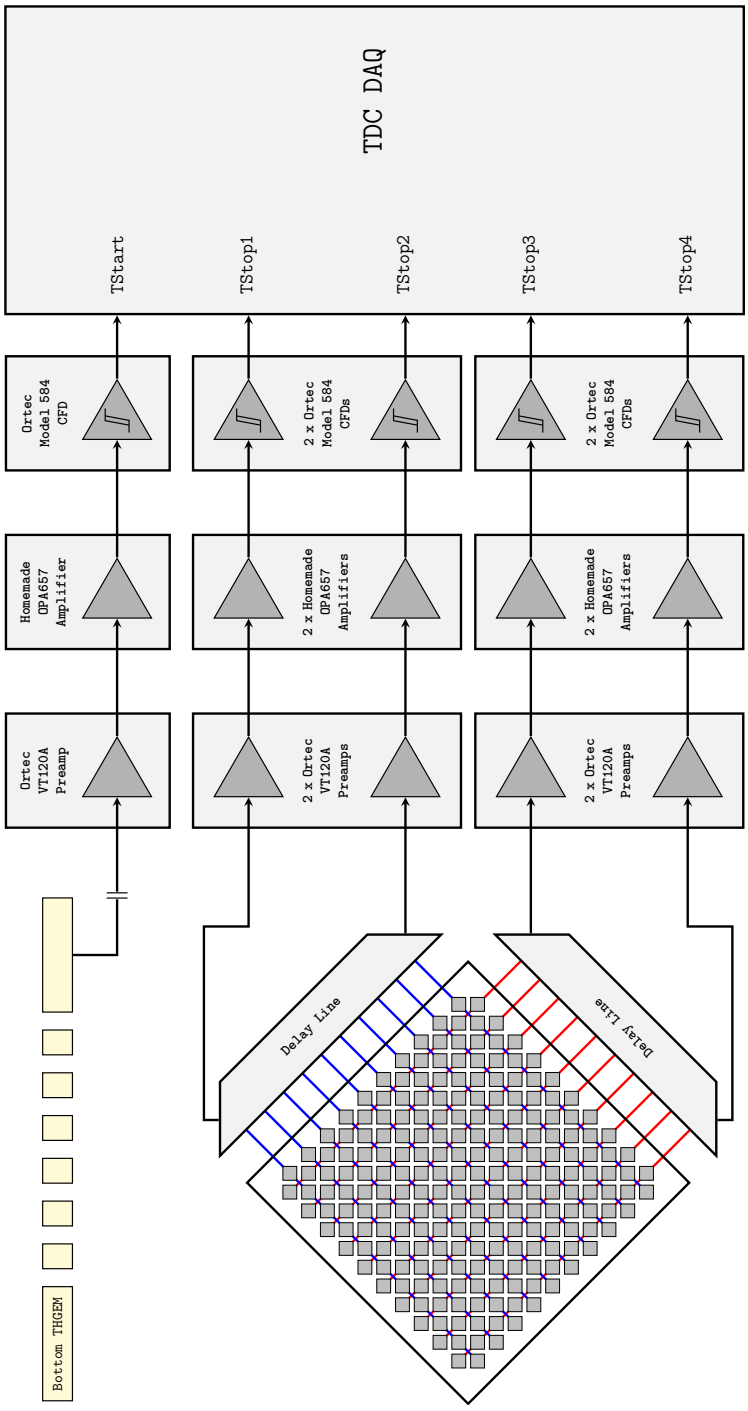

Figure 3.7: Schematic diagram of the analog pulse processing chain used by the two-dimensional delay line based THGEM imaging detector.

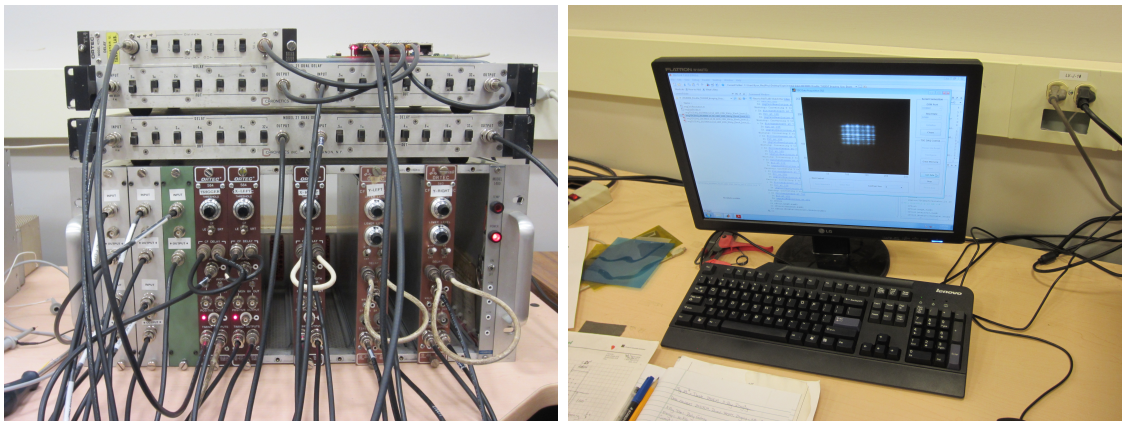

(a) **(b)**

Figure 3.8: Images of the analog pulse processing chain (a) and the data acquisition computer (b).

The final stage of the pulse processing chain consists of a time-to-digital converter (TDC) data acquisition (DAQ) system. The TDC DAQ, described thoroughly in Chapter 4, is a general purpose event reconstruction system which I developed for PSDs with delay line readouts. With the help of a TDC chip, the time difference between the trigger and four delay line signals is digitized. Following this, logic implemented on a Field Programmable Gate Array (FPGA) calculates the difference between signals originating from a common axis and increments the memory location corresponding to the reconstructed event position. At the end of the acquisition cycle, images stored on the memory of the TDC DAQ are transfer to the local memory of the PC for viewing – see Figure 3.8 (b). The image files produced contain 1024 x 1024 square pixels with a pixel depth of 32-bits.

3.5 Development of the homemade amplifiers

To interface the output signals from the delay line readout with the timing pickup electronics used in the pulse processing chain, it was necessary to develop a set of five

pulse amplifiers – see Figure 3.9. As illustrated in Figure 3.7, the homemade amplifiers are located between the Ortec VT120A preamplifiers and the Ortec Model 584 CFDs. The primary function of the amplifiers is to provide the necessary amplification for the preamp output signals in order to effectively trigger the CFDs. Additionally, the amplifiers improve the signal-to-noise ratio by filtering a portion of the high frequency noise.

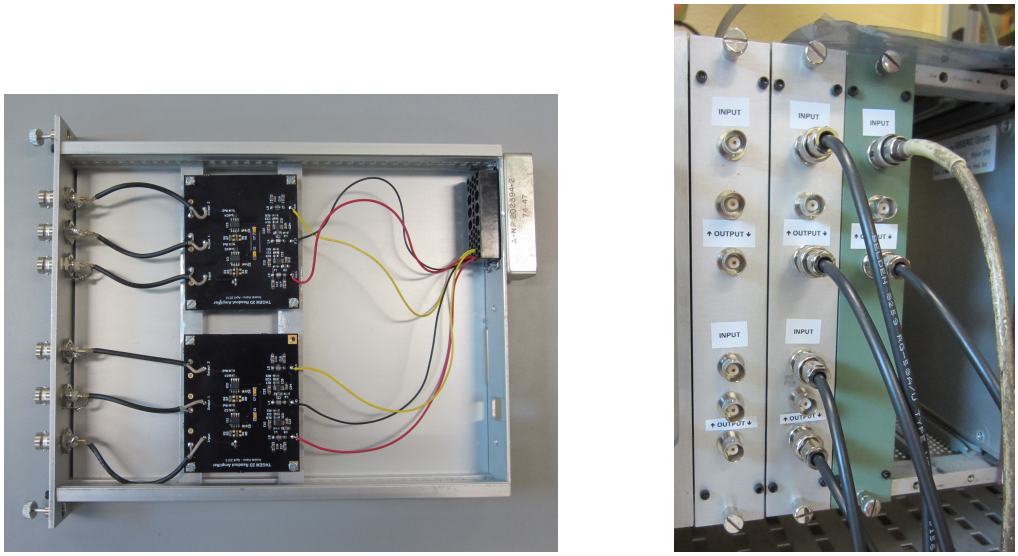

(a) **(b)**

Figure 3.9: Images of two pulse amplifier units (a), in the non-inverting configuration, and all five pulse amplifiers (b) installed in a NIM crate.

Due to their location in the pulse processing chain, the input and output requirements of the amplifiers are driven primarily by the preamplifiers and CFDs. To effectively transfer the fast timing signals, the input and output impedance of the amplifiers should match those of the preamps and CFDs, respectively. Consequently, the amplifiers have been designed with an input and output impedance of 50Ω. Additional requirements considered during the design phase include signal bandwidth, desired gain, and additional filtering.

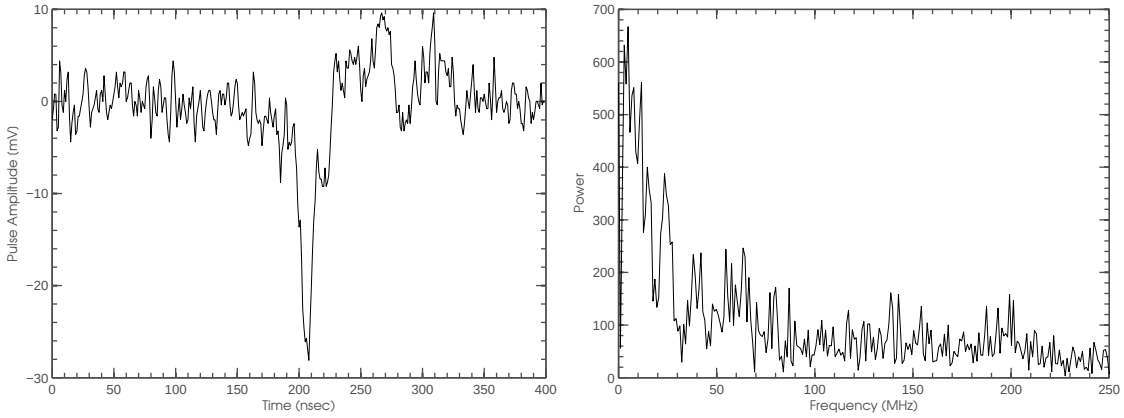

Figure 3.10: Example of a typical delay line pulse (a) and the associated power spectrum (b). The pulse was generated by alpha particles amplified by a double THGEM (0.4 mm) setup biased to -2260 V.

The Ortec VT120A is a fast timing preamplifier used to read out the small current pulses from the two-dimensional delay line readout. As illustrated in Figure 3.10 (a), typical timing pulses from the delay line readout have a negative polarity, an amplitude of a few tens of millivolts and a pulse width of approximately 25 ns. The power spectrum, shown in Figure 3.10 (b), indicates that most of the fundamental frequencies are below 50 MHz. To allow for some variation in signal shapes, the amplifiers were designed with a bandwidth of approximately 100 MHz. Finally, taking into consideration the range of pulse amplitudes and flexibility in setting the CFD threshold, necessitated a gain of approximately 40 dB.

Once the input, output, bandwidth and gain requirements were established, it was necessary to select an operational amplifier (op-amp) which would match these needs. The OPA657, from Texas Instruments, is a voltage-feedback op-amp with a high gain bandwidth product, low input noise, and low distortion. With regards to small signal amplification, the OPA657 has a bandwidth of 275 MHz at a gain of +10, slew rate

of 700 V/μs, and rise/fall times of 1 ns. Due to the excellent gain bandwidth product and fast rise/fall times, it was decided the OPA657 would be the ideal op-amp for amplifying the preamp output signals.

Although a single OPA657 can be safely configured for high gains (> 50), the frequency response of the op-amp drops off dramatically. For example, when configured for a gain of 50, the frequency response shows a first order low pass filter with a cutoff at approximately 32 MHz. Including the parasitic capacitance of the PCBs, would further reduce the response until it is very close to the signal bandwidth of the signal being amplified. Since a high gain is desired, it was determined that two back-to-back OPA657 op-amps would be needed. In such a configuration, the overall gain is given by the product of individual op-amp gains. Additionally, operating at lower gains (< 20) benefits from a broader frequency response, higher slew rates and results in an overall faster amplifier.

As illustrated in Figure 3.11 (a), the final amplifier design features back-to-back OPA657 op-amps configured for relatively low absolute gain. To allow flexibility in input signal polarity, each op-amp can be wired in both the inverting and non-inverting configuration. As shown in Table 3.1, the amplifiers are configured by connecting the appropriate resistors to the op-amp inputs. Additionally, since the op-amps are wired in series, two output gains are possible. Outputs 1 and 2 provide a signal output following one or two stages of amplification. Finally, the amplifiers can be configured as active filters. When adding a capacitor in parallel with the feedback resistors, the amplifiers function as low pass filters. In the default configuration, each op-amp has a feedback capacitance (Cf1 & Cf2) of 2 pF giving a low pass filter with a cutoff frequency of approximately 160 MHz. In either configuration, inverting and

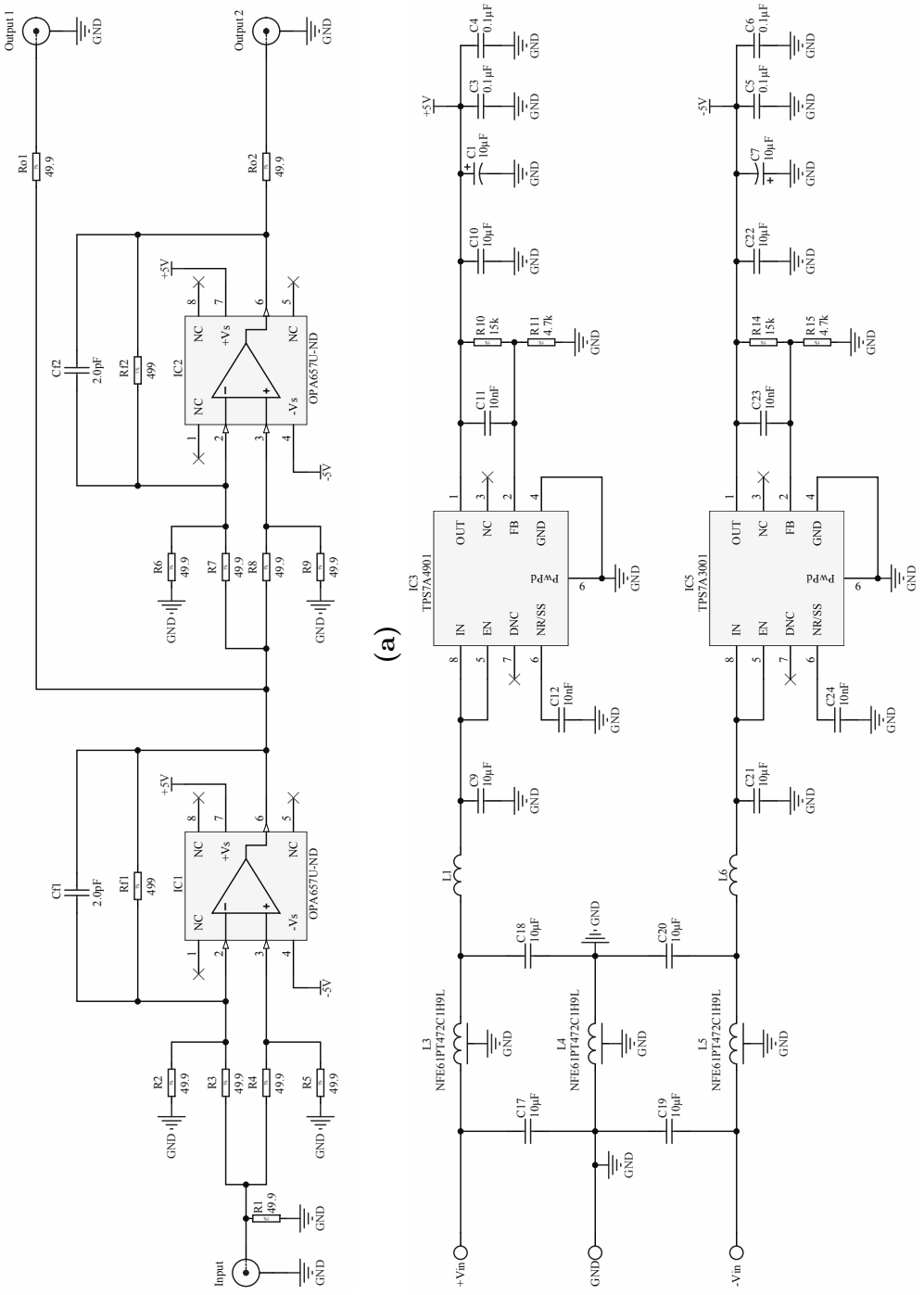

Figure 3.11: Schematics for the pulse amplifier circuit featuring back-to-back OPA657 op-amps (a) and the necessary power regulation (b) and filtering.

non-inverting, the amplifiers have shown to be stable with a feedback capacitance of up to 8 pF.

Table 3.1: Typical component values used to configure the pulse amplifier in inverting (G = -110) and non-inverting (G = +121) modes.

Component	Inverting	Non-Inverting
R1	–	49.9Ω
R2	–	49.9Ω
R3	49.9Ω	–
R4	–	0Ω
R5	0Ω	–
Cf1	2pF	2pF
Rf1	499Ω	499Ω
Ro1	49.9Ω	49.9Ω
R6	49.9Ω	49.9Ω
R7	–	–
R8	49.9Ω	0Ω
R9	–	–
Cf2	2pF	2pF
Rf2	499Ω	499Ω
Ro2	49.9Ω	49.9Ω

To power the two OPA657 op-amps, it was necessary to supply them with well filtered -5/+5 V. To accomplish this, two ultra low noise linear power regulators were used. The TPS7A4901 and TPS7A3001, from Texas Instruments, function as the positive and negative voltage converters for the power regulation circuitry. For ease of integration with the rest of the pulse processing chain, the amplifiers were designed to fit inside standard size NIM modules. As such, input power to the amplifier circuits comes from the -12/+12 V supply rails of the NIM bin. To minimize power supply noise from other modules plugged into the same NIM bin, the supply rails have additional filtering in the form of a Butterworth low pass filter. The filter, constructed as an LC pi network, has been specifically designed to improve high-frequency attenuation. As a result of careful power supply design, the low input noise of the OPA657 has been preserved.

Prior to finalizing the PCB design for the amplifiers, an analog simulation was developed to study the various parameters which describe the performance of each configuration. The Tina-TI program, by Texas Instruments, offers high quality SPICE models for a large range of op-amps including the OPA657. Using this program, the frequency response and expected overall gain was accurately simulated. As illustrated in Figure 3.12, the frequency response of both configurations, inverting and non-inverting, are quite similar. In both cases, following two stages of amplification (Output 2), the frequency response shows a 2^{nd} order low pass filter with a cutoff at approximately 80 MHz. The frequency response following a single amplification stage (Output 1) shows a higher cutoff frequency of approximately 130 MHz. Finally, as illustrated by the ordinate of each plot, the expected gains of the inverting and non-inverting configurations are -40.8 dB and +41.6 dB, respectively.

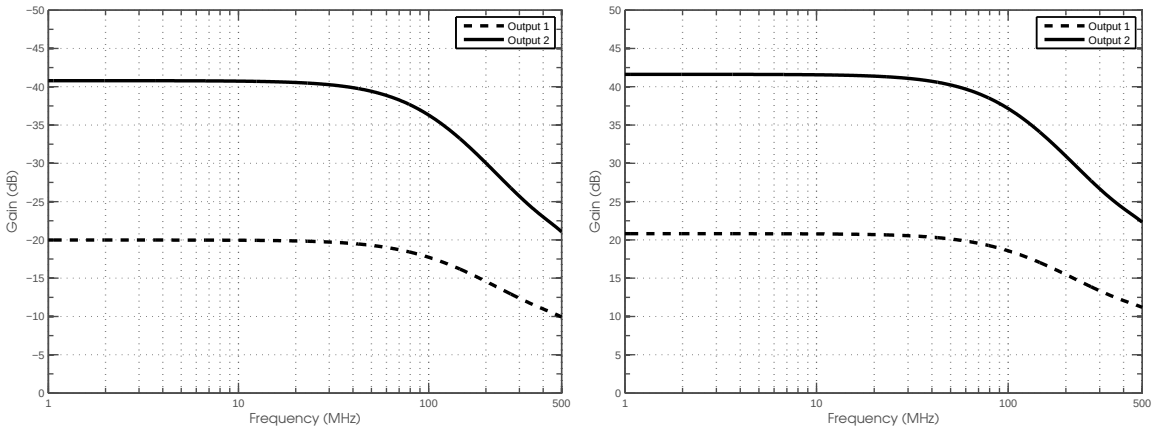

(a) **(b)**

Figure 3.12: Frequency response of the OPA657 based pulse amplifier circuits, simulated with the Tina-TI SPICE models, in the inverting (a) and non-inverting configuration (b).

Once the amplifiers were assembled, their performance was tested using a precision pulse generator (BNC PB-5). With the trigger and delay line amplifiers configured

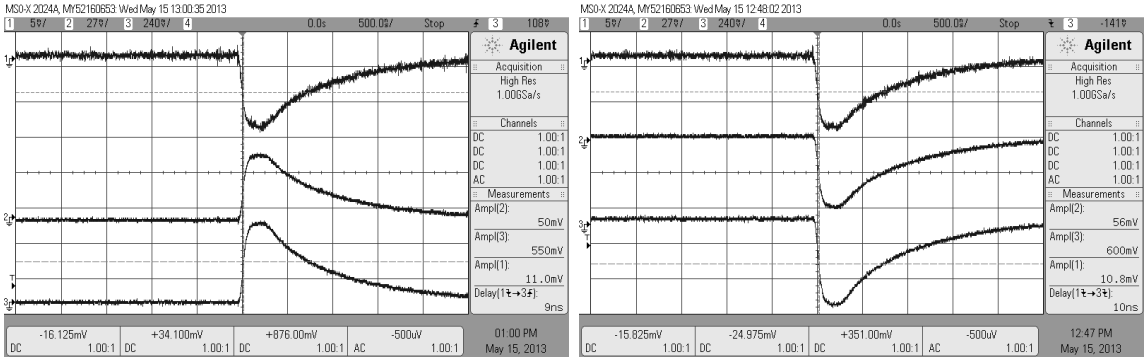

(a) **(b)**

Figure 3.13: Oscilloscope captures of the trigger (a) and delay line (b) amplifiers. Output signals are terminated at the oscilloscope inputs into 50 Ω.

in the inverting and non-inverting modes, the effective voltage gain and propagation delays were measured. As illustrated in Figure 3.13, the trigger and delay line amplifiers were evaluated using input pulses of -11.0 mV and -10.8 mV, respectively. On the trigger amplifier, the first stage of amplification is inverting and produces a 50 mV output pulse. The second stage is non-inverting and results in 550 mV pulses. Using these values, the effective gain of the trigger amplifier is shown to be -33.9 dB. Similarly, the delay line amplifiers have a gain of +34.9 dB. In the pulse processing chain, the CFD inputs are terminated into 50Ω. Similarly, the amplifier output signals were terminated at the oscilloscope inputs. The termination reduces the signal amplitudes by approximately 6 dB and explains the discrepancy between the measured and expected gain. Lastly, the propagation delay of each amplifier configuration was measured. The results of these measurements indicate that the trigger and delay line amplifiers have a propagation delay of 9 ns and 10 ns, respectively. For the purposes of the THGEM imaging detector, the actual magnitude of the propagation delay is not important as long as the trigger and delay line signals have a consistent propagation delay between them.

3.6 Time delay measurements

When used to encode the position of detected events, one of the most important parameters of delay lines is the relative time delay (t_r) as a function of input node. As referred to hereinafter, the relative time delay is calculated by subtracting the time for pulses to reach the right output from the time to reach the left output – see Equation 3.5. Therefore, input nodes closer to the left side of delay line have negative relative time delays while the right most input nodes have positive relative time delays.

$$t_r = L_{OUT} - R_{OUT} \tag{3.5}$$

Prior to finalizing the design of the delay lines, a simulation model was constructed in the Tina-TI SPICE program. Although the theoretical models of a delay line are certainly adequate, the simulation can be used to assess the impact of equivalent series resistance from inductors and the parallel resistance of capacitors. To simulate the expected relative time delay, an input pulse with an amplitude of -1 V and a width of 30 ns was sequentially connected to each of the 20 input nodes to the delay line. In addition to the component values in Figure 3.4, a small series resistance (0.4 Ω) was added to each inductor. The parallel resistance of the capacitors was unknown and therefore not included in the simulation. Using the aforementioned equation, the relative time delay was calculated for each input node.

Once assembled, the two delay lines used in the two-dimensional anode were characterized. Following a similar approach to the above, the relative time delay of each delay line was measured. Input pulses, generated from a precision pulse generator (Model PB-5, Berkeley Nucleonics Corporation), had an amplitude, rise time, and fall

time of -1.00 ± 0.02 V, 66 ± 4 ns, 1.7 ± 0.1 μs, respectively. Although the shape of the experimental input pulses differs from the simulation, they are slower and therefore should not be filtered any further than the simulation pulses.

As illustrated in Figure 3.14, both the simulation and experimental measurements reveal some interesting results. First, each of the input nodes can be distinctly identified from adjacent nodes without any overlap. This is important when trying to discern objects nearing in size to the pad pitch. Next, the relative time delay of both delay lines show almost perfect linearity with only minor deviations near the ends. Non-linearities in the relative time delay can result in distortions, such as barrel or pincushion, which have to be corrected in post-processing. Lastly, the measured and simulated relative delay times differ quite significantly towards the ends of the delay line. This can be partially explained by the stray capacitance, from the electrodes, which is in parallel with the delay line capacitance. Without further modeling of the sensing electrodes, this stray capacitance is difficult to calculate and was omitted from the simulation model. This additional capacitance increases the time delay per LC section and decreases the cutoff frequency of the delay line.

3.7 Effects on signal rise time

The variation of time delay between adjacent cells can be explained by the changing signal rise time as the current pulse propagates through the delay line. As illustrated in Figure 3.15, a precision pulse generator was used as input to one end of the delay line while the other end was left terminated. The input signal had an amplitude, rise time, and fall time of -1.36 ± 0.02 V, 66 ± 4 ns, 1.7 ± 0.1 μs, respectively. Using an oscilloscope, the output signal at each of the 20 delay line nodes was recorded and analyzed.

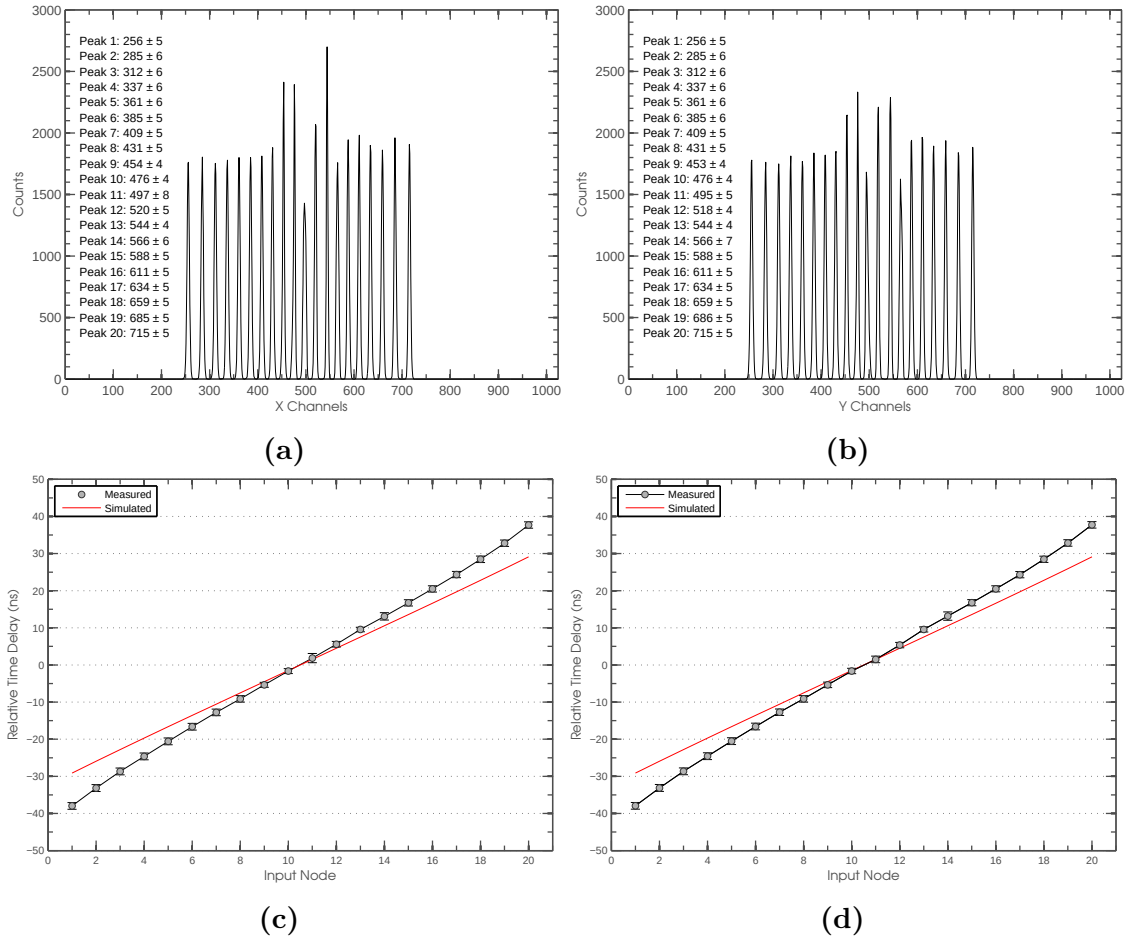

Figure 3.14: The distribution of counts used to characterize the x-axis (a) and y-axis (b) delay lines. Relative time measurements are compared with simulation results in (c) and (d).

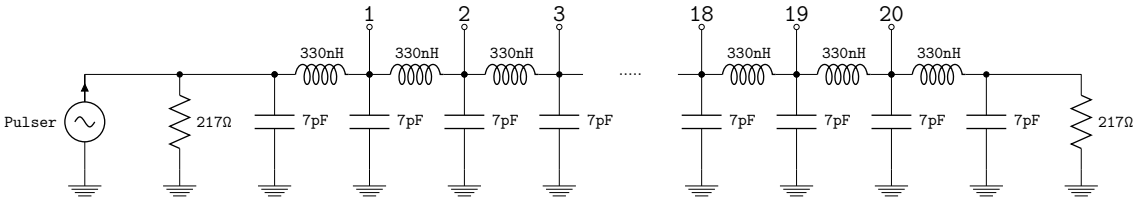

Figure 3.15: Schematics of the delay line configuration for measuring the signal rise time as a function of the number of delay cells.

The results of these measurements provide insight into the edge effects of delay lines. As illustrated in Figure 3.16, as the input signal progresses through a larger number of delay cells it experiences a change in rise time. In our 20 cell delay line, the effect becomes drastic following 10 delay cells. The changing rise time would not be a problem if it was consistent for both delay line pulses. However, that is not the case. For interactions near the edge of the delay line readout, one pulse always traverses a larger number of delay cells than the other. Consequently, it experiences a significant change in rise time. This changing rise time becomes a problem for the timing pickup electronics. The CFDs, used in the pulse processing chain, are implemented to deal with variations in signal amplitude and not rise times. A change in signal rise time will cause the CFDs to output a pulse later than expected, and artificially inflate the measured delay time.

By this stage, it should be rather clear that a delay line is primarily a filter which has the property of introducing a time delay between input and output signals. Each cell of the delay line is a low pass filter with a specific cutoff frequency. The result of lumping a given number of LC sections is an N-th order low pass filter, where N is the number of delay sections. Lower order filters have smoother transitions at the corner frequency and as a result do not change the signal shape as drastically as higher order filter. Higher order filters, such as those produced by 10 or more LC

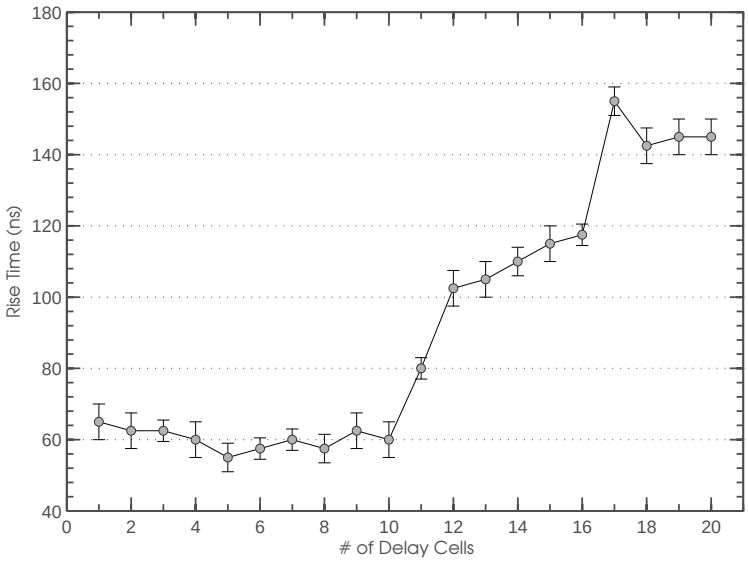

Figure 3.16: A plot of output signal rise time versus the number of delay line cells. An input signal with amplitude, rise time, and fall time of -1.36 ± 0.02 V, 66 ± 4 ns, and 1.7 ± 0.1 μs, was used.

sections, have a sharp cutoff at the corner frequency and significantly alter the rise time of fast signals.

To enhance the response of the delay line readout, the following suggestions are recommended. First, the THGEM signal should be thoroughly studied prior to designing any future delay line based readouts. It should be understood that the gas mixture has a great impact on the development of the THGEM signal. Consequently, it is the spectral density of the THGEM signal which dictates the bandwidth of the delay line circuit and not the other way around. Next, the bandwidth of the delay line circuit should be large enough to negate the effects of higher order filtering. Lastly, a few delay cells should be included to either end of the delay line. These additional delay cells, which are not connected to with readout electrodes, will increase the filtering experienced by signals close to the edges and hopefully mitigate this effect.

Chapter 4

Development of the TDC based event reconstruction system

To process the timing signals associated with the delay line based THGEM imaging detector, a time-to-digital converter (TDC) data acquisition (DAQ) system was developed. The TDC DAQ digitizes the timing signals generated from the delay line readout, calculates the difference between signals originating from a common axis, and increments the memory location corresponding to the reconstructed event position. In order to select the hardware for the TDC DAQ, it was necessary to establish the required timing resolution, throughput rate, and processing capabilities of the system. Based upon the timing characteristics of the delay line readout, a resolution of less than a nanosecond is required to distinguish signals originating from adjacent positions on the same delay line. This criteria was far exceeded by all of the TDCs available, with most offering timing resolution better than 100 ps. The required throughput rate was determined by evaluating available literature for the count rate capabilities of similar imaging systems. Investigations into GEM based imaging detectors, by Cortesi *et al.* (2007) and Zhou *et al.* (2009), demonstrated counting capabilities up to 10^5 counts per mm^2 per sec. Extrapolating to a THGEM detector with an active area of 1600 mm^2 (4 cm x 4 cm) requires electronics which

can handle event rates greater than 100 MHz. Since such high count rates were not desired, it was decided that the system should handle at least 10^4 counts per sec over the entire area of the prototype THGEM detector. As is described in later sections, this proposed counting rate is exceeded by a factor of 100. Finally, the system is required to process the TDC measurements and reconstruct the event position. For this task, it was decided the TDC measurements should be processed by a Field Programmable Gate Array (FPGA) connected to external memory. Using FPGAs, allowed for a system capable of running the acquisition process and event reconstruction in parallel. The ability to process events in parallel results in throughput rates of a few MHz.

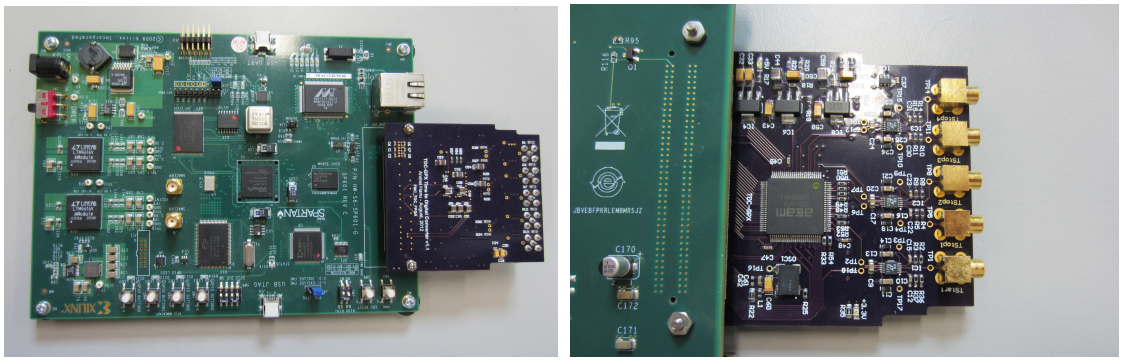

(a) **(b)**

Figure 4.1: Pictures of the entire event reconstruction system including the Xilinx SP601 carrier board (a) and a closeup image of the assembled TDC DAQ module (b).

Due to the abundance of FPGA development kits currently available, the TDC DAQ was designed as a universal plugin module. The Xilinx SP601, featuring a Spartan 6 FPGA and 128 MB of DDR2 memory, is an entry-level FPGA development kit and it functions as the carrier board for the TDC event reconstruction system (see Figure 4.1). The TDC-GPX, from Acam messelectronic, was the TDC selected for

this design. Following the VITA 57.1 standard VMEbus International Trade Association (2008), the TDC-GPX was implemented on a 4-layer PCB (see Figure 4.2) along with all of the necessary input circuitry. Compliance with VITA 57.1 guarantees the TDC DAQ can be used with FPGA development kits which posses the necessary connectivity. By adopting a modular design philosophy, the time required to prototype the TDC DAQ event reconstruction system was significantly reduced.

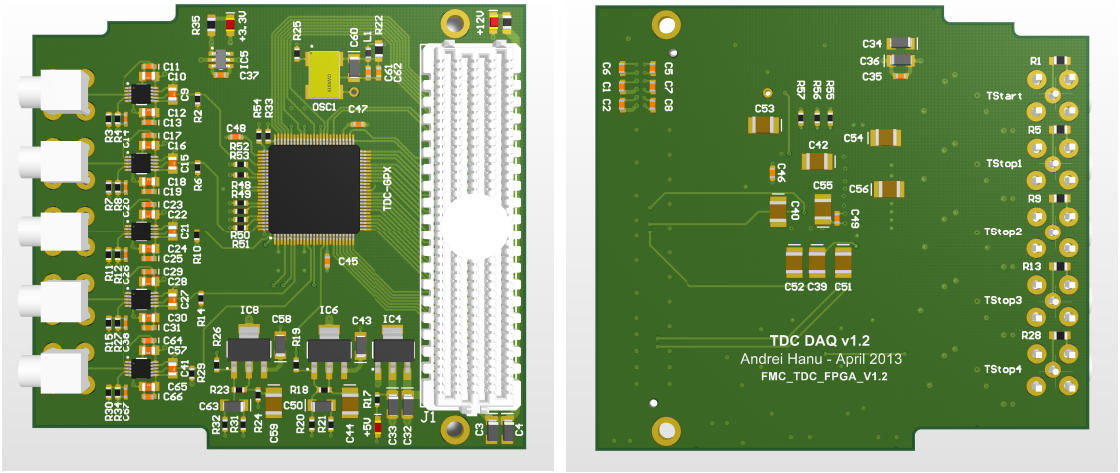

(a) **(b)**

Figure 4.2: Pictures of the (a) top and (b) bottom of TDC DAQ module realized on a 4-layer PCB. The TDC DAQ interfaces with FPGA development kits through the FMC connector pictured at the right of the module.

The first two sections of this chapter describe the hardware design and implementation, of the TDC DAQ module, followed by the development of the FPGA firmware. Next, the PC software which controls and communicates with the TDC DAQ event reconstruction system is presented. Finally, the use of an external pulse generator allowed for measuring the continuous throughput rate, integral non-linearity (INL) and differential non-linearity (DNL) of the system. The results of these measurements are an indication of the system performance and are discussed in the closing sections.

4.1 Hardware Architecture

The primary role of the TDC DAQ module is to process the timing signals associated with the delay line based THGEM imaging detector. To accomplish this task, the TDC DAQ module must include a TDC, the appropriate signal interfacing circuitry, and a high speed connector. As illustrated in Figure 4.3, the hardware architecture of the TDC DAQ module consists of a single TDC-GPX application-specific integrated circuit (ASIC), five NIM-to-LVTTL converter circuits, and an FPGA Mezzanine Card (FMC) low pin count (LPC) connector.

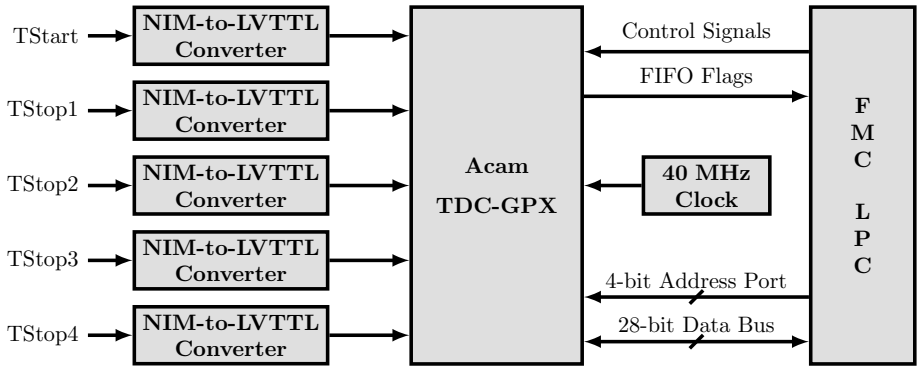

Figure 4.3: The hardware architecture of the TDC DAQ module.

In order to comply with the VITA 57.1 standard, the TDC DAQ module must include an FMC connector. FMC connectors were developed by a consortium of companies ranging from FPGA vendors to end users. The purpose of this connector is to provide the necessary high speed connectivity between FPGA systems and user developed expansion modules, such as the TDC DAQ. One of the primary advantages of the VITA 57.1 standard is design reuse and system flexibility. Employing a modular design philosophy allows the TDC DAQ event reconstruction system to be implemented using many of the available FPGA carrier boards complying with the

VITA 57.1 standard. The TDC DAQ module reduces the time to design a complete system while retaining nearly all of the features often found in purpose-built systems.

To interface the fast NIM signals to LVTTL signals, required by the TDC-GPX, a signal conversion circuit was developed. The design and implementation of the five NIM-to-LVTTL converter circuits and some key features of the TDC-GPX ASIC will be discussed in the following subsections.

4.1.1 TDC ASIC

The TDC ASIC chosen for this design is the TDC-GPX model from Acam. Featuring one common start and 8 independent stop channels, the TDC-GPX can be configured in one of four operating modes. In I-mode, as configured on the TDC DAQ, the TDC-GPX has a 17-bit measurement range. With a typical time resolution of 81 ps, the TDC-GPX can be configured for temperature stable resolutions between 64 ps and 113 ps. Using a proprietary communication protocol, employed over a 28-bit data bus and 4-bit address port, internal registers on the TDC-GPX can be used to configure the operating mode, resolution, edge sensitivity, and length of the measurement window.

Since the high resolution of the TDC-GPX is achieved through internal gate propagation delays, the resolution exhibits sensitivity to changes in core voltage and temperature unless stabilized. In resolution adjust mode, temperature stability is achieved by regulating the core voltage against temperature fluctuations. At the maximum operating temperature the maximum core voltage is reached while the minimum core voltage is reached at the lowest temperature. Regulation of the core voltage is achieved by controlling an external signal connected to the power supply.

The feedback control signal is generated by an internal phase locked loop (PLL) circuitry. As shown in Figure 4.3, an external 40 MHz clock is used for generating the PLL frequency and resolution calibration. Using this scheme, the TDC-GPX achieves temperature stable timing resolution between -40°C and +125°C.

4.1.2 NIM-to-LVTTL Converter

In I-mode, as configured on the TDC DAQ, the TDC-GPX requires input signals of the LVTTL type. Timing pickup electronics, which are used in the delay line readout, provide output signals of the fast NIM type. Therefore, it was necessary to design input circuitry which converts fast NIM signals to LVTTL signals. In electronics, comparators are used to compare two voltage levels and provide an output indicating which is higher. Using a comparator connected to the fast NIM signal and an appropriate threshold, an output signal will be generated when the fast NIM signal crosses the threshold. The duration of the output signal is equal to the length of time which the NIM negative signal spends below the threshold. This approach was incorporated on the input stage to the TDC DAQ module.

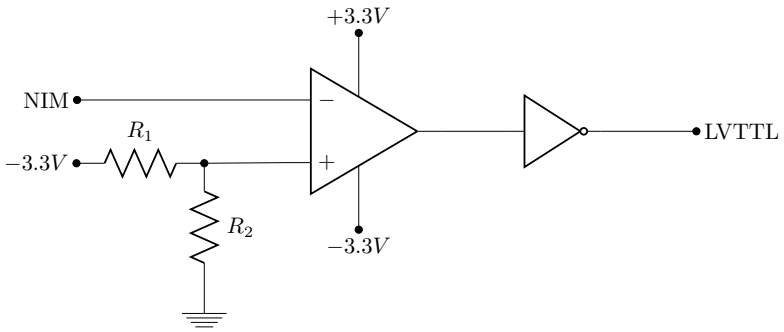

Figure 4.4: Basic design of a NIM-to-LVTTL level converter

As illustrated in Figure 4.4, a simple NIM-to-LVTTL converter can be constructed using a comparator, an inverter and a voltage divider. In such a design, the fast NIM

negative signal is connected to the inverting input of the comparator while a negative reference voltage is connected to the non-inverting input. Although it is possible to provide the reference voltage externally, the simplest way is to use a voltage divider connected to the negative supply of the comparator. Therefore, it is required that a comparator with a split power supply and an input range which extends to the negative rail be used. Most comparators which offer this feature will generally output a signal of the same polarity as the input signal and an inverter is required to produce a signal of opposite polarity.

When selecting comparators for the NIM-to-LVTTL converter, significant emphasis was placed on parameters describing the timing jitter and maximum toggling frequency. Timing jitter refers to the deviation from the ideal timing of an event and it fundamentally describes the timing error of a system. In order to preserve the excellent timing resolution of the TDC-GPX in the overall system, the timing jitter of the comparator output should be smaller than the width of a single time bin. In I-Mode, the TDC-GPX has a typical resolution of 81 ps. Therefore, it is desirable that the selected comparator have an output timing jitter better than 81 ps.

The maximum toggling frequency is a parameter which specifies how fast the output of the comparator can switch between states. In most comparators, this is defined by the highest frequency at which a 100 mV sinusoidal input results in an error free output toggling to greater than 4V when HIGH and to less than 1V when LOW on a 5V power supply. On the TDC DAQ module, the required maximum toggling frequency of the comparator is dictated by the pulse width of the fast NIM negative signal at the threshold voltage. A typical fast NIM negative pulse width, measured at half amplitude, is about 5 ns. Assuming the next pulse will not arrive

for another 5 ns, the situation is similar to the comparator toggling on a sinusoidal with a period of 10 ns. It is therefore required that the comparator successfully toggle at a frequency of at least 100 MHz.

Following an extensive catalogue search through the common integrated circuit (IC) manufacturers, the Linear Technology LT1715 comparator chip was selected for the NIM-to-LVTTL converter. The LT1715 has a maximum toggling frequency of 150 MHz and a timing jitter of 15 ps RMS. Although the LT1715 offers dual comparators in a single IC package, this feature was not used due to significant crosstalk between neighbouring channels exhibited at high switching frequencies. Therefore, the signal conversion on the TDC DAQ is accomplished using independent LT1715 ICs for each input channel. Additionally, the LT1715 offers independent input and output supplies in a single chip. The independent supplies are a convenient feature since they eliminate the inverter which was previously required to produce a positive signal. This allows a negative input signal to be compared to a negative threshold while the output signal is positive. Moreover, by removing the inverter from the design, an additional source of jitter was eliminated.

4.2 FPGA Firmware Architecture

Containing programmable logic, in the form of logic blocks, FPGAs are a special class of ICs which can be modified after manufacturing. With most processors, compilers convert the user code to a set of operations to be performed within the already available logic units. Conversely, firmware written for FPGAs control the high speed connections between sets of logic blocks (gates/flip flops). Therefore, the process of programming FPGAs results in true logic circuits implemented using the available logic blocks.

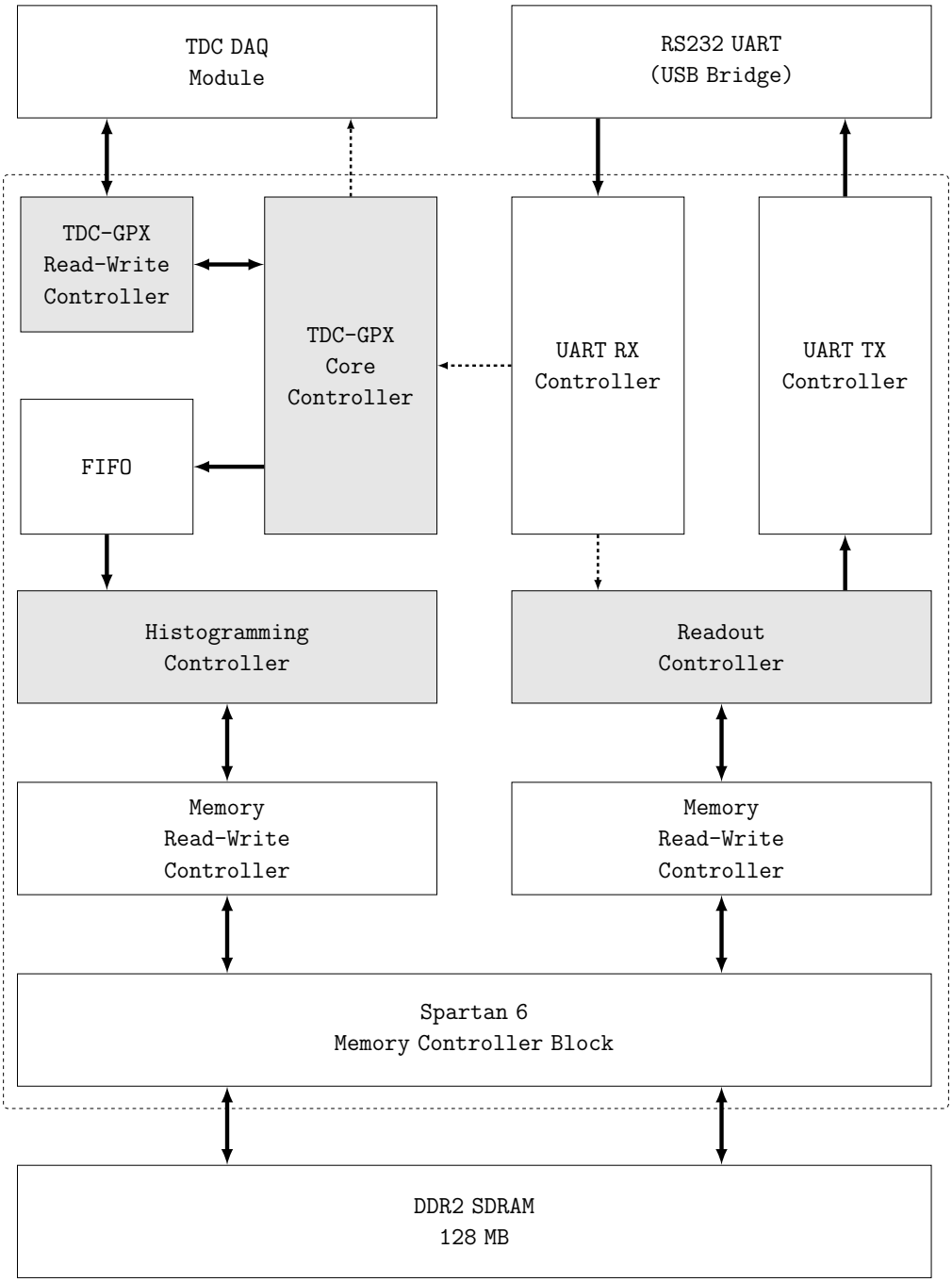

Figure 4.5: Diagram of the top level firmware architecture controlling the TDC DAQ module. Control modules are enclosed by the dashed rectangle. Data flow and control signals are represented by solid and dashed arrows, respectively.

Once the TDC DAQ module had been designed and assembled, the next step was to develop the firmware for the Spartan 6 FPGA on-board the Xilinx SP601 development board. The primary objective of the FPGA firmware is to implement the necessary logic for communicating with the TDC-GPX ASIC. Additionally, the FPGA is expected to perform the event position reconstruction and image generation algorithms in real-time. At the end of an acquisition window, time measurements should be retrieved from the TDC-GPX and the FPGA should compute the interaction position on an event by event basis. Once the event position is known, the second step is to increment the number of counts at the corresponding memory location. Finally, when requested by the user, the FPGA logic should send the image data to the PC for display. Although offline analysis of the time measurements during a single acquisition would be beneficial, the throughput rate of such a system is limited by the large amount of data which needs to be transferred and stored.

As illustrated in Figure 4.5, the FPGA firmware consists of eight controller modules, a `FIFO` and a `Memory Controller Block`. Of the eight controller modules, the four most important are the `TDC-GPX Read-Write Controller`, `TDC-GPX Core Controller`, `Histogramming Controller`, and the `Readout Controller`. The logic inside each of these modules will be discussed in the following subsections.

The `Memory Controller Block` generates the necessary logic and timing requirements for interfacing the FPGA with the DDR2 memory. The two `Memory Read-Write Controllers` provide a simple logic abstraction layer for the complicated DDR2 logic. Finally, the `UART RX Controller` and `UART TX Controller` implement a communication protocol between the FPGA and PC using the serial interface. Although important in the operation of the entire system, the logic inside the aforementioned

modules is relatively standard and does not merit a more through discussion.

4.2.1 TDC-GPX Controllers

The primary function of the FPGA firmware is to establish communication with the TDC DAQ module and retrieve the measurement data. As illustrated in Figure 4.5, the two modules directly involved in communicating with the TDC-GPX are the `TDC-GPX Read-Write Controller` and `TDC-GPX Core Controller`. While the `TDC-GPX Core Controller` is responsible for initializing and monitoring the data acquisition process, the `TDC-GPX Read-Write Controller` implements the necessary read/write functionality required for modifying registers on the TDC-GPX. Intercommunication between the two controller modules allows effective transfer of measurement data across the entire TDC DAQ event reconstruction system.

Data transfer between the TDC-GPX and FPGA is handled by the `TDC-GPX Read-Write Controller`. Since the TDC-GPX employs a proprietary communication protocol, using a 28-bit data bus and a 4-bit address port, an abstraction layer is required to efficiently integrate this logic with the rest of the system. The abstraction layer, employed by the `TDC-GPX Read-Write Controller`, masks all of the specific timing requirements which must be met and provides a simple interface for the rest of the modules. Additionally, abstraction allows read and write operations to occur at their maximum transfer rate irrespective of the downstream logic. The timing requirements and Verilog code employing the communication protocol are found in Appendix A.3.

With the TDC-GPX, time measurements can be made in either the single window or continuous measurement modes. In the single window mode, as illustrated in Figure 4.6, a signal on the TStart channel triggers the start of an internal timer

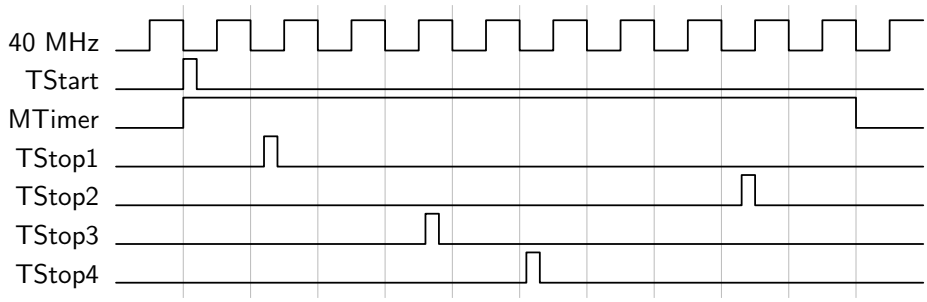

Figure 4.6: Example acquisition with the TDC DAQ configured for a window length of 250 ns.

known as the MTimer. The period of the MTimer, derived from the 40 MHz clock on-board the TDC DAQ, defines the region on time (window) in which measurements can be made on the four stop channels, TStop1 through TStop4. Outside of this window, stop signals are ignored and no measurements are made. At the end of the measurement window, an external flag is raised indicating that data is available on the TDC-GPX. Once the data has been read, the TDC-GPX must be partially reset in order to allow subsequent measurements. During the reset, which last for approximately 60 ns, start and stop pulses cannot be processed and the system is effectively dead. On the TDC DAQ event reconstruction system, the single window mode has a length of 250 ns and allows measurements to be made at a continuous rate of just below 2 MHz.

The `TDC-GPX Core Controller` is the module which configures the TDC-GPX and initiates the data acquisition process. Logic inside this module is primarily controlled by the FSM illustrated in Figure 4.7. On power up, the `TDC-GPX Core Controller` enters the `IDLE` state. While in the `IDLE` state, the FPGA must configure the registers on the TDC-GPX before an acquisition can be started. When

a configure command is received from the `UART RX Controller`, the FSM transition to the `Config` state. In the `Config` state, and with the help of the `TDC-GPX Read-Write Controller`, the FSM configures registers which control the operating mode, timing resolution, edge sensitivity, and window length of the TDC-GPX. When the TDC-GPX has been successfully configured, the FSM returns to the `IDLE` state.

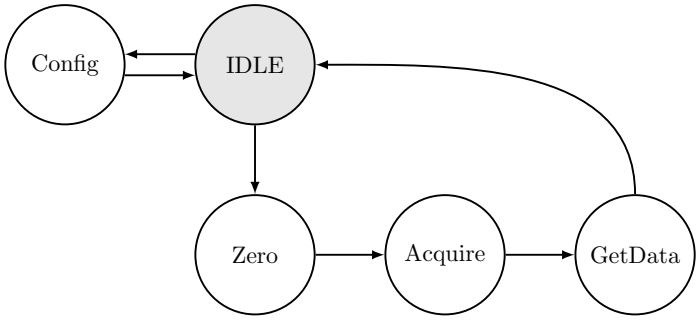

Figure 4.7: A simplified schematic of the FSM controlling the logic inside the TDC-GPX Core Controller. The initial state, `IDLE`, is shown in the shaded circle.

When a start command is received from the `UART RX Controller`, the FSM transitions to the `Zero` state. The purpose of `Zero` state is to provide a blank time marker, labelled the `START` timestamp, before the beginning of each acquisition cycle. The `START` timestamp is used in other modules to identify measurements belonging to the same acquisition cycle. Once a `START` timestamp is generated, the FSM transitions to the `Acquire` state. In the `Acquire` state, the FSM waits for the end of the acquisition window and queries the TDC-GPX for available data. If data is present, the FSM transitions to the `GetData` state where the timestamps are transferred to the `FIFO`. When data transfer is complete, the TDC-GPX is partially reset and the FSM transitions back to `IDLE` where it is ready for another acquisition cycle.

The `TDC-GPX Core Controller` is connected to the rest of the TDC DAQ modules through a `FIFO`. One advantage of having a `FIFO` for temporarily storing measurement

data, is that the event acquisition logic and the histogramming logic can occur in parallel. While the `TDC-GPX Core Controller` is acquiring events, the `Histogramming Controller` can process time measurements from the previous acquisition cycle. As long as the acquisition rate does not exceed that which the histogramming logic can handle, the operations are essentially independent. Parallel processing allows each controller to operate at its maximum frequency resulting in optimum data throughput. The Verilog code which implements the `TDC-GPX Core Controller` logic has been included in Appendix A.4.

4.2.2 Histogramming Controller

The `Histogramming Controller` is primarily responsible for reconstructing the interaction position from time measurements made during a single acquisition window. Logic inside this controller interprets the incoming timestamps, generates a memory address corresponding to the difference between timestamps originating from a common axis, and increments the value at the generated memory address. As illustrated in Figure 4.8, all of the logic inside this module is controlled by a FSM. Initially in the `IDLE` state, the FSM continuously checks the `FIFO` empty flag for valid timestamps. Once the `FIFO` has at least one timestamp, the FSM issues a read command to the `FIFO` and transitions to the `GetTime` state. If no timestamps are available for processing, the FSM remains in the `IDLE` state.

As shown in Figure 4.9, output timestamps from the TDC-GPX appear on the `FIFO` in the same chronological order that they were processed. In order to subtract timestamps originating from a common axis, logic in the `GetTime` state groups them into registers corresponding to the respective stop channel on which the measurements were made. If a `START` timestamp is received, the logic interprets the number of

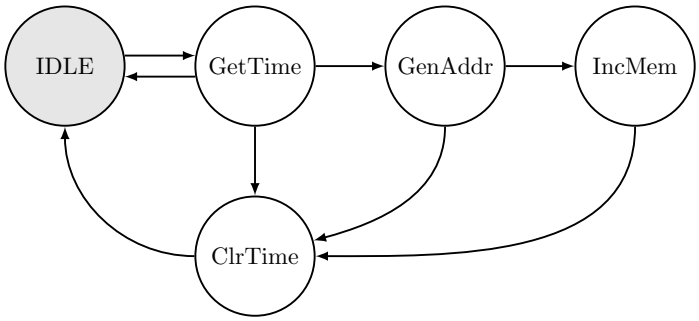

Figure 4.8: A simplified schematic of the FSM controlling the logic inside the Histogramming Controller. The initial state, `IDLE`, is shown in the shaded circle.

timestamps since the previous `START` and determines valid events. If greater than four timestamps were received, the situation represent multiple events in the same acquisition cycle and their position cannot be determined based on timing alone. Alternatively, less than four hits represents an insufficient amount of data. Therefore, a valid event consists of exactly four unique timestamps. For all valid events, the FSM computes the difference between timestamps originating from a common axis and transitions to the `GenAddr` state. Timestamps of non-valid events are discarded via a transition to the `ClrTime` state.

In the `GenAddr` state, the computed time differences are compared to a maximum allowable range. If the time difference for each axis falls within the allowable range, a memory address is generated. The memory address is generated from the arbitrary X and Y coordinates determined by the difference between TStop1–TStop2 and TStop3–TStop4 pairs, respectively. The successful generation of a memory address triggers a transition to the `IncMem` state, otherwise the event is discarded via a transition to the `ClrTime` state. Although adjustable for various delay line lengths, the default maximum allowable range corresponds to delay lines shorter than $\sim$166 ns.

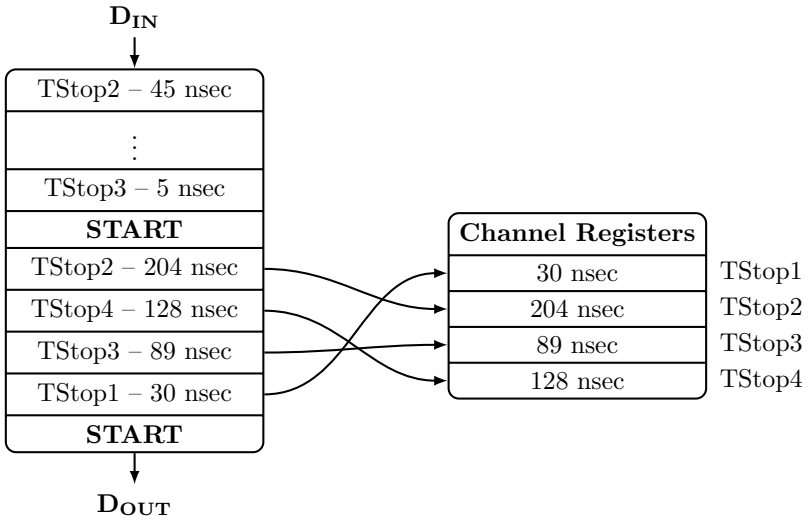

Figure 4.9: Visualization of the sorting logic employed in the Histogramming Controller using the acquisition example in Figure 4.6. Measurements made by the TDC-GPX appear on the FIFO in the same chronological order in which they were processed.

Dividing this range into 1024 pixels per axis, requires the TDC to have a time resolution of ∼162 ps. The typical resolution of the TDC-GPX is 81 ps, with minimum and maximum resolutions of 64 ps and 113 ps, respectively. Configuring the TDC-GPX to the typical 81 ps resolution and dropping the least significant bit (LSB), of each timestamp, accomplishes the required resolution. In addition to providing the necessary resolution, dropping the LSB of each timestamp significantly improves the DNL caused by the periodicity of the LSB.

Finally, in the `IncMem` state, a read command is issued to the `Memory Read-Write Controller` using the generated memory address. The data returned is incremented by one and written back into the same memory address. Following a successful write operation, the FSM transitions to the `ClrTime` state and the entire process starts over.

The raw image data, generated by the TDC DAQ, is stored on-board the 128 MB

of DDR2 memory provided by the SP601. Using this data, image files are generated which are 1024 x 1024 square pixels with a pixel depth of 32-bits and a final size of 4 MB. Due to the periodicity in the LSB of each timestamp, the timing resolution of each pixel is twice that of the LSB. On the TDC DAQ, the timing resolution of each pixel of the raw image files corresponds to 162 ps.

4.2.3 Readout Controller

As illustrated in Figure 4.5, the `Readout Controller` is located between the serial `UART Controllers` and the `Memory Read-Write Controller`. Although tasked with multiple functions, the `Readout Controller` is primarily responsible for interpreting read requests from the `UART RX Controller` and serializing the raw image pixels, stored on-board the DDR2 memory, to be sent to the PC via the the `UART TX Controller`. Additionally, the `Readout Controller` is responsible for clearing the DDR2 memory and performing the image scaling algorithm required for real-time display of the image. The logic inside the `Readout Controller` is controlled by the FSM illustrated in Figure 4.10.

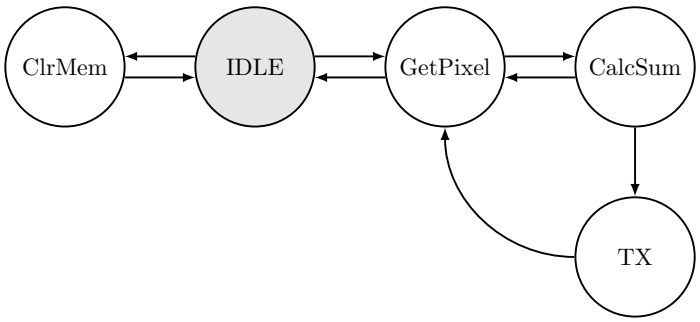

Figure 4.10: A simplified schematic of the FSM controlling the logic inside the Readout Controller. The initial state, `IDLE`, is shown in the shaded circle.

Initially in the `IDLE` state, the FSM waits for a clear memory request or a read data request from the `UART RX Controller`. If a clear memory request is received, the

FSM transitions to the `ClrMem` state. Due to the volatile nature of DDR memory, the information stored in memory cannot be maintained while the power is off. Moreover, once the memory is powered on, the initial values are random and must be zeroed. Following a power up, or when requested by the user, the `ClrMem` state is responsible for zeroing the 128 MB DDR2 memory on-board the SP601 evaluation kit. Once memory is cleared, the FSM transitions back to the `IDLE` state.

Due to the low data rate of serial communication and the relatively large size of the images stored in memory, transfer times for full sized images can reach 10 minutes. These transfer times are unacceptable for viewing images in real-time. For this reason, it was decided that an image scaling algorithm should be implemented in hardware to allow low resolution images to be displayed in near real-time. When requested, the image scaling algorithm divides the number of pixels in each axis of the raw image by powers of two. Image scaling is accomplished by accumulating the values of all the high resolution pixels corresponding to one pixel in the scaled image. As each pixel of the scaled image is calculated, it is serially sent to the PC to be reconstructed. For each factor of two scaling, the effective transfer times are reduced by a factor of four. For a low resolution, 32 x 32 square pixel image, transfer times are reduced to under one second. Since the scaling algorithm is passive, the image data stored in memory remains unchanged and high resolution images can be downloaded once the acquisition is complete.

As shown in Figure 4.10, when a read image request is initiated, the FSM transitions from the `IDLE` state to the `GetPixel` state. In the `GetPixel` state, a read pixel request is placed to the `Memory Read-Write Controller`. Once the `Memory Read-Write Controller` returns the requested pixel value, the FSM transitions to

the `CalcSum` state. In the `CalcSum` state, the sum of all high resolution pixels corresponding to one low resolution pixel is calculated. Once complete, the FSM transitions to the `TX` state where the value of the low resolution pixel is sent to the `UART TX Controller` to be transmitted to the PC. Once all of the scaled image pixels are transmitted, the FSM transitions back to the `IDLE` state.

4.3 Graphical User Interface

To allow for simple control and communication with the TDC DAQ, a graphical user interface (GUI) was developed using the Matlab environment. Seeing that the image generating logic has been implemented entirely in hardware, the primary role of the GUI is to retrieve the image data from the DDR2 memory on the SP601 and store it in the local memory of the PC. Additionally, the GUI provides a simple means of configuring and controlling the TDC-GPX ASIC.

Since the Xilinx SP601 is an entry-level FPGA development kit, it offers relatively few options for communication with a PC. The fastest method, and consequently the hardest to implement, is using the gigabit ethernet. Due to its high throughput speeds, the gigabit ethernet could potentially allow the TDC DAQ to have real time display for all image sizes. However, in order to use the gigabit ethernet several communication layers should be implemented in FPGA. The time and effort required to implement the gigabit ethernet logic is significant and for the purposes of this project an unnecessary waste. As an alternative, the SP601 also includes a serial communication via USB connection. Although orders of magnitude slower, the serial communication is significantly easier to implement and debug. Therefore, this version of the TDC DAQ has been developed using the serial interface on-board the SP601.

As illustrated in Figure 4.5, the PC is connected to the SP601 through the `RS232`

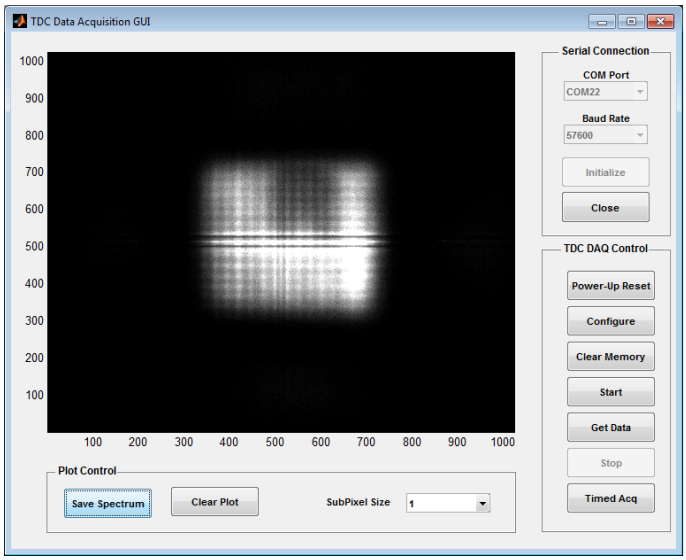

Figure 4.11: A picture of the Matlab based graphical user interface (GUI) used in controlling the TDC DAQ with an example image acquisition.

`UART` using a baud rate of 57,600 bits per second. The `RS232 UART` sends ASCII commands, received from the PC, to the `UART RX Controller` which interprets them and converts them to the appropriate control signals for the various modules on the TDC DAQ. Image data is transferred from the TDC DAQ to the PC via the `UART TX Controller`. Aside from generating ASCII control signals, the only logic performed by the GUI is to reconstruct the image from the data received over the serial port.

Illustrated in Figure 4.11, the TDC DAQ GUI consists of three control panels and an image container. The Serial Connection panel, on the top right of the GUI, is used for establishing a serial communication with the SP601. The TDC DAQ Control panel, is used for generating the ASCII commands which reset/configure the TDC-GPX, start/stop the acquisition, and clear/retrieve data from memory. Lastly, the Plot Control panel is used in setting the image scaling factor and saving the acquired image to PC memory. When all of the data has be retrieved from the TDC DAQ

memory, the reconstructed image is displayed in the image container.

4.4 Maximum continuous throughput rate

The maximum continuous throughput rate is defined by the maximum input frequency, of start and stop signals, for which the TDC DAQ event reconstruction system can still resolve the true interaction position. The continuous throughput rate is a parameter which describes the average count rate which the system can successfully handle with a reasonable dead time. It should be obvious to the reader, that the maximum count rate which the TDC DAQ can handle is in no way related to the maximum count rate of the THGEM imaging detector.

On the TDC DAQ event reconstruction system, the system throughput was measured using a variable frequency pulse generator connected to two CFDs. The trigger signal from the pulse generator was first inverted and then connected to the TStart input of the TDC DAQ module. The output of the pulser generator was split and connected to two CFDs. The output of each CFD was connected to the four stop inputs, TStop1–TStop4. The output frequency of the PB-5 pulse generator was measured using an oscilloscope (Agilent MSOX2024A).

Using the timed acquisition function of the GUI, allowed for acquiring events within a known period of time. The measured frequency was calculated from the sum of events over the entire image divided by the measurement period. As illustrated in Figure 4.12, the system throughput was measured over a wide range of input frequencies. The maximum continuous throughput rate of the TDC DAQ event reconstruction system is 1.8 MHz. Beyond 1.8 MHz, the system cannot resolve the true interaction position.

On the TDC DAQ, the maximum continuous throughput rate is primarily limited

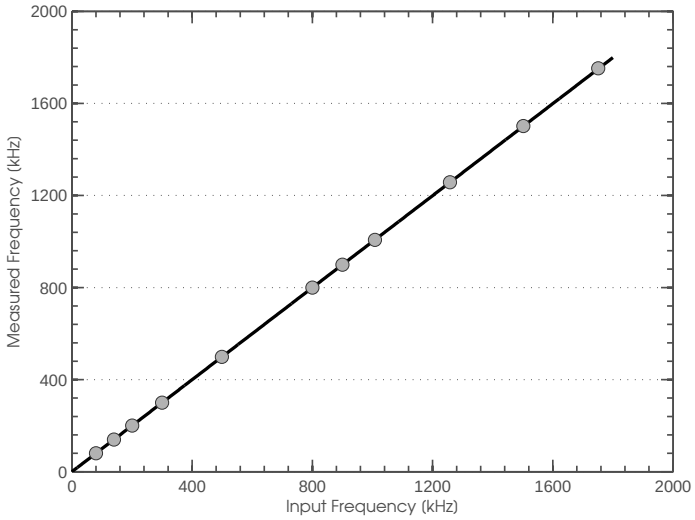

Figure 4.12: Plot of the measured continuous throughput rate of the TDC DAQ event reconstruction system.

by the length of acquisition window, chip reset time, and the time required to read the timestamps from the TDC-GPX. As previously mentioned the window length and reset are 250 ns and 60 ns, respectively. In Appendix A.3, it is demonstrated that a continuous read of 4 time measurements adds an additional dead time of 200 ns. Therefore, the period of a single acquisition cycle lasts approximately 510 ns and results in a maximum throughput rate of 1.96 MHz for periodic signals. It should be noted that the theoretical calculations do not account for the few clock cycles necessary to verify that the read operations are complete. Considering these additional clock cycles should bring the theoretical throughput rate to the measured value.

4.5 Integral non-linearity

In histogramming applications, such as the TDC DAQ event reconstruction system, it is important to have a measure of the system linearity. Non-linearities in

the TDC of timing based imaging detectors have the potential to introduce various distortion effects, such as barrel or pincushion distortion, in the final image. If a model of the system non-linearities exists, image distortions can be corrected in post processing.

The most direct method for measuring the non-linearity of a system is to measure the INL. In TDC based systems, this can be measured by plotting the peak channel corresponding to pulses with a known relative time difference. The maximum deviation of the measured data from the linear fit is a measure of the INL and is quoted as a percentage of the full system measurement range. In well-designed systems, non-linearities are often lower than 0.1%.

The INL of the TDC DAQ event reconstruction system was measured by varying the time difference between channels corresponding to a common axis in 8 ns intervals covering a time range of 120 ns. The output signal from a pulse generator was connected between independent nanosecond delay units. This arrangement allows each channel to be delayed a maximum of 62 ns relative to each other. The output signals from the nanosecond delay units were then connected to a pair of constant fraction discriminators (CFD) for timing pickup. Keeping the time difference in one axis constant while varying the other, allowed for measuring the INL in both X and Y axis.

The results of the INL measurement, on the TDC DAQ event reconstruction system, are illustrated in Figure 4.13. The bright pixels in the reconstructed images Figure 4.13 (a) and (b), represent the position of signals spaced in 8 ns intervals. Using the raw image file, a plot of true versus measured time interval is obtained for each coordinate. The INL is defined by the maximum deviation of the measured

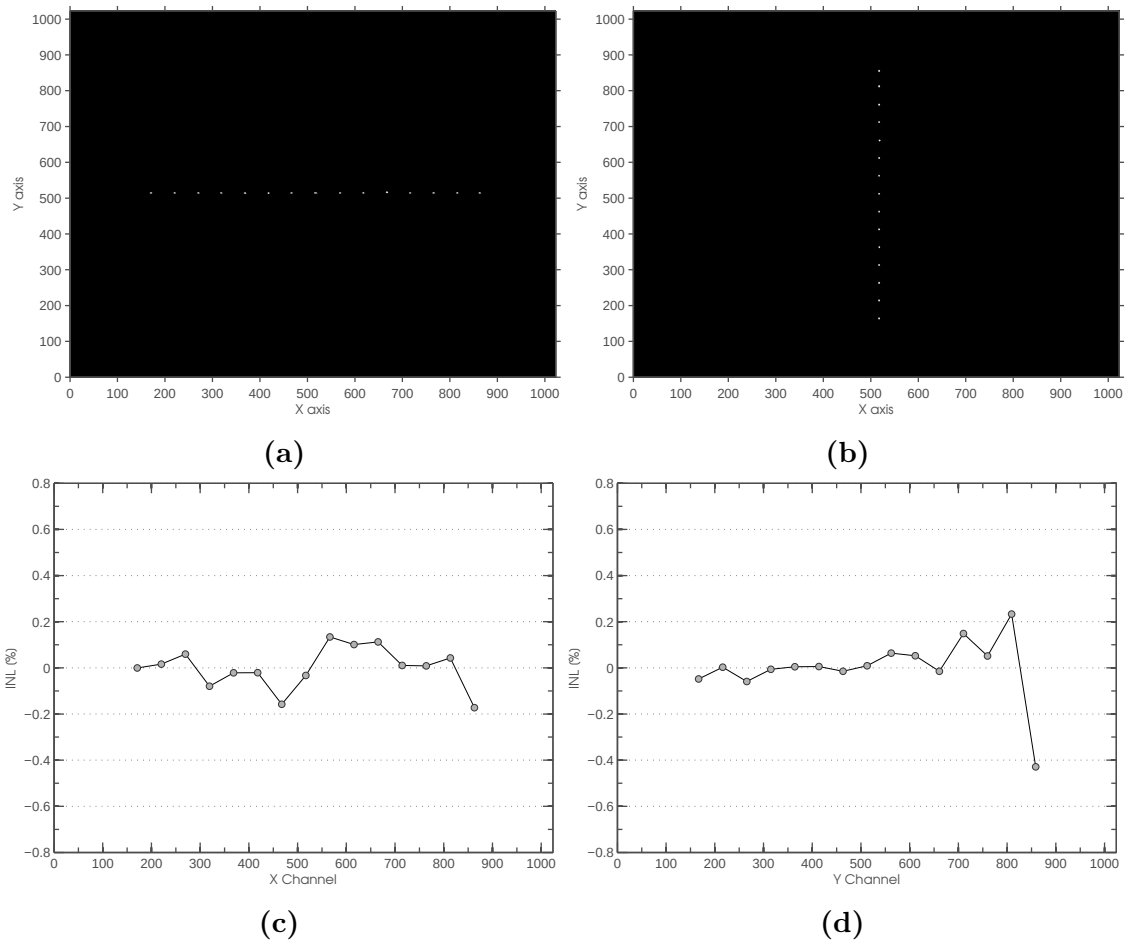

Figure 4.13: Illustrated in (a) and (b) are the raw image files used for calculating the INL along the X (c) and Y (d) axis, respectively. The INL is calculated from the difference in the fitted peak location from the true location, divided by the total range of the TDC DAQ.

peak location from the linear fit, divided by the total TDC DAQ range. Illustrated in Figure 4.13 (c) and (d), the INL measurements along the X and Y axis are 0.17% and 0.43%, respectively. The results of these measurements illustrate that the TDC-GPX is very linear within the measurement rage used by the TDC DAQ event reconstruction system.

4.6 Differential non-linearity

A more sensitive method for measuring the non-linearity of a system is to measure the DNL. On TDC based systems, this can be accomplished by employing pulses with a uniform time distribution over the entire measurement range. Enough time must be allowed such that the statistical fluctuation within each bin is smaller than the desired measurement accuracy. In linear systems, a plot of the number of counts per channel versus channel number should produce a uniform or flat distribution. A flat distribution is an indication that each bin sampled the time space with equal probability. Deviations from linearity of a few percent (<5%) are typical of good TDC systems.

The DNL describes how well adjacent analog values are converted to adjacent digital values and is a measure of the uncertainty in the LSB. On the TDC DAQ event reconstruction system, the DNL was measured using three pulse generators running at slightly different frequencies. One pulse generator was connected to the TStart input and the other two were connected to the four stop signals, TStop1 – TStop4. This method relies on the randomness, created by the out of phase pulse generators, to uniformly sample the entire measurement range of the TDC DAQ event reconstruction system.

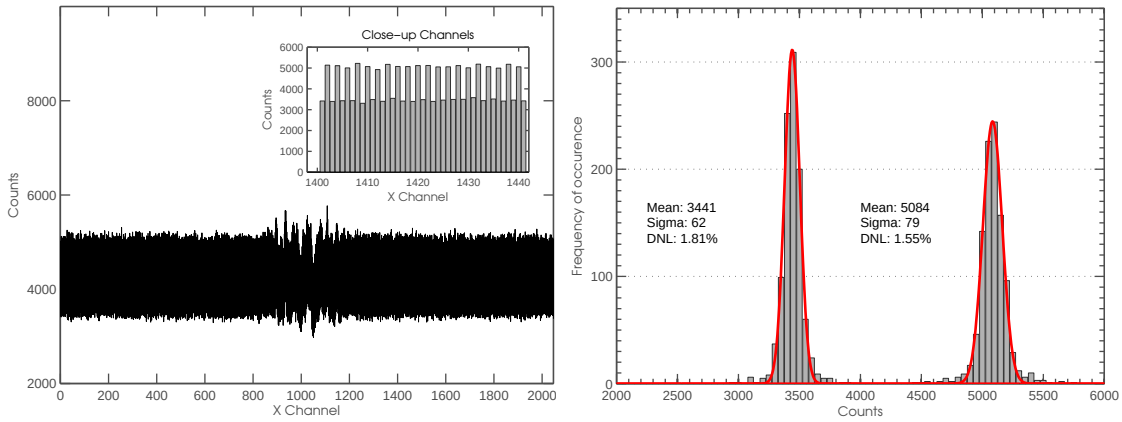

(a) **(b)**

Figure 4.14: The distribution of counts along the X axis (a) with the TDC-GPX configured to a standard timing resolution of 81 ps. A close-up of the spectrum reveals the systematic periodicity caused by the LSB. The DNL, illustrated in (a), shows two groups of counts as a result of the LSB periodicity.

Using the aforementioned method, and with the TDC-GPX configured at the typical 81 ps resolution, the DNL of the TDC DAQ has been measured. In these results, the DNL is calculated from the standard deviation (σ) of the Gaussian fit describing the distribution of counts along each axis. The results of these measurements indicate that the TDC-GPX displays a moderate DNL. Although not promising, the results are not entirely negative. Illustrated in Figure 4.14 (b), the DNL of the TDC-GPX shows two distinct groups of counts, not one as expected. A close-up view of the number of count versus channel number spectrum, illustrated in Figure 4.14 (a), reveals the source of the problem. As a result of the method by which time is measured on the TDC-GPX, a narrow time bin is followed by a broad time bin with a periodicity of two. The difference in width between adjacent bins results in two distinct groups of counts. However, since adjacent bins are represented by the LSB of the timestamps, the DNL of the system can be substantially improved by omitting the LSB.

As suggested, the LSB of each timestamp from the TDC-GPX is omitted in the

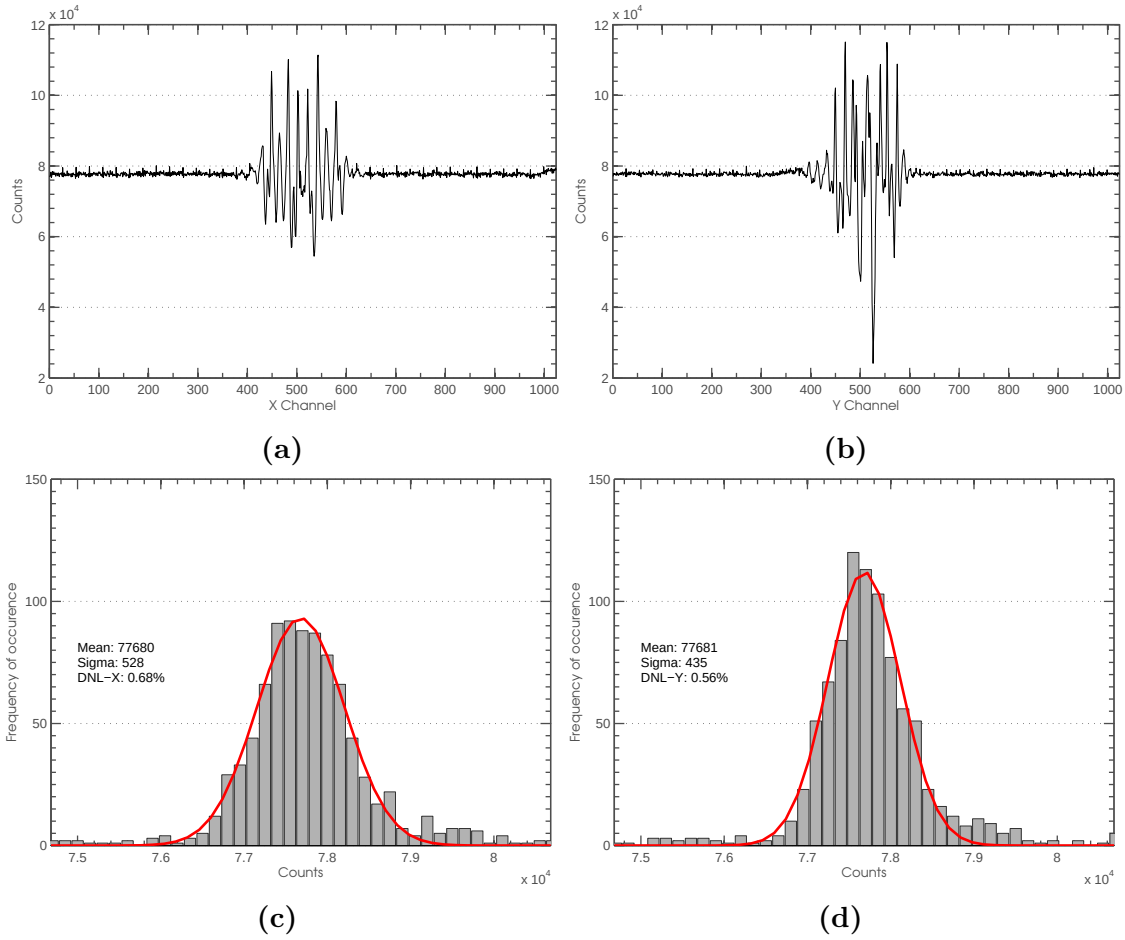

Figure 4.15: Illustrated in (a) and (b) is the distribution of counts along the X and Y axis, respectively. The DNL in the X (c) and Y (d) axis is calculated from the FWHM of the normal distribution describing the variability of counts in each channel of the spectrum.

`GetTime` state of the `Histogramming Controller`. The result of this modification improves the DNL of the TDC DAQ event reconstruction system by effectively averaging the bin width. Illustrated in Figure 4.15 (c) and (d), the DNL measurement along the X and Y axis are 0.68% and 0.56%, respectively. By omitting the LSB, the periodicity of widths in adjacent bins was entirely removed with only a larger periodicity remaining. As illustrated in Figure 4.15 (a) and (b), the larger periodicity does not significantly impact the DNL of the system.

Chapter 5

Imaging Results

In this thesis, a prototype THGEM imaging detector has been developed as a proof-of-concept for future imaging detectors. To demonstrate the imaging capabilities of the detector, a set of studies were performed using two radiation sources. First, collimated alpha particles, generated in the decay of a ^{244}Cm source, were used to demonstrate the one- and two-dimensional readouts described in Chapter 3. Since the range of alpha particles is small, the ^{244}Cm source was installed inside of the gas containment chamber and directly above the Mylar cathode. An imaging object was created by collimating the alpha particles through a 3 mm hole at the bottom of the source holder – see Figure 5.1. The hole dimensions were chosen as a compromise between collimation and count rate, which was approximately 100 cps.

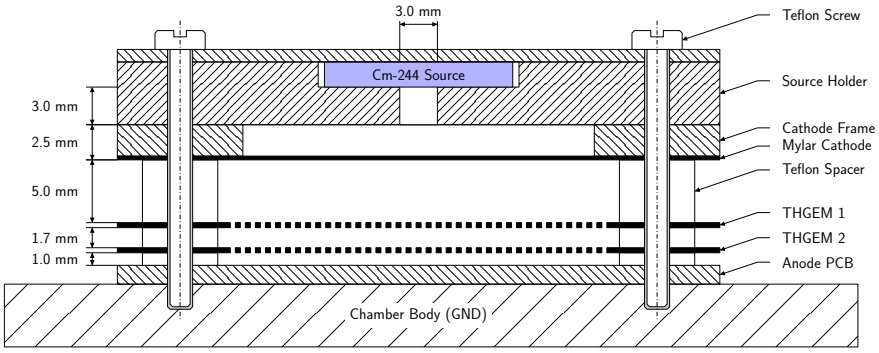

Figure 5.1: A cross-sectional view of the THGEM detector with the ^{244}Cm source assembled above the Mylar cathode. Horizontal dimensions not to scale.

Following the alpha particle imaging, the internal ^{244}Cm source was removed and the detector was configured for conventional X-ray transmission radiography. During these investigations, a range of imaging objects were placed in front of the THGEM detector and exposed to an X-ray beam. Due to the low interaction probability of X-rays with the detection gas, it was necessary to acquire images over a few hours to gather sufficient statistics. The X-rays used in these studies were generated from a high power X-ray tube (Varian NDI-160-21) connected to a 1800 W power supply (Gulmay CF160-2). With this setup, it was possible to generate X-rays up to 160 kVp and 25 mA of current. However, for the images described in this chapter, the accelerating potential was set to 40 kVp and the current to 20 mA. For these measurements, the detector was located 1.5 m from the X-ray tube, with a field size that was 8 cm in diameter and which resulted in a total count rate of 5000 cps.

In this chapter, I will assess the imaging performance of the prototype THGEM imaging detector. A limited number of filtering algorithms will be applied to improve the image quality and the spatial resolution will be estimated using a fitting technique. However, the objective of this chapter is to determine the factors which limit the spatial resolution and to suggest a series of steps which can be taken to improve the current value.

5.1 Alpha Particle Imaging

5.1.1 One-dimensional readout

As described in Chapter 3, a one-dimensional delay line anode was designed to demonstrate the feasibility of using the delay line method for extracting positional information from detected events. To use the one-dimensional readout, the position

reconstruction algorithm was modified such that only one axis was included in the calculations. In this configuration, the output from the TDC DAQ is a spectrum of time difference versus number of counts.

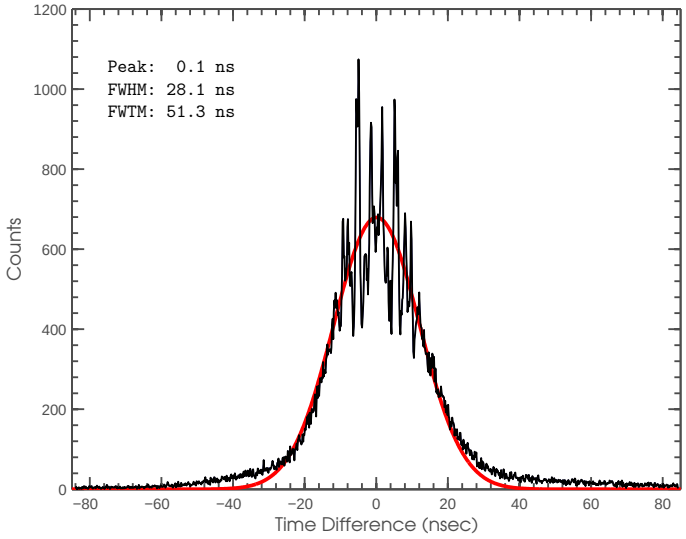

Figure 5.2: Collimated alpha particle imaging using the one-dimensional delay line readout anode.

As illustrated by the spectrum in Figure 5.2, it is evident that the imaging system can indeed locate the interaction position, of the collimated alpha particles, using output pulses from the delay line readout. From the fitting, it can be seen that the peak is located in the center of the spectrum as should be expected from the physical placement of the ^{244}Cm source. The full width at half maximum (FWHM) and full width at tenth maximum (FWTM) are 28.1 ns and 51.3 ns, respectively. As described in Figure 3.14, the one-dimensional readout is 29.5 $\pm$ 0.5 mm wide and the time delay from end-to-end of the delay line is 75 $\pm$ 2 ns. From these values, a coefficient of conversion, equal to 0.39 $\pm$ 0.01 mm/ns, was calculated. The FWHM and FWTM, expressed in units of distance, are 10.9 $\pm$ 0.3 mm and 20.0 $\pm$ 0.5 mm, respectively. While these values are significantly larger than the diameter of the collimation hole,

a simple geometrical calculation predicts the spot size to be approximately 18 mm at the top THGEM. Considering additional effects, such a diffusion and electron cloud size, it becomes evident that the measured width of the one-dimensional alpha imaging is certainly within reason. The successful demonstration of this initial *imaging* prompted the development of the two-dimensional readout.

5.1.2 Two-dimensional readout

Once the two-dimensional delay line readout had been constructed, a true image of the ^{244}Cm source could be acquired. As shown in Figure 5.3 (a) and Figure 5.3 (b), the bright spot near the center of the image represents the interaction position of alpha particles within the THGEM imaging detector. To compare the performance of the two readouts, the two-dimensional image was projected along the X and Y directions as shown in Figure 5.3 (c) and Figure 5.3 (d), respectively. Similarly, the peaks have been fitted, a conversion coefficient has been calculated and the peak dimensions have been expressed in millimeters. As expected, the width of the two-dimensional alpha imaging object matches the predicted value and is also consistent with measurements made using the one-dimensional readout.

As can be seen, particularly in the two-dimensional image, there are some artifacts which run the length of the image in both the X and Y direction. The cause of these artifacts is due to crosstalk between adjacent channels of the TDC DAQ position reconstruction system. This effect has been discussed in Chapter 4 and will be described in detail in the section to follow. In addition to crosstalk between adjacent timing channels, signal reflections on the two-dimensional delay line readout also introduce imaging artifacts. These artifacts appear as bright spots near the edges of the imaging area and their position does not correspond to one that can be inferred from

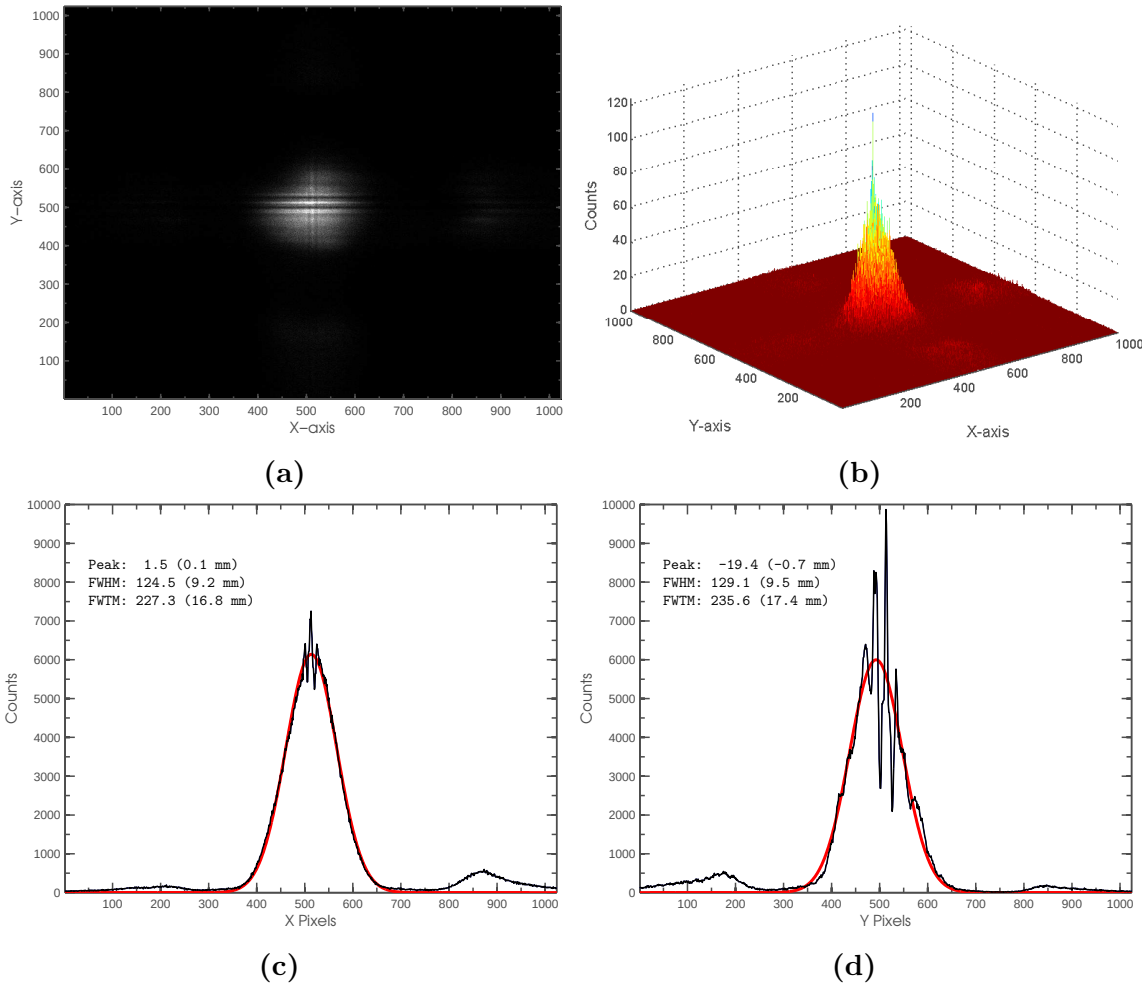

Figure 5.3: Raw image (a) and a three-dimensional surface plot (b) of the collimated alpha source. Projections along the X and Y axes are shown in (c) and (d), respectively.

the delay line. The distance of these spots, measured from the center of the image, is exactly twice the delay line length which suggests that they could be caused by signal reflections. Considering the impedance mismatch between the delay line and the preamplifiers, it is certainly not a surprise that there are signal reflections. Future delay line should be carefully designed to match the impedance of the preamplifiers. Nevertheless, these simple investigations illustrate that the delay line concept works as expected.

5.2 X-Ray Imaging

5.2.1 Correcting for detector and field inhomogeneities

The crosstalk, between adjacent channels of the TDC DAQ, is primarily caused by the TDC-GPX ASIC. While not directly specified in the datasheet, adjacent channels of the TDC-GPX exhibit cross talk due to stray capacitances on the die. On the TDC-GPX, stop channels are organized into groups of two and are then distributed along the perimeter of the IC. Early designs of the TDC DAQ used this grouping of input channels to manage signals from the same axis. The cross talk perturbs the time measurements between simultaneous pulse pairs resulting in artifacts on the acquired image. As shown in Figure 5.3, these artifacts appear as horizontal and vertical lines near the center of the images.

Digital images, which contain detector induced artifacts and field inhomogeneities, can be improved using a technique known as flat-field correction (Seibert *et al.*, 1998; Davidson *et al.*, 2003). While there exists many algorithms for flat-field correction, their primary objective is to remove artifacts caused by variations in pixel sensitivity

or shadows induced by imaging field inhomogeneities. To perform flat-field correction, the sensor is exposed to a uniform light field and an image is acquired. The image, known as the flat-field calibration image or flat-field image for short, is used to calculate a matrix of coefficients. Images can then be *flat-fielded* by multiplying the acquired image and flat-field coefficient matrices. A sensor which has been flat-fielded will produce a uniform output when illuminated by a uniform source.

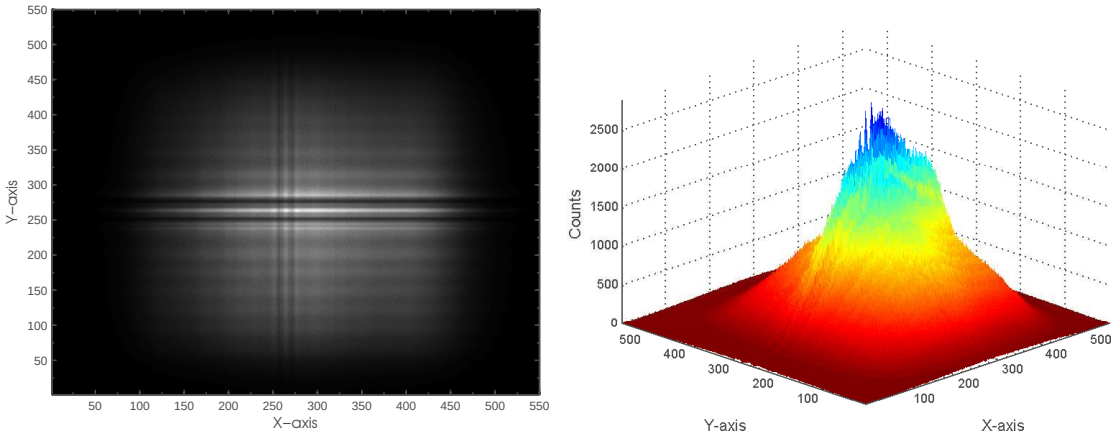

(a) **(b)**

Figure 5.4: Flat-field calibration image (a) and three-dimensional surface plot (b) taken with the THGEM imaging detector exposed to 40 kVp X-rays.

To correct for crosstalk, gain variations and field inhomogeneities, the THGEM imaging detector was exposed to a bare X-ray beam and an image was acquired. The flat-field image, shown in Figure 5.4, was used to calculate the flat-field coefficients by dividing the individual pixel intensities by the mean intensity value. Images were then flat-fielded by dividing individual pixels by the corresponding flat-field coefficient. As illustrated in Figure 5.5, this technique is very effective at removing detector and field inhomogeneities while preserving, and sometimes enhancing, image details. Due to its success, flat-field correction was applied to all images described henceforth.

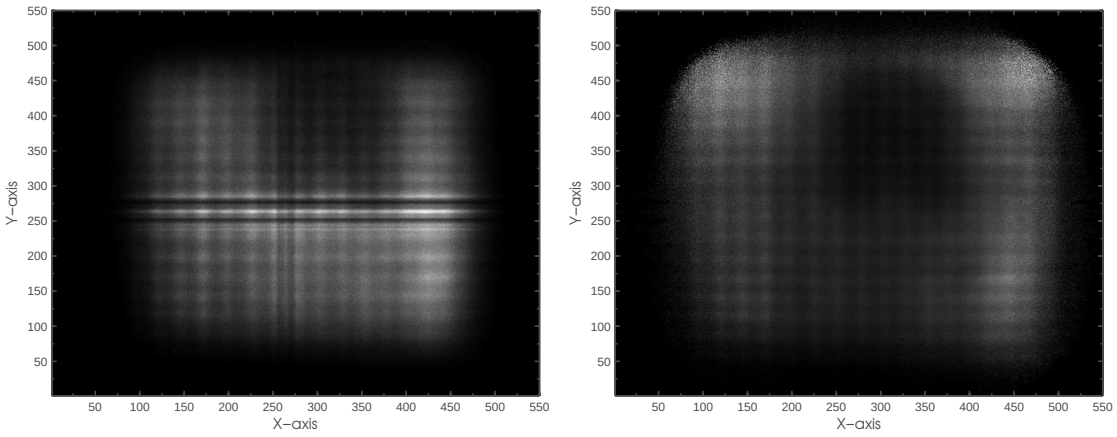

(a) **(b)**

Figure 5.5: Raw image (a) and flat-field corrected (b) images of a radiographic film identification marker (R) exposed to 40 kVp X-rays.

5.2.2 Large grid imaging

Following the initial success of the alpha imaging, the internal ^{244}Cm source was removed and the detector was reassembled with the objective of performing conventional X-ray transmission radiography. To do this, objects of interest were placed upon the front surface of the detector and exposed to an X-ray beam while an image was acquired. The first object imaged was a copper plate which had been perforated with a number of uniformly distributed holes. This so-called *large grid* object has a thickness of 1 mm, hole diameter of 1.95 $\pm$ 0.05 mm and a pitch of 6.35 $\pm$ 0.05 mm. The acquired flat-fielded image, and a three-dimensional surface plot, are presented in Figure 5.6 (a) and Figure 5.6 (b), respectively.

Unlike the alpha source, which was positioned directly over the collimation hole, the X-ray beam was more than a meter away from the imaging objects. To estimate the spatial resolution of the detector, it was assumed that the X-rays have an angle of incidence normal to the surface of the imaging object and any angular variation is

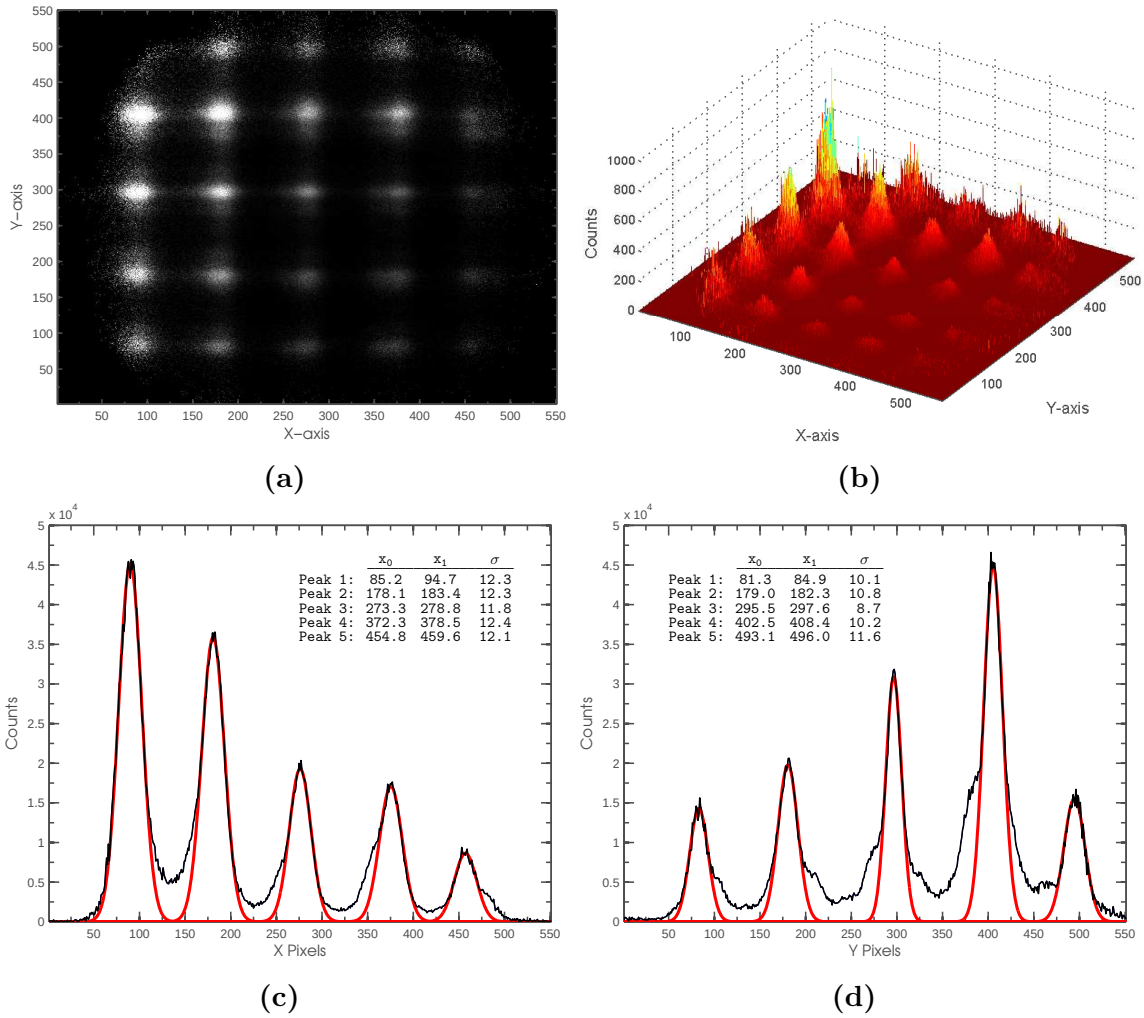

Figure 5.6: Flat-fielded image (a) and a three-dimensional surface plot (b) of the large grid object. Projections along the X and Y axes are shown in (c) and (d), respectively.

negligible. Therefore, any blurring of object details is due to the spatial resolution of the detector and not a geometry effect. In the acquired image, shown in Figure 5.6 (a), the holes are clearly illustrated by the uniformly distributed *bright spots*. Unlike the two-dimensional alpha images, the outlines of the holes are well defined in the X-ray images. The position, and width, of the holes can be determined by fitting the X and Y projections shown in Figure 5.6 (c) and Figure 5.6 (d), respectively.

To fit the peaks, some assumptions must be made regarding the imaging system and the interaction of the X-rays with the imaging object. Since the object is placed far from the X-ray source, and near the detector window, any blurring due to the penumbra effect is negligible. Therefore, the projection of a hole along the X or Y direction would be similar to a rectangular function which has a width equal to the hole diameter. However, all imaging systems have a finite point spread function (PSF) which describes the response of the imaging system to a point source. During an acquisition, the PSF is convolved with the true image resulting in the blurring of details which are smaller than the spatial resolution of the detector. As a first approximation, the PSF can be modeled as Gaussian with the standard deviation equal to the spatial resolution of the detector. The convolution of a Gaussian with a unit step function results in the well known error function. Since the rectangular function is the difference between two step functions, it follows that the convolution of a rectangular function with a Gaussian can be described by the difference in two error functions. Therefore, by fitting the holes in the X and Y projections, it is possible to estimate the spatial resolution of the system. In Equation 5.1, $\mathtt{A}$ is the amplitude, σ is the standard deviation of the Gaussian PSF, $\mathtt{x_0}$ is position of the left most edge

and x_1 is position of the right most edge.

$$f(x) = \frac{A}{2}\left[\mathrm{erf}\left(\frac{x - x_0}{\sigma\sqrt{2}}\right) - \mathrm{erf}\left(\frac{x - x_1}{\sigma\sqrt{2}}\right)\right] \tag{5.1}$$

To estimate the spatial resolution, the detector must first be calibrated using known distance measurements. Modern imaging systems undergo routine quality control and are calibrated using standard test objects. The images presented here were acquired towards the end of this thesis and there wasn't enough time to image a standard radiographic test object. Additionally, most test objects are larger than the active area of the THGEM imaging detector and difficult to image in the current configuration. Nevertheless, the detector can still be calibrated using the pitch of the holes. Since the holes were drilled on a milling machine, their position is relatively accurate and the effect of outliers diminishes if a large number of holes are included in the fitting. As illustrated in Figure 5.7, the average pixel dimension was calculated by plotting the hole center as a function of the relative distance. The slope of the fit represents the average pixel dimensions and has units of mm/pixel. Once the pixel dimensions are known, the spatial resolution along each axis can be estimated by multiplying the average standard deviation by the pixel size.

$$\sigma_x = 0.83 \pm 0.05\,\mathrm{mm} \tag{5.2}$$

$$\sigma_y = 0.61 \pm 0.08\,\mathrm{mm} \tag{5.3}$$

As shown in Equation 5.2 and Equation 5.3, the spatial resolution of the detector is estimated to be better along the Y axis. This effect is evident in the images, whereby the holes are slightly elongated along the X axis when compared to the Y direction. One of the possible causes for this effect is the capacitive coupling between electrodes

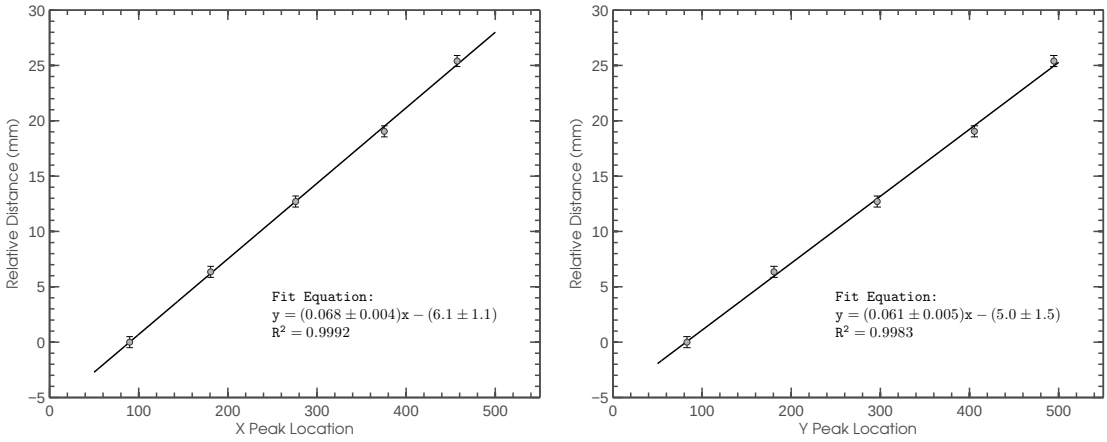

(a) **(b)**

Figure 5.7: Pixel dimensions along the X (a) and Y (b) axis measured from the large grid.

located on the inner layers of the two-dimensional readout board. Electrodes which are routed on the layer closest to the top layer can capacitively couple to the electrodes of the opposite axis. This effect can be mitigated by placing the ground layer directly below the collection pads.

5.2.3 Small grid imaging

The next object imaged was the so-called *small grid*. The results of this investigation are particularly interesting since the hole dimensions are very close to the estimated spatial resolution of the detector. This small grid object was also made from copper and has a thickness of 0.5 mm, hole diameter of 1.07 ± 0.05 mm and a pitch of 3.00 ± 0.05 mm. The acquired flat-fielded image, and a three-dimensional surface plot, are presented in Figure 5.8 (a) and Figure 5.8 (b), respectively.

As done in the previous sections, the acquired image was projected along the X and Y axes and the plots are shown Figure 5.8 (c) and Figure 5.8 (d), respectively. Peaks corresponding to the different holes were fitted using Equation 5.1 and the

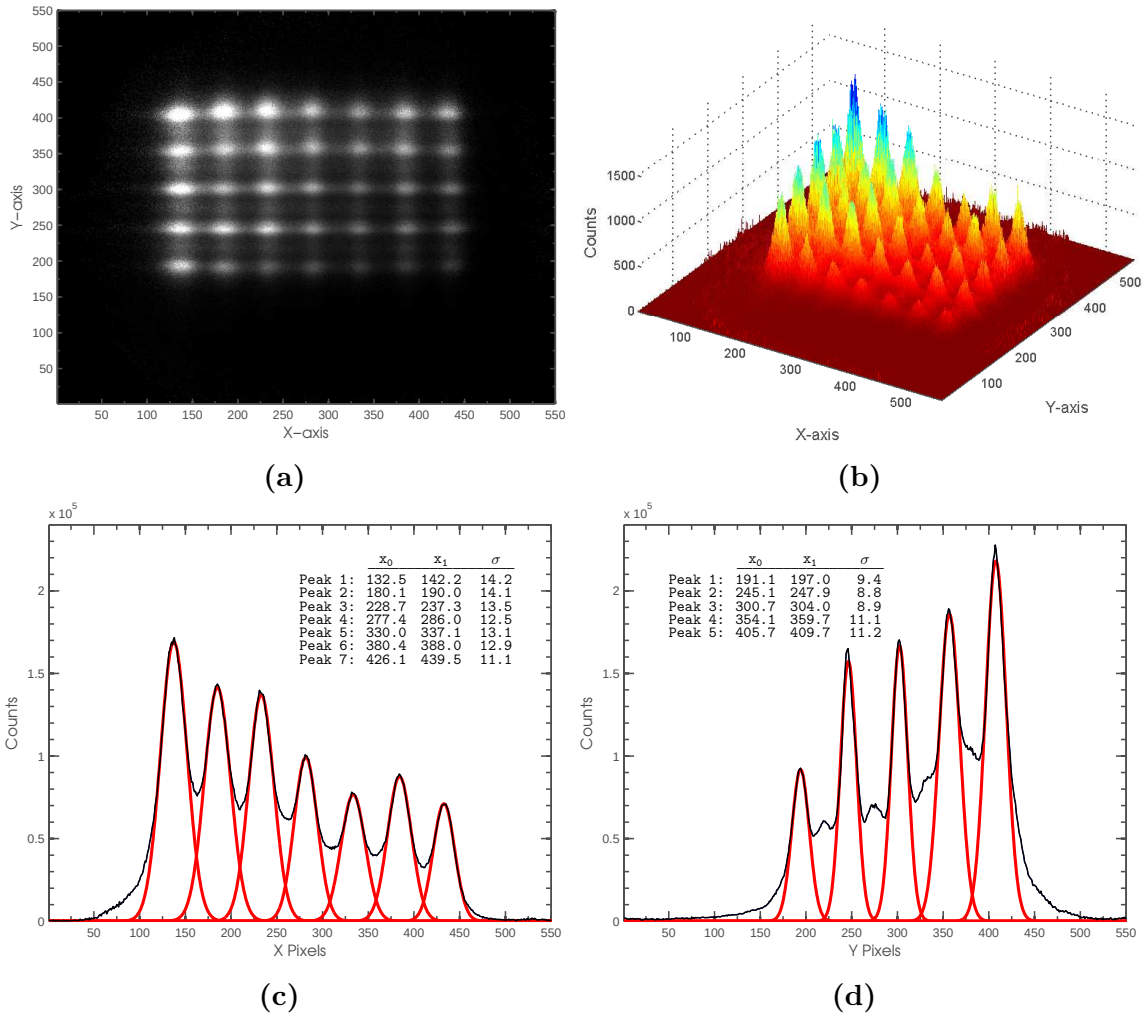

Figure 5.8: Flat-fielded image (a) and a three-dimensional surface plot (b) of the small imaging grid. Projections along the X and Y axes are shown in (c) and (d), respectively.

spatial resolution was again estimated.

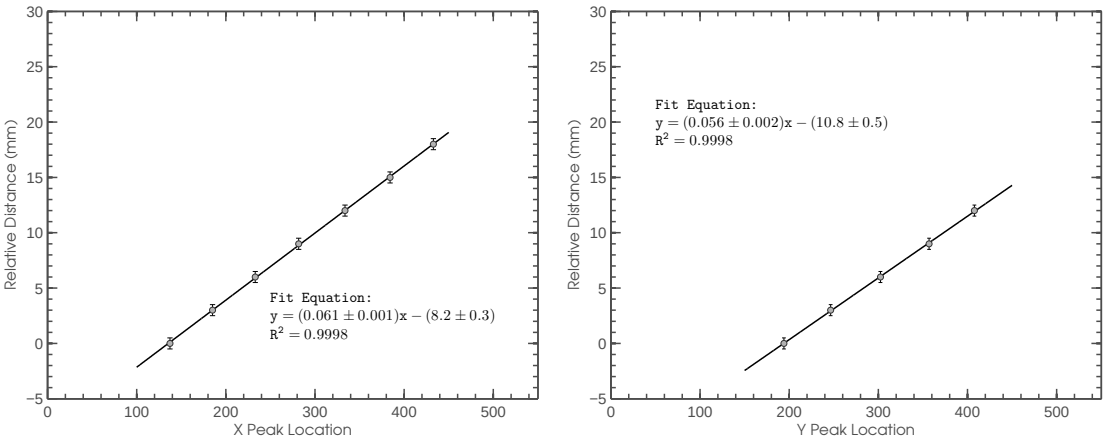

(a) **(b)**

Figure 5.9: Measurement of the pixel dimensions along the X (a) and Y (b) axis using the small imaging grid.

As shown in Equation 5.4 and Equation 5.5, the estimated spatial resolution matches the one previously calculated. Similarly, the Y axis exhibits better spatial resolution than the X axis. While the holes can be individually resolved in the acquired image, it is clearly evident that the peaks are overlapping. This effect is to be expected when the dimensions of the object are near the spatial resolution of the detector.

$$\sigma_{\mathtt{x}} = 0.79 \pm 0.07\,\mathtt{mm} \tag{5.4}$$

$$\sigma_{\mathtt{y}} = 0.56 \pm 0.06\,\mathtt{mm} \tag{5.5}$$

5.2.4 Resolution deconvolution

When the distance between objects approaches the spatial resolution of the imaging system, it becomes extremely difficult to distinguish them in the acquired image. In almost all cases, the objects will just appear as a blurry spot. However, if the

spatial variation in the PSF of the imaging system is known, it is possible to image objects much smaller than the resolution limit. This technique is known as deconvolution imaging and is frequently used in microscopy (Sibarita, 2005), radio astronomy (Lauer, 2002) and computed tomography.

The objective of deconvolution imaging is to reverse the distortion induced by the resolution limit and recover otherwise blurry details. In general all deconvolution techniques need to make some assumptions about the starting conditions. As previously mentioned, it has been assumed that the optical path to the sensor is perfect and the true image is convolved with the PSF to produce the acquired image. If the PSF is known, the acquired image can be convolved with the complementary PSF, resulting in an image which is free from sensor induced distortions. In practice, it is almost impossible to measure the true PSF and approximations must be made. Nevertheless, significant improvements in image quality can be achieved using deconvolution imaging.

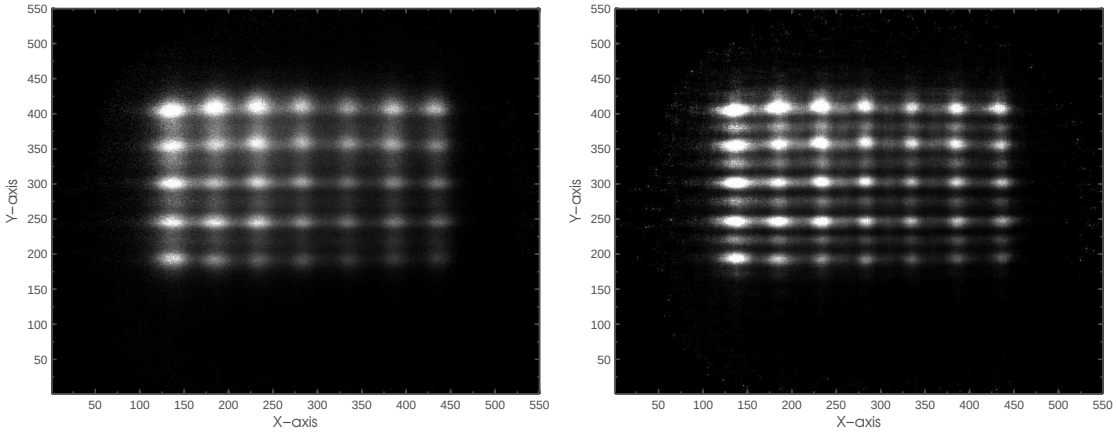

(a) **(b)**

Figure 5.10: Comparison between the normal image (a) and deconvolved image (b) of the small imaging grid. Flat field correction was applied to both images.

In the previous sections, the spatial resolution of the THGEM imaging detector was estimated by fitting the two calibration objects with an error function. In doing so, an assumption was made that the PSF of the detector has a Gaussian-like distribution. Continuing with this assumption, a PSF was generated using the mean standard deviation along each axis and a deconvolution operation was performed between the acquired images and the Gaussian-like PSF. The deconvolution operation was performed using the Richardson-Lucy algorithm (Richardson, 1972) which is available through the `deconvlucy` function in Matlab. Results of the deconvolution operations are presented in Figure 5.10 and Figure 5.11.

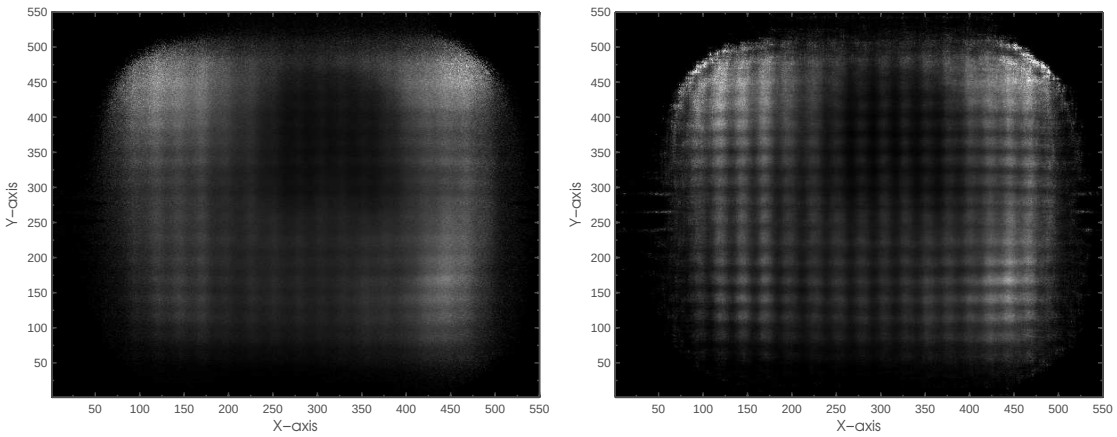

(a) **(b)**

Figure 5.11: Comparison between the normal image (a) and deconvolved image (b) of a radiographic film identification marker. Flat field correction was applied to both images.

While plenty of approximations were made regarding the PSF, the results of the deconvolution are impressive nevertheless. As illustrated in Figure 5.10, significant details are revealed in the acquired image of the small grid object. Since the dimensions of this object are closer to the estimated spatial resolution than the rest, it should be expected that the acquired images are distorted by the PSF. Although the

holes are visible in both images, they appear blurred in the original acquisition while not as much in the deconvolved images.

The final image which was subjected to the deconvolution operation was that of the radiographic film identification marker illustrated in Figure 5.11. Due to the limited spatial resolution of the THGEM imaging detector, the fine details of the marker are not visible. However, it is evident from the outline of the dark region that the imaging object was the letter "*R*". Furthermore, this image is of particular interest since it provides some insight into what presently limits the spatial resolution of the detector. The results of the deconvolution operation, shown in Figure 5.10 (b), reveal an interesting periodic structure across the entire image. The distance between these periodic "*bright*" spots was measured and it exactly matches the pitch of the two-dimensional readout structure. This result is significant as it confirms the spatial resolution, of the THGEM imaging detector, is currently limited by the pitch of the readout structure and not by the diffusion limit. Therefore, it can be concluded that the spatial resolution of the detector can be further improved by increasing the granularity of the readout anode.

5.2.5 Slit imaging

The last image which will be presented in this chapter is that of the *narrow slit* object. In this investigation, a 1.00 ± 0.05 mm slit was machined in a 5.2 ± 0.1 mm block of lead (Pb) and imaged using the THGEM detector. The flat-fielded image, three-dimensional surface plot and the axial projections are presented in Figure 5.12.

Along the X projection, the periodic pattern of the readout electrodes is clearly visible while the Y projection shows the width of the slit. The width of the slit, as described by the FWHM, has been calculated to be 2.0 mm. Although this value is

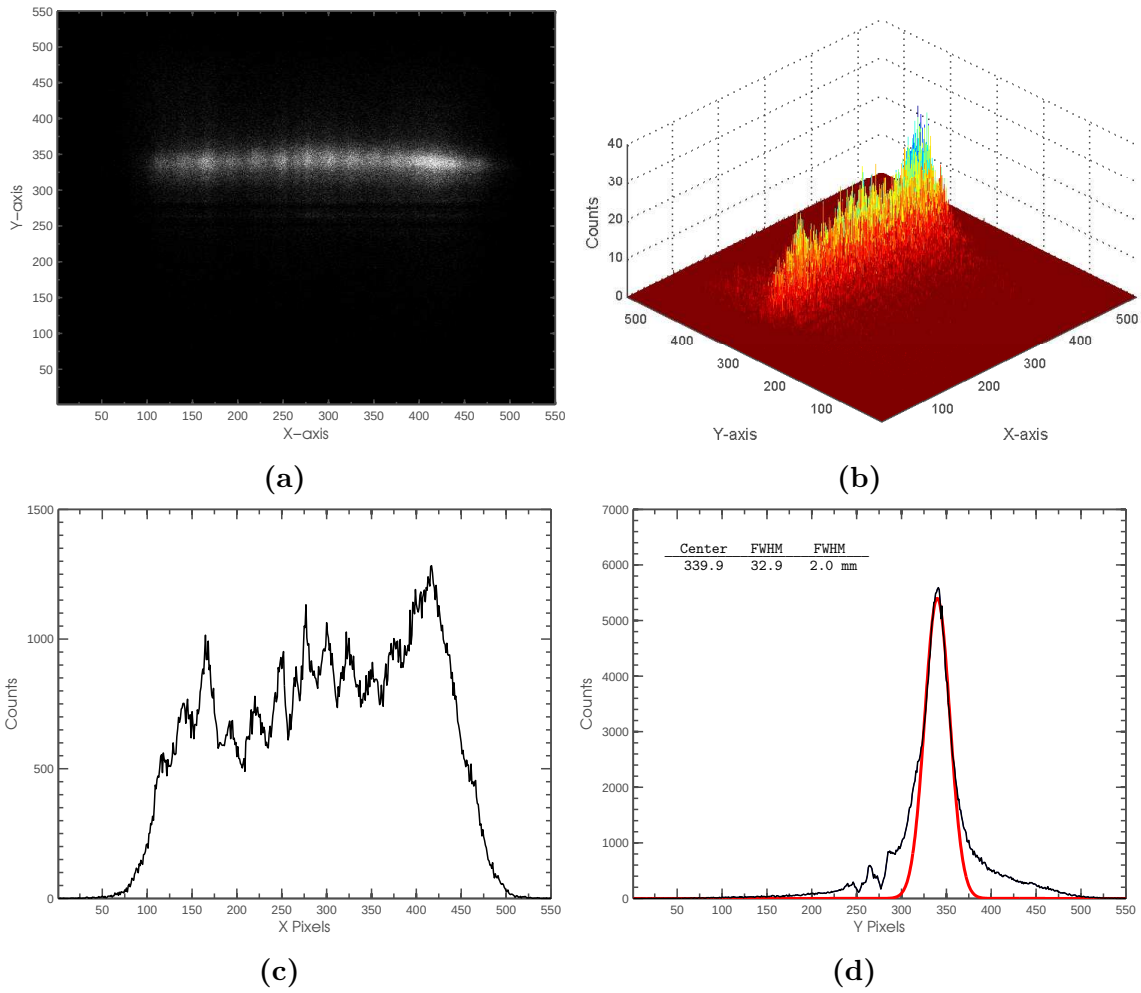

Figure 5.12: Flat-fielded image (a) and a three-dimensional surface plot (b) of the narrow slit object. Projections along the X and Y axes are shown in (c) and (d), respectively.

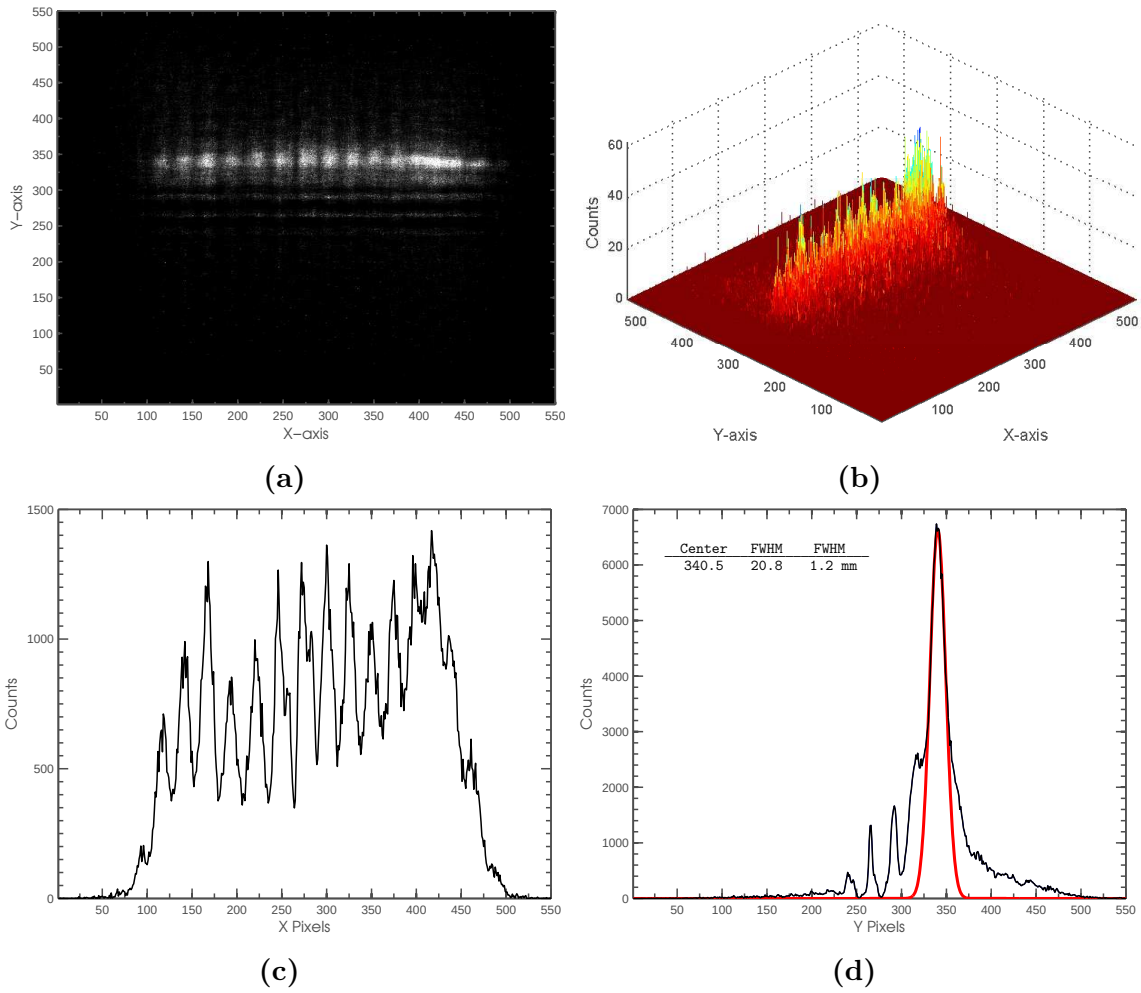

Figure 5.13: Deconvolved image (a) and a three-dimensional surface plot (b) of the narrow slit object. Projections along the X and Y axes are shown in (c) and (d), respectively.

almost twice of the real width, it is to be expected considering the dimensions are so close to the spatial resolution. However, since an estimate for the PSF has been established, the image can be corrected using the deconvolution method. Results of the deconvolution are shown in Figure 5.13.

In the deconvolved image, the periodic pattern of the readout becomes much more clear. The measured width of the slit, as described by the FWHM, is 1.2 mm. Although the measured value does not exactly match the physical dimensions of the slit, the two are in close agreement. One of the primary reasons for this discrepancy is due to the penumbra effect which was previously neglected when attempting to estimate the spatial resolution of the system. In reality, blurring of edges is not entirely caused by the PSF, but also by the optics between the X-ray source and the imaging system. In all cases presented, the objects were at a fixed distance from the cathode of the detector. This extra distance between the object and the detector introduces some magnification due to optics and edge blurring will occur as a consequence of the penumbra effect. It is therefore likely that the spatial resolutions has been slightly overestimated and includes the geometry effects of the source and imaging objects.

5.3 Summary

In this chapter, the imaging capabilities of the prototype THGEM detector have been demonstrated using various test objects. It has been shown that image quality can be improved using a combination of flat-field correction and resolution deconvolution techniques, but fundamentally the images are limited by the current spatial resolution. The spatial resolutions along the X and Y axis have been estimated to

be 0.81 ± 0.09 mm and 0.59 ± 0.09 mm, respectively. In has been clearly demonstrated that the spatial resolution is limited by the pitch of the electrodes on the two-dimensional readout structure. Future designs should consider increasing the granularity of the readout structure to improve the spatial resolution. Additionally, a ground layer should be placed between the top layer and the inner routing layers of the two-dimensional readout. This modification reduces capacitive coupling between the collection electrodes and the inner routing layers, thus minimizing the discrepancy in spatial resolution. To estimate the spatial resolution of the system, some assumptions were made regarding the optics of the imaging system. In reality, effects such as magnification, or blurring due to penumbra, cannot be ignored. From these very basic imaging studies, it can be concluded that the THGEM imaging detector, with two-dimensional delay line readout, is a robust and cost effective solution for large area imaging applications.

Chapter 6

Discussion and Conclusions

The work presented in this thesis describes the design, development and investigation of a two-dimensional, delay line based, THGEM imaging detector. Through the entire process, tremendous knowledge was gained concerning the operation and fabrication of THGEMs, the development of high speed electronics and the preliminary testing of imaging systems. In terms of reaching the primary objectives, the author concludes that this project has been a success. However, the real knowledge was gained in the many failures experienced along the way. The goal of this final chapter is to discuss some of the difficulties encountered and suggest possible solutions for future projects.

One of the most important components of the prototype imaging detector is the THGEM. From the experiments performed in this thesis, it can be concluded that THGEMs with smaller holes produce larger gains, and are more stable, when compared to THGEMs with larger holes. Catastrophic breakdowns were observed on many occasions. Breakdowns are caused by the formation of a conductive layer between the THGEM electrodes which acts as a resistor in parallel with the capacitance of the THGEM. Frequent discharges result in an increase of the conductive layer and also of the leakage current across the THGEM. By monitoring the leakage current, it

should be possible to predict when a catastrophic breakdown is about to occur and reduce the high voltage bias to prevent it from happening. The discharge probability can be reduced by etching a rim in the copper surrounding a THGEM hole and Breskin *et al.* (2009) showed that maximal gain is achieved using a 0.1 mm rim. An adverse effect of the etched rim is long gain stabilization times and increased gain variations. While this may not be a significant problem for timing based applications, it is certainly important in spectroscopy and microdosimetry applications. Experiments by Oliveira *et al.* (2007) have shown that it is possible to protect THGEMs from catastrophic breakdowns by using electrodes which are made of highly resistive materials. The so-called RETGEMs can be operated in the glow discharge region for extended periods of time without catastrophic failure. For RETGEMs, the discharges are stopped by simply reducing the bias voltage and the devices can resume operation without any change in their characteristics. It is strongly recommended that such devices be studied in future projects.

As described in Chapter 2, the imaging detector is biased using two independent high voltage power supplies. One power supply is used for the cathode voltage while the other for the THGEM voltages. To reduce the number of power supplies, the THGEM voltages are generated through a resistive divider. Although economical, this approach wastes a lot of power and imposes a limit on the range of electric fields which can be studied. Consequently, it is expected that the THGEM signal could be improved by using independent power supplies and optimizing the electric field in the different regions of the detector. Corradi *et al.* (2007) presented the design of a high voltage system for a triple GEM detector which could be applied to THGEM detectors. Computer controlled power supplies, such as the aforementioned, can be

used to control the voltage ramping profiles, measure the leakage currents and achieve consistent voltage settings. Such a system should be considered for future THGEM applications.

The THGEM detector is transformed into an imaging sensor by using the two-dimensional readout anode. Fabricated on a 4-layer PCB, the two-dimensional readout incorporates the charge sensing electrodes and the delay line circuits. Although this fabrication technique produces good results, it can certainly be improved. As shown in the Chapter 5, the spatial resolution is slightly better in one axis when compared to the other and it was suggested that this is caused by crosstalk between axes. This conclusion was reached while measuring the time delay of the two-dimensional readout. While probing the sensing electrodes with a pulser, signals were observed on every output of the delay line even when only one axis was tested. The crosstalk is a product of capacitive coupling between the inner routing layer of the 4-layer PCB and can be reduced by separating the layer by a ground layer. Next, the delay line circuits should be optimized to match the input impedance of the pre-amplifiers. The preamplifiers used in the imaging experiments were acquired towards the end of this project and had a fixed input impedance. The delay line circuits were designed much earlier and had their own impedance characteristics. For maximum power transfer, the impedance of the delay line circuit should match that of the preamplifier. Lastly, the sensing electrodes should be reduced in size and pitch to improve the current spatial resolution. A larger number of smaller sensing electrodes will have to be included on the new readout board which will also require a larger delay line circuit. Increasing the granularity of the readout anode, should bring the current spatial resolution closer to the diffusion limit.

In Chapter 5 it was mentioned that some imaging artifacts are caused by crosstalk between adjacent channels on the TDC DAQ. This crosstalk is caused by the grouping of stop channels on the TDC-GPX ASIC. To overcome this issues, an artificial delay can be introduced between the delay line signals. The additional time delay should be longer than the length of the delay line to guarantee that pulse pairs do not reach the stop channels at the same time. Additionally, a version of the TDC DAQ has been developed without NIM-to-TTL converters – see Appendix A.2. This version is intended to be used with the CAEN model N89 level translator module. Lastly, the time required to download a high-resolution image from the TDC DAQ is almost 10 minutes. Using an Ethernet connection should reduce the download time to under 10 seconds. The SiTCP library, developed by Uchida (2008), implements a hardware based Ethernet protocol and will be used in future versions of the TDC DAQ.

Finally, the THGEM imaging detector was demonstrated only in TE-propane gas and at low pressures. In Chapter 1 it was shown that the the photoelectron and Auger electron range is relatively long under these conditions. Increasing the operating pressure will reduce the electron range and subsequently improve the spatial resolution. Additionally, operation in gases such as Xenon (Xe) or Neon (Ne) should improve the detection efficiency due to higher atomic number. Increasing the gas pressure, and the granularity of the readout anode, should produce a significant improvement in the spatial resolution of the THGEM imaging detector.

6.1 Conclusion

A THGEM imaging detector, with a two-dimensional delay line readout, has been constructed. Featuring an imaging area of 40 x 40 mm^2, the prototype detector can be operated under various gas mixtures and pressures. Using two 0.4 mm THGEMs, in a cascade configuration, the detector has been successfully operated in a propane based gas mixture at a pressure of 167 Torr. In these conditions, stable operation has been demonstrated at an effective gain of 10^3. Positional readout was accomplished using a timing based interpolating technique. Two sets of orthogonal electrodes, connected to individual delay lines, serve as a two-dimensional anode readout. The delay lines have a cutoff frequency of 657 MHz and induce an average time delay of 3.4 ns between adjacent electrodes. A TDC based DAQ system has been developed to process the timing signals associated with the delay line readout. Using modern FPGAs, the TDC DAQ is capable of resolving event rates approaching 2.0 MHz and has a DNL much better than 5%. The imaging capabilities of the detector have been demonstrated using a collimated alpha source and a wide area X-ray beam. Under the aforementioned conditions, the detector was able to successfully resolve 1 mm diameter holes spaced 3 mm apart. While low pressure operations are not favorable for imaging, the results obtained in these conditions are certainly impressive. Future studies are recommended, using a larger imaging area and higher gas pressures, to fully characterize the capabilities of this detector concept. Nevertheless, as shown by these preliminary studies, a delay line based THGEM imaging detector is a robust and economic alternative for applications which require large imaging areas with reasonable spatial resolution. The design principles developed in this thesis should serve as a framework for the development of future THGEM imaging detectors.

6.2 Future Work

The design principles presented in this thesis provide a framework for the development of future THGEM based imaging detectors. Imaging results have shown that it is possible to achieve sub-mm spatial resolution using a delay line readout and there is still some room for improvement. From the research presented, future work includes imaging of alpha sources, neutron imaging using appropriate converters and dose imaging in proton or photon therapy. Imaging of alpha particles has already been demonstrated and it should be fairly straight forward to image external sources which are placed on a thin Mylar entrance window. Neutron imaging can be accomplished using either special cathode materials, or gas compositions, which convert the incoming neutrons in (n,p) or (n,α) reactions. Neutron conversion in gas can be easily accomplished by introducing a small amount of ^{3}He into the mixture. Although ^{3}He is expensive, and in short supply, it has a high absorption cross section for thermal neutrons. Medical imaging applications have been demonstrated by Klyachko *et al.* (2011), which used GEMs, and an optical readout method, as a beam monitoring device for radiotherapy. A much more robust and economical device can be built using the THGEM concept presented here and with the same spatial resolution.

Additionally, the system can provide spectroscopic information from the trigger signal which can be used for energy gating. If the THGEMs are operated in the proportional region, the trigger signal will also be proportional to the incident energy. This is useful for applications such as dual energy X-ray absorption spectroscopy and imaging spectrometry.

Appendix A

Appendix

A.1 Gas Containment Chamber

The gas containment chamber, used for the prototype imaging detector, consists of a main chamber body, a covering lid with interchangeable entrance windows and a flange to seal the window. Technical drawings for all three parts are included in Figure A.2, Figure A.3, and Figure A.4, respectively. Fabricated from 6061 aluminium, the chamber houses the THGEM assembly, the high voltage dividers, and the readout anode. Electrical connections are provided via two SHV5 high voltage connectors and five BNC signal connectors.

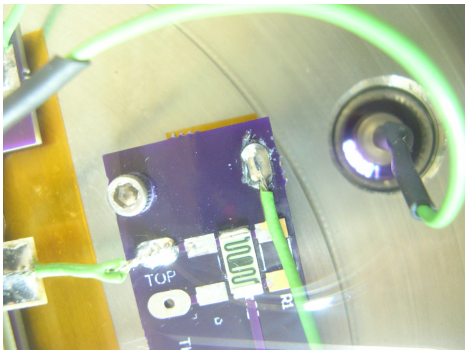

Figure A.1: Paschen discharge inside an SHV5 connector biased to -2000 volts in TE-propane at 167 Torr.

It is important to mention the SHV5 connectors were intended for use in high vacuum applications. As such, they do not include a ceramic insulator to shield the central conductor from the connector body, which is usually at ground potential. For applications using low gas pressures (100 Torr) and bias voltages greater than 2000 volts, Paschen discharges were observed between the center conductor and the connector body – see Figure A.1. To stop these discharges, a plastic insulator was fabricated to fit between the central conductor and the connector body.

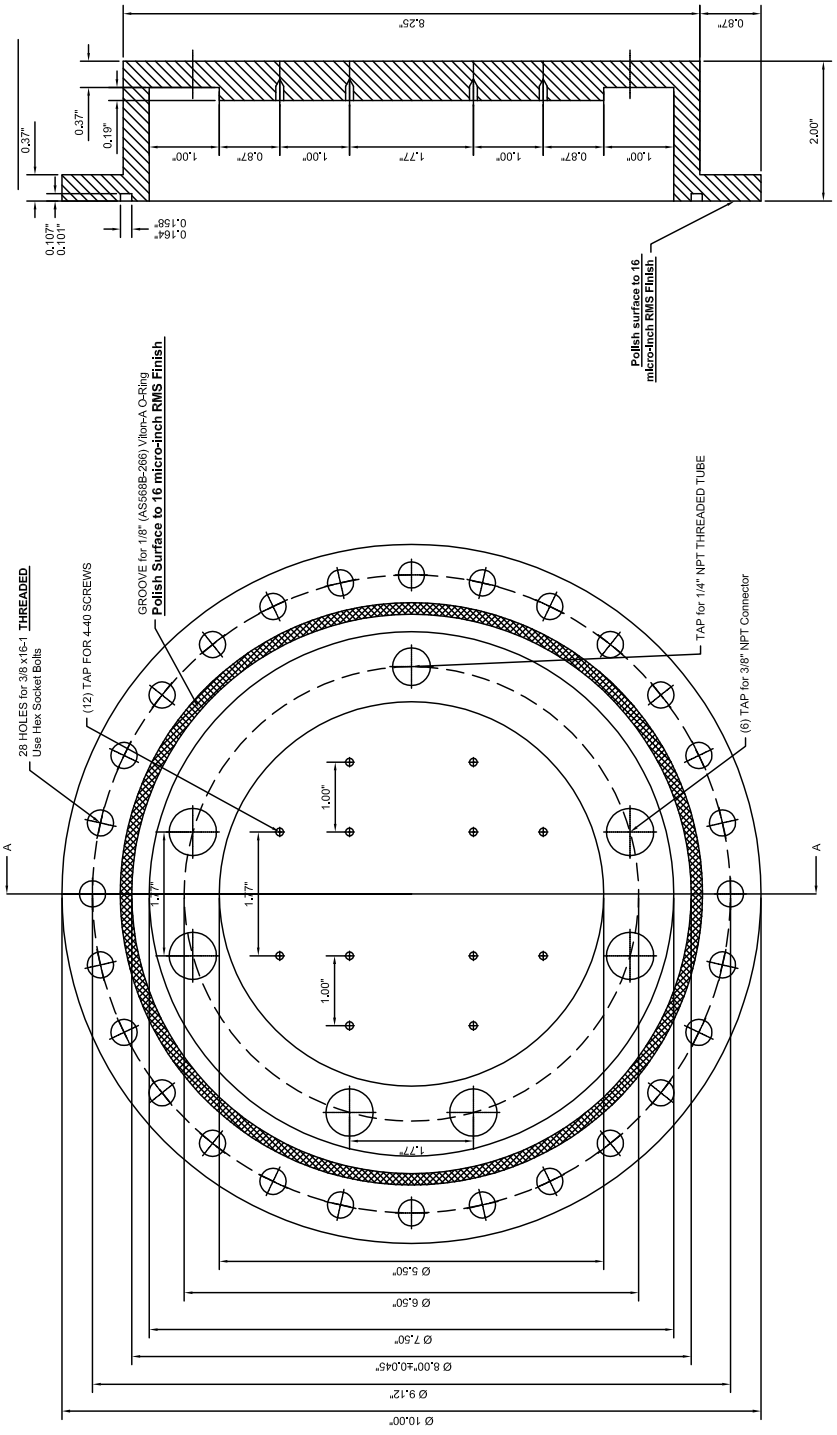

Figure A.2: Technical drawing of the aluminium (6061) gas containment chamber used in the THGEM imaging detector. The chamber is sealed by a lid with interchangeable entrance window types.

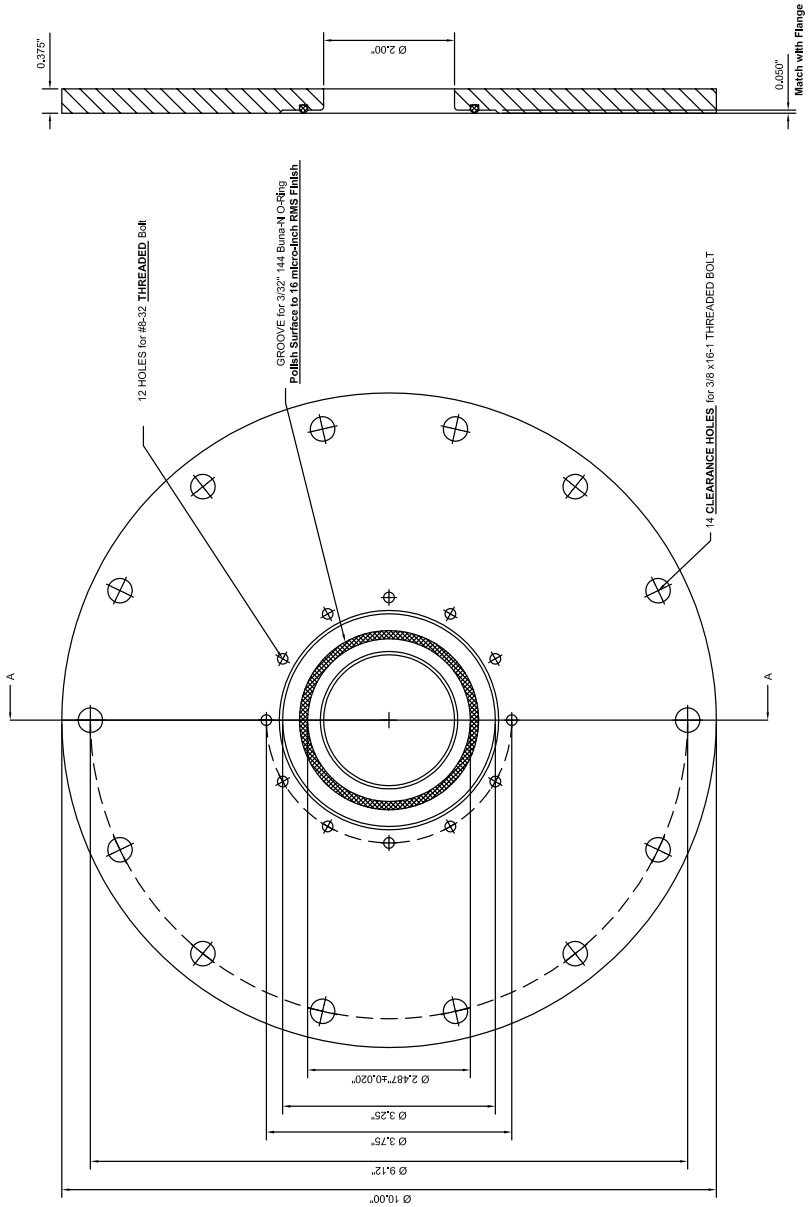

Figure A.3: Technical drawing of the aluminium (6061) lid used to seal the gas containment chamber. The lid has a 2 inch opening in the middle which accept various entrance window types.

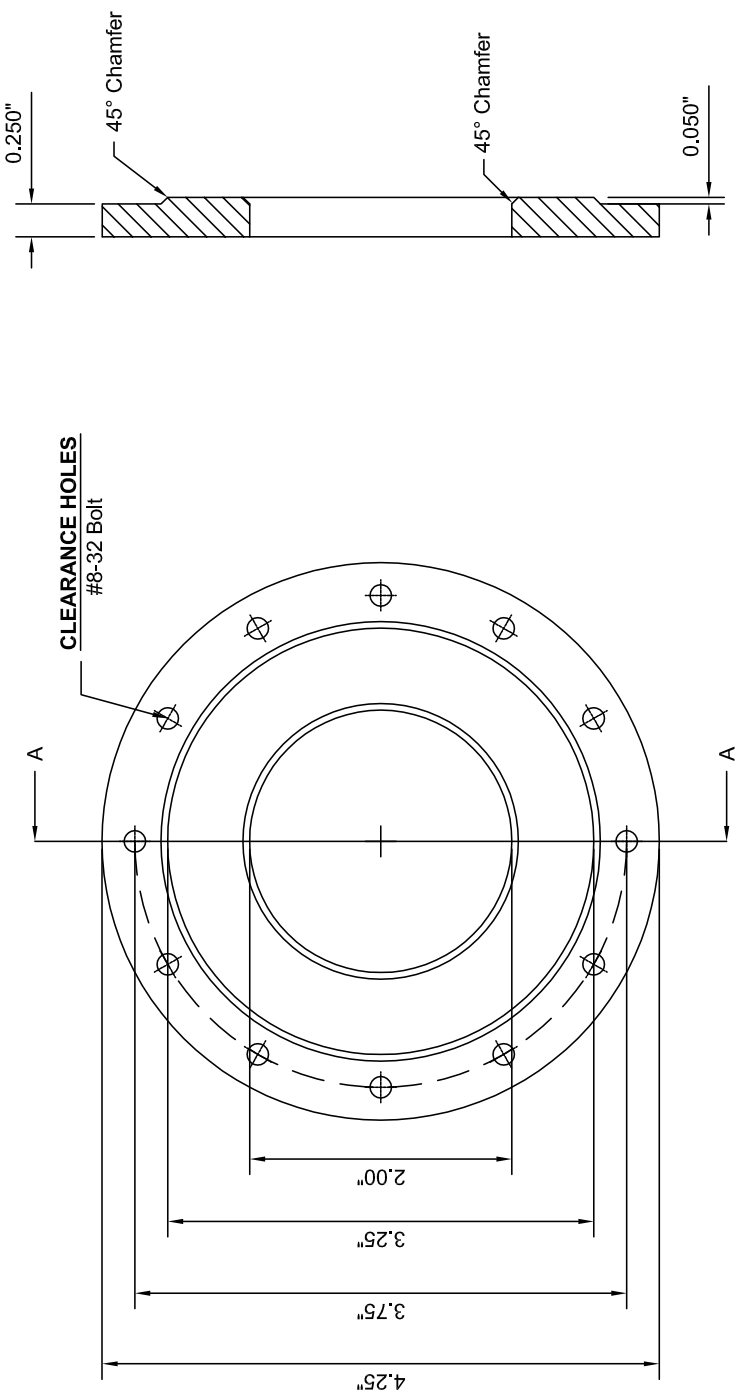

Figure A.4: Technical drawing of the aluminium (6061) flange use to seal the entrance window to the lid of the gas containment chamber.

A.2 Schematics and renderings of the TDC DAQ module

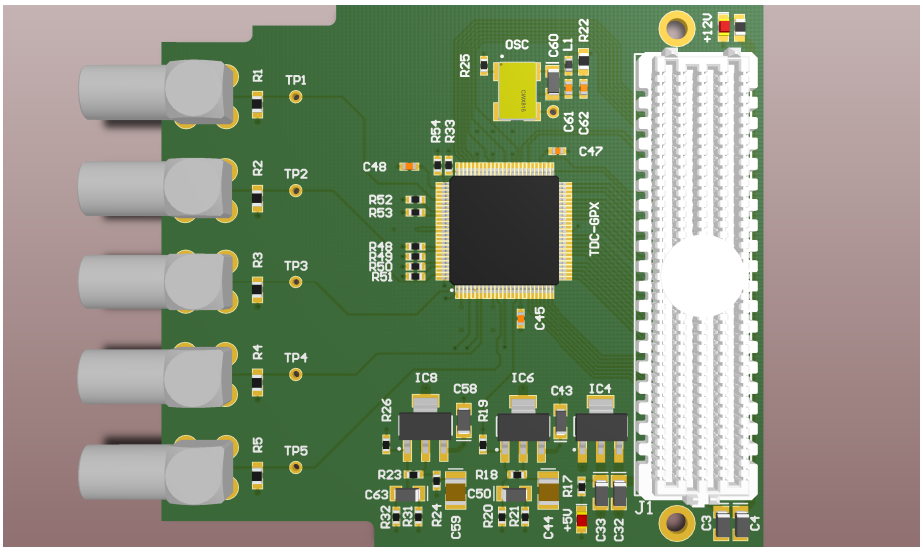

(a)

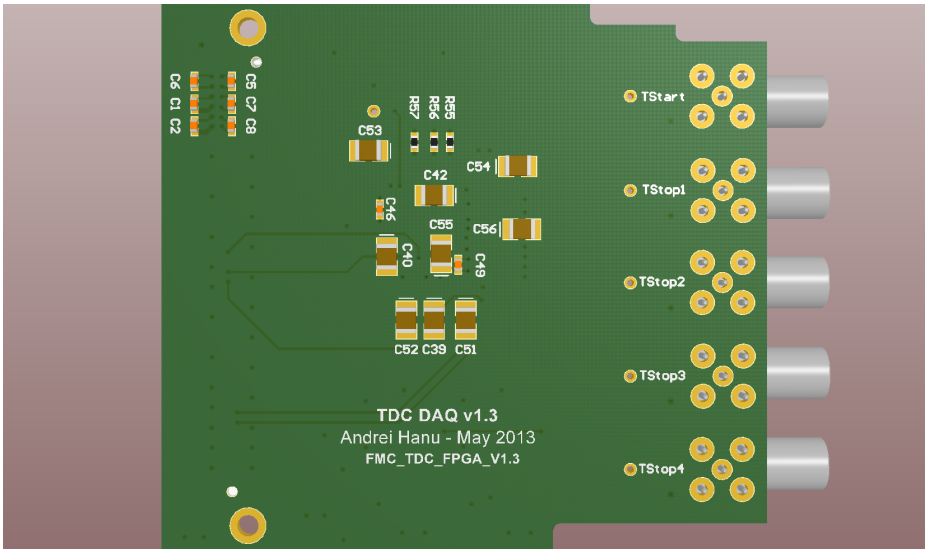

(b)

Figure A.5: Three-dimensional renderings showing the top (a) and bottom (b) of the TDC DAQ module. Illustrated here is version 1.3, which does not include the NIM-to-LVTTL converter circuits.

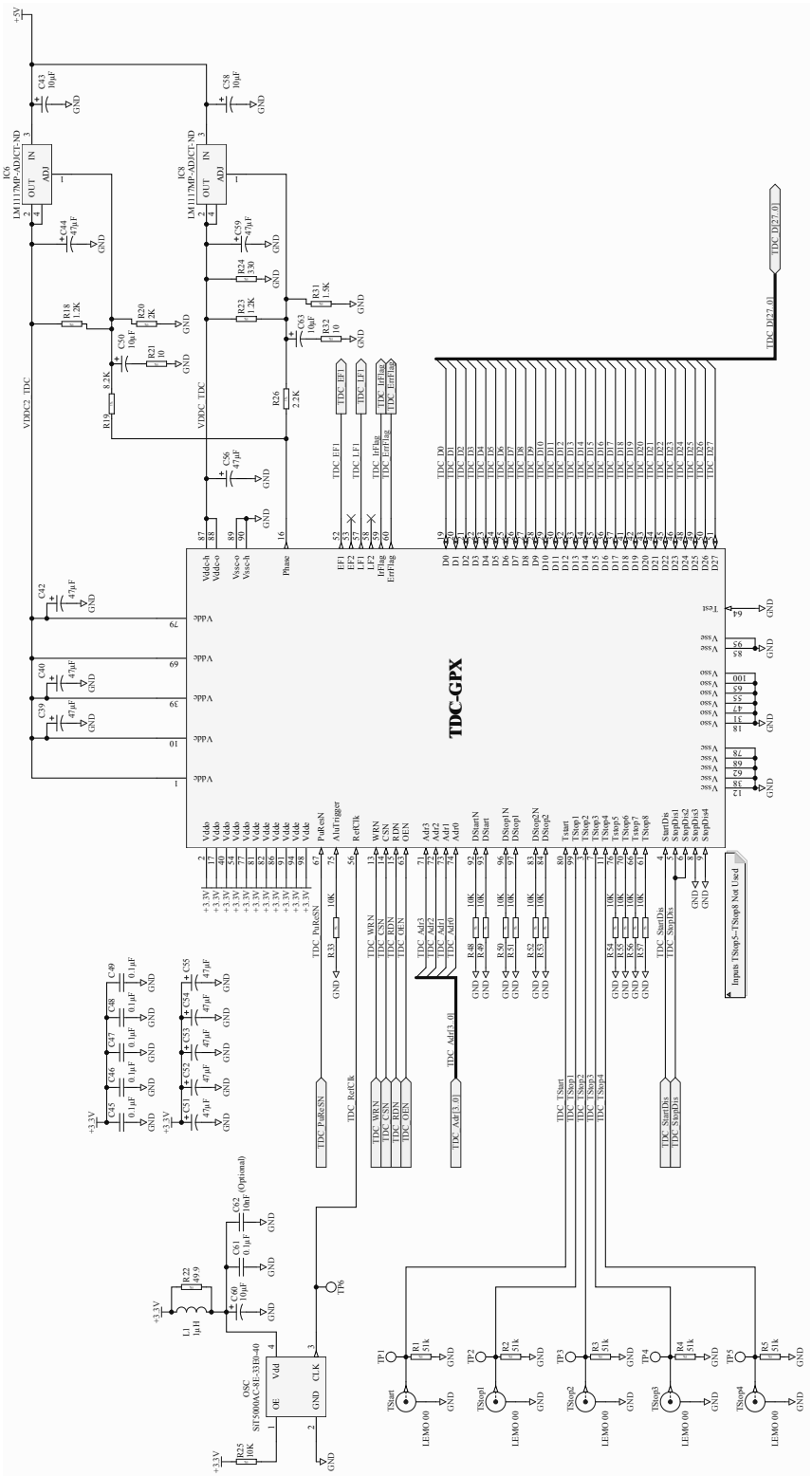

Figure A.6: Schematics diagram for the power supply, clock and input to the TDC-GPX on the TDC DAQ module. Shown here is version 1.3, which does not include the NIM-to-LVTTL converter circuits.

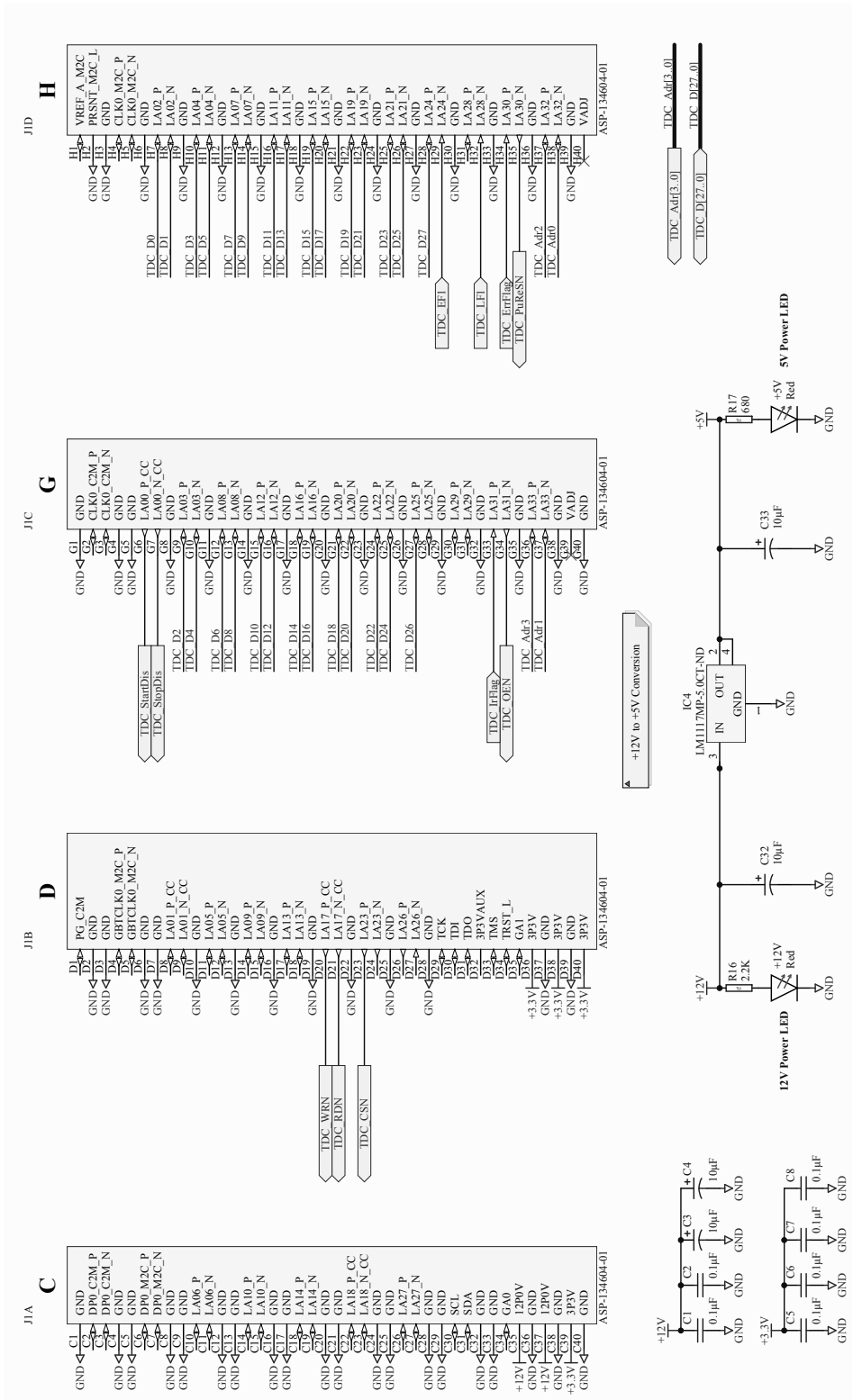

Figure A.7: Schematics diagram for the wiring of the LPC FMC connector. Shown here is version 1.3, which does not include the NIM-to-LVTTL converter circuits.

A.3 TDC-GPX Read-Write Controller

For the FPGA to communicate with the TDC-GPX, it was necessary to implement the timing requirements of the proprietary communication protocol. As illustrated in Figure A.8, read and write timing constraints are generated using a 100 MHz clock derived from the 200 MHz differential clock on-board the SP601 FPGA. As can be seen in the timing diagrams, a single read or write cycle takes 5 clock cycles allowing for continuous read or write operations at 20 MHz. During a single window mode acquisition on the TDC DAQ, a continuous read of 4 time measurements adds an additional dead time of 200 ns.

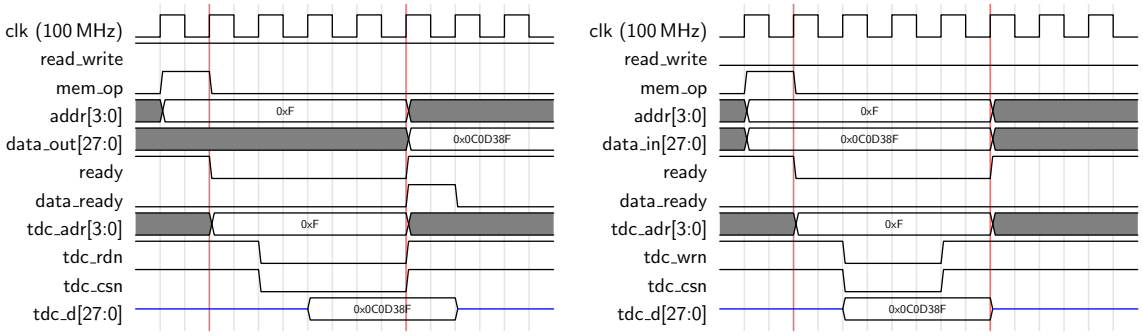

(a) **(b)**

Figure A.8: Timing diagram for implementing a) read and b) write operations using the proprietary communication protocol on the TDC-GPX.

The following code, written in the Verilog HDL, implements the aforementioned timing constraints required for communication with the TDC-GPX ASIC. The timing logic is implemented using the Asynchronous State Machine and Datapath (ASMD) process which generates sequential logic for combined control and dataflow.

```
module TDC_GPX_Read_Write_Controller(
   // Synchronous Clock & Asynchronous Reset
   input wire clk, reset,

   // To & From The Main Controller
   output wire ready,
   output wire [27:0] data_out,
   input wire [27:0] data_in,
   input wire [3:0] addr,
   input wire read_write,
   input wire mem_op,
   output wire data_ready,

   // To & From TDC-GPX Chip
   inout wire [27:0] tdc_d,
   output wire [3:0] tdc_addr,
   output wire tdc_wrn,
   output wire tdc_rdn,
   output wire tdc_csn,
   output wire tdc_oen
);

// Symbolic State Declaration
localparam [3:0]
   idle  = 4'b0000,
   write1  = 4'b0001,
   write2  = 4'b0010,
   write3  = 4'b0011,
   write4  = 4'b0100,
   read1  = 4'b0101,
   read2  = 4'b0110,
   read3  = 4'b0111,
   read4  = 4'b1000;

// Internal Signal Declaration
reg ready_reg, ready_buff;
reg [3:0] state_reg, state_next;
reg [27:0] data_out_reg, data_out_next;
reg [27:0] data_in_reg, data_in_next;
reg [3:0] addr_reg, addr_next;
reg tri_reg, tri_buff;
reg tdc_wrn_reg, tdc_wrn_buff;
reg tdc_rdn_reg, tdc_rdn_buff;
reg tdc_csn_reg, tdc_csn_buff;
reg tdc_oen_reg, tdc_oen_buff;
reg data_ready_reg, data_ready_buff;

// FSMD state & data registers
always @(posedge clk, posedge reset) begin
   if (reset) begin
      state_reg <= idle;
      ready_reg <= 1;
      data_out_reg <= 0;
      data_in_reg <= 0;
      addr_reg <= 0;
      tri_reg <= 1;
      tdc_wrn_reg <= 1;
      tdc_rdn_reg <= 1;
      tdc_csn_reg <= 1;
      tdc_oen_reg <= 1;
      data_ready_reg <= 0;
   end else begin
      state_reg <= state_next;
      ready_reg <= ready_buff;
      data_out_reg <= data_out_next;
      data_in_reg <= data_in_next;
      addr_reg <= addr_next;
      tri_reg <= tri_buff;
      tdc_wrn_reg <= tdc_wrn_buff;
      tdc_rdn_reg <= tdc_rdn_buff;
      tdc_csn_reg <= tdc_csn_buff;
      tdc_oen_reg <= tdc_oen_buff;
      data_ready_reg <= data_ready_buff;
   end
end

// FSMD next-state logic
always @* begin
   data_out_next = data_out_reg;
   data_in_next = data_in_reg;
```

```
   addr_next = addr_reg;

   case (state_reg)
   idle:
   begin
      if (~mem_op)
         state_next = idle;
      else begin
         // Load the address
         addr_next = addr;
         // Read or Write operation
         if (read_write)
            // Read Operation
            state_next = read1;
         else begin
            // Write Operation
            data_in_next = data_in;
            state_next = write1;
         end
      end
   end
   write1:
      state_next = write2;
   write2:
      state_next = write3;
   write3:
      state_next = write4;
   write4:
      state_next = idle;
   read1:
      state_next = read2;
   read2:
      state_next = read3;
   read3:
      state_next = read4;
   read4:
      begin
         data_out_next = tdc_d;
         state_next = idle;
      end
   default:
      state_next = idle;
   endcase
end

// look-ahead output logic
always @* begin
   ready_buff   = 1'b0;
   tri_buff   = 1'b1;
   tdc_wrn_buff  = 1'b1;
   tdc_rdn_buff  = 1'b1;
   tdc_csn_buff  = 1'b1;
   tdc_oen_buff  = 1'b1;
   data_ready_buff = 1'b0;

   case (state_next)
   idle:
   begin
      ready_buff = 1'b1;
      if (state_reg == read4) begin
         data_ready_buff = 1'b1;
      end
   end
   write2:
   begin
      tdc_wrn_buff = 1'b0;
      tdc_csn_buff = 1'b0;
      tri_buff = 1'b0;
   end
   write3:
   begin
      tdc_wrn_buff = 1'b0;
      tdc_csn_buff = 1'b0;
      tri_buff = 1'b0;
   end
   write4:
      tri_buff = 1'b0;
   read2:
   begin
      tdc_rdn_buff = 1'b0;
      tdc_csn_buff = 1'b0;
      tdc_oen_buff = 1'b0;
```

```
   end
   read3:
   begin
      tdc_rdn_buff = 1'b0;
      tdc_csn_buff = 1'b0;
      tdc_oen_buff = 1'b0;
   end
   read4:
   begin
      tdc_rdn_buff = 1'b0;
      tdc_csn_buff = 1'b0;
      tdc_oen_buff = 1'b0;
   end
   endcase
end

// To Main System
assign ready = ready_reg;
assign data_out = data_out_reg;
assign data_ready = data_ready_reg;

// To TDC-GPX
assign tdc_addr = addr_reg;
assign tdc_wrn = tdc_wrn_reg;
assign tdc_rdn = tdc_rdn_reg;
assign tdc_csn = tdc_csn_reg;
assign tdc_oen = tdc_oen_reg;
assign tdc_d = (~tri_reg) ? data_in_reg : 28'bZ;
endmodule
```

A.4 TDC-GPX Core Controller

```
module TDC_GPX_Core_Controller (
   // Synchronous Clock & Asynchronous Reset
   input wire clk, reset,

   // Control Signals
   input wire cntrlPuReSN,
   input wire cntrlConfigure,
   input wire cntrlStartStop,

   // TDC-GPX Control Signals
   output wire tdc_startdis,
   output wire tdc_stopdis,
   output wire tdc_puresn,
   input wire tdc_ef1,
   input wire tdc_lf1,
   input wire tdc_irflag,
   input wire tdc_errflag,

   // TDC-GPX Read/Write Controller Signals
   input wire rw_ready,
   input wire [27:0] rw_data_out,
   output wire [27:0] rw_data_in,
   output wire [3:0] rw_addr,
   output wire rw_read_write,
   output wire rw_mem_op,
   input wire rw_data_ready,

   // FIFO Write Interface
   input wire fifo_full,
   output wire [31:0] fifo_din,
   output wire fifo_wr_en
);

// Symbolic State Declaration
localparam [3:0]
   idle     =  4'b0000,
   puresn    = 4'b0001,
   configure   = 4'b0010,
   configure_wait  = 4'b0011,
   zero    = 4'b0100,
   zero_wait   = 4'b0101,
   acquire    = 4'b0110,
   read    = 4'b0111,
   read_wait   = 4'b1000,
   master_reset  = 4'b1001,
   master_reset_wait = 4'b1010;

// Internal Signal Declaration
reg [3:0] state_reg, state_next;
reg [7:0] cnt_reg, cnt_next;
reg tdc_startdis_reg, tdc_startdis_buff;
reg tdc_stopdis_reg, tdc_stopdis_buff;
reg tdc_puresn_reg, tdc_puresn_buff;
reg [27:0] rw_data_in_reg, rw_data_in_next;
reg [3:0] rw_addr_reg, rw_addr_next;
reg rw_read_write_reg, rw_read_write_next;
reg rw_mem_op_reg, rw_mem_op_buff;
reg [31:0] fifo_din_reg, fifo_din_next;
reg fifo_wr_en_reg, fifo_wr_en_buff;

// FSMD state & data registers
always @(posedge clk, posedge reset) begin
   if (reset) begin
      // Asynchronous Reset
      state_reg <= idle;
      cnt_reg <= 0;
      tdc_startdis_reg <= 1;
      tdc_stopdis_reg <= 1;
      tdc_puresn_reg <= 1;
      rw_data_in_reg <= 0;
      rw_addr_reg <= 0;
      rw_read_write_reg <= 1;
      rw_mem_op_reg <= 0;
      fifo_din_reg <= 0;
      fifo_wr_en_reg <= 0;
   end else begin
```

```
      // Synchronous CLK edge
      state_reg <= state_next;
      cnt_reg <= cnt_next;
      tdc_startdis_reg <= tdc_startdis_buff;
      tdc_stopdis_reg <= tdc_stopdis_buff;
      tdc_puresn_reg <= tdc_puresn_buff;
      rw_data_in_reg <= rw_data_in_next;
      rw_addr_reg <= rw_addr_next;
      rw_read_write_reg <= rw_read_write_next;
      rw_mem_op_reg <= rw_mem_op_buff;
      fifo_din_reg <= fifo_din_next;
      fifo_wr_en_reg <= fifo_wr_en_buff;
   end
end

// FSMD next-state logic
always @* begin
   state_next = state_reg;
   cnt_next = cnt_reg;
   rw_data_in_next = rw_data_in_reg;
   rw_addr_next = rw_addr_reg;
   rw_read_write_next = rw_read_write_reg;
   fifo_din_next = fifo_din_reg;

   case (state_reg)
   idle:
      begin
         if (cntrlPuReSN) begin
            // Power Up Reset Request
            cnt_next = 61;
            state_next = puresn;
         end else if (cntrlConfigure) begin
            // Configure TDC-GPX Request
            cnt_next = 12;
            state_next = configure;
         end else if (cntrlStartStop) begin
            // Start Acquisition Request
            if (~tdc_irflag) begin
               state_next = zero;
               end
         end
      end
   puresn:
      begin
         cnt_next = cnt_reg - 1;
         if(cnt_next == 0)
            state_next = idle;
      end
   configure:
      begin
         if (rw_ready) begin
            // Write Operation
            rw_read_write_next = 0;
            // Go to a wait state (1 clk cycle)
            state_next = configure_wait;
            // Decrement Counter
            cnt_next = cnt_reg - 1;
            // Which register are we on
            case (cnt_next)
            11:
               begin
                  // Register 0
                  // Rising edges, Start ring oscillator
                  rw_addr_next   =  0;
                  rw_data_in_next  =  28'h007FC81;
               end
            10:
               begin
                  // Register 1
                  // Channel Adjustment
                  rw_addr_next   =  1;
                  rw_data_in_next  =  28'h0000000;
               end
            9:
               begin
                  // Register 2
                  // I-Mode
                  rw_addr_next   =  2;
                  rw_data_in_next  =  28'h0000002;
               end
            8:
               begin
```

```
            // Register 3
            rw_addr_next   =  3;
            rw_data_in_next  =  28'h0000000;
          end
        7:
          begin
            // Register 4
            // Mtimes trig. by Start, EFlagHiZN
            rw_addr_next   =  4;
            rw_data_in_next  =  28'h6000000;
          end
        6:
          begin
            // Register 5
            // StartOff1 = 100ns, MasterAluTrig
            // No StopDisStart, StartDisStart
            rw_addr_next   =  5;
            rw_data_in_next  =  28'h0C004DA;
          end
        5:
          begin
            // Register 6
            rw_addr_next   =  6;
            rw_data_in_next  =  28'h0000000;
          end
        4:
          begin
            // Register 7
            // Resolution = 82.3045ps | MTimer = 250 nsec
            rw_addr_next   =  7;
            rw_data_in_next  =  28'h0051FB4;
          end
        3:
          begin
            // Register 11
            rw_addr_next   =  11;
            rw_data_in_next  =  28'h0000000;
          end
        2:
          begin
            // Register 12
            // Mtimer -> IrFlag
            rw_addr_next   =  12;
            rw_data_in_next  =  28'h2000000;
          end
        1:
          begin
            // Register 14
            rw_addr_next   =  14;
            rw_data_in_next  =  28'h0000000;
          end
        0:
          begin
            // Master Reset
            state_next = master_reset;
          end
        endcase
      end
    end
  configure_wait:
    begin
      state_next = configure;
    end
  zero:
    begin
      // FIFO Full?
      if (~fifo_full) begin
        // Send timestamp to FIFO
        fifo_din_next = 32'hFFFFFFFF;
        // Go to wait state
        state_next = zero_wait;
        end
      end
  zero_wait:
    begin
      state_next = acquire;
    end
  acquire:
    begin
      // Check the IrFlag
      // HIGH - End of Time Window Reached
      // LOW - Acquiring
```

```
         if (tdc_irflag) begin
            state_next = read;
         end
      end
   read:
      begin
         // Check the TDC FIFO Empty Flag
         // HIGH - FIFO Empty
         // LOW - FIFO Contains Data
         if (tdc_ef1) begin
            // No data available
            state_next = master_reset;
         end
         else begin
            // FIFO Full?
            if (~fifo_full) begin
               // Data available
               if (rw_ready) begin
                  // Read Operation
                  rw_read_write_next = 1;
                  // Register 8
                  rw_addr_next   =  8;
                  // Go to wait state
                  state_next = read_wait;
               end
            end
         end
      end
   read_wait:
      begin
         // Is data ready?
         if (rw_data_ready) begin
            // Send timestamp to FIFO
            fifo_din_next[27:0] = rw_data_out;
            fifo_din_next[31:28] = 4'h0;
            // Check for more data
            state_next = read;
         end
      end
   master_reset:
      // Master Reset
      begin
         if (rw_ready) begin
            // Write Operation
            rw_read_write_next = 0;
            // Register 4
            rw_addr_next   =  4;
            rw_data_in_next  =  28'h6400000;
            // Go to wait state
            state_next = master_reset_wait;
         end
      end
   master_reset_wait:
      begin
         // Return to IDLE
         state_next = idle;
      end
   default:
      state_next = idle;
   endcase
end

// look-ahead output logic
always @* begin
   tdc_startdis_buff = 1;
   tdc_stopdis_buff = 1;
   tdc_puresn_buff = 1;
   rw_mem_op_buff = 0;
   fifo_wr_en_buff = 0;

   case (state_next)
   puresn:
      tdc_puresn_buff = 0;
   configure_wait:
      rw_mem_op_buff = 1;
   zero_wait:
      fifo_wr_en_buff = 1;
   acquire:
      begin
         // Enable Inputs
         tdc_startdis_buff = 0;
         tdc_stopdis_buff = 0;
```

```
      end
   read:
      begin
         if (state_reg == read_wait) begin
            // FIFO Write Enable
            fifo_wr_en_buff = 1;
         end
      end
   read_wait:
      begin
         if (state_reg == read) begin
            // Strobe Memory Operation
            rw_mem_op_buff = 1;
         end
      end
   master_reset_wait:
      begin
         // Strobe Memory Operation
         rw_mem_op_buff = 1;
      end
   endcase
end

// To TDC-GPX
assign tdc_startdis = tdc_startdis_reg;
assign tdc_stopdis = tdc_stopdis_reg;
assign tdc_puresn = tdc_puresn_reg;

// To TDC-GPX Read/Write Controller
assign rw_data_in = rw_data_in_reg;
assign rw_addr = rw_addr_reg;
assign rw_read_write = rw_read_write_reg;
assign rw_mem_op = rw_mem_op_reg;

// To the FIFO
assign fifo_din = fifo_din_reg;
assign fifo_wr_en = fifo_wr_en_reg;

endmodule
```

A.5 THGEM microdosimetry paper

The work presented in the following manuscript describes the development of a Geant4 Monte Carlo code to investigate the neutron microdosimetric responses of the THGEM detector. In this study, the energy deposited per incident neutron event was converted to the lineal energy (y), which is a fundamental microdosimetric quantity. The lineal energy distribution, known as the microdosimetric spectrum, was used to evaluate the THGEM detector response. Results for various neutron energies, and incidence angles, are presented in this manuscript. A modified version of this code was used by Anjomani *et al.* (2013) to study design parameters for a new multi-element THGEM based microdosimetric detector.

The simulation work presented in this paper was performed solely by the author of this thesis under the supervision of Dr. Soo-Hyun Byun. The manuscript was also written by the thesis author and edited Dr. Soo-Hyun Byun and Dr. William V. Prestwich.

This article has been reprinted from Nuclear Instruments and Methods in Physics Research A, Vol. 622, A. Hanu, S.H. Byun and W.V. Prestwich, A Monte Carlo simulation of the microdosimetric response for thick gas electron multiplier, Pages 270-275, Copyright 2010, with permission from Elsevier.

Nuclear Instruments and Methods in Physics Research A 622 (2010) 270–275

Contents lists available at ScienceDirect

Nuclear Instruments and Methods in Physics Research A

journal homepage: www.elsevier.com/locate/nima

A Monte Carlo simulation of the microdosimetric response for thick gas electron multiplier

A. Hanu *, S.H. Byun, W.V. Prestwich

Department of Medical Physics and Applied Radiation Sciences, McMaster University, 1280 Main Street West, Hamilton, ON, Canada L8S 4K1

ARTICLE INFO

Article history:
Received 1 April 2010
Received in revised form
21 June 2010
Accepted 5 July 2010
Available online 8 July 2010

Keywords:
Monte Carlo simulation
Thick gas electron multiplier
Microdosimetry
Geant4

ABSTRACT

The neutron microdosimetric responses of the thick gas electron multiplier (THGEM) detector were simulated. The THGEM is a promising device for microdosimetry, particularly for measuring the dose spectra of intense radiation fields and for collecting two-dimensional microdosimetric distributions. To investigate the response of the prototype THGEM microdosimetric detector, a simulation was developed using the Geant4 Monte Carlo code. The simulation calculates the deposited energy in the detector sensitive volume for an incident neutron beam. Both neutron energy and angular responses were computed for various neutron beam conditions. The energy response was compared with the reported experimental microdosimetric spectra as well as the evaluated fluence-to-kerma conversion coefficients. The effects of using non-tissue equivalent materials were also investigated by comparing the THGEM detector response with the response of an ideal detector in identical neutron field conditions. The result of the angular response simulations revealed severe angular dependencies for neutron energies above 100 keV. The simulation of a modified detector design gave an angular response pattern close to the ideal case, showing a fluctuation of less than 10% over the entire angular range.

1. Introduction

Microdosimetry aims to study how different types of radiation transfer their energy into micro-volumes of the order of cellular and sub-cellular structures. The final product from a microdosimetric study is the distribution of lineal energies, which can be used to calculate the absorbed dose and predict the radiobiological effectiveness of radiation. Due to its ability to provide a quantitative dose measurement along with a dose spectrum, microdosimetry has been applied to a wide range of fields including radiation physics, radiation protection and radiobiology [1].

Until recently, the standard device used in microdosimetry has been the low-pressure tissue-equivalent proportional counter (TEPC). Although generally regarded as the best available device, particularly for mixed neutron–gamma field dosimetry, standard TEPCs have several shortcomings [2]. When coupled to a fast digital or analog pulse processing system, a standard ½-inch TEPC can be reliably operated at a neutron dose rate of 20 mGy/min with a moderate dead time of 15% [3]. However, as the neutron dose rate increases, the dead time increases rapidly. As a result, making quantitative measurements is impossible for the dose rates typically encountered in therapeutic applications. Since there is little room for enhancing the pulse processing systems, the sensitive volume of the detector must be reduced to allow for operation at high dose rates. Several attempts have been made to reduce the sensitive volumes of TEPCs, allowing for operations up to a neutron dose rate of 333 mGy/min [4–6]. However, reducing the gaseous volume makes the detector fabrication and assembly a very difficult task due to the tiny size of the central anode wire.

With the increasing need to understand the biological effects of densely ionizing radiation, simulation of smaller tissue sites is required. In general, this is accomplished by lowering the gas pressure inside the cavity. However, normal-sized TEPCs cannot be easily operated at pressures low enough to simulate nanometric sites. Reducing the gaseous cavity volume allows for an increase in pressure, though, it encounters the same fabrication and assembly problem as previously mentioned. Such limitations require developing new detectors with greater flexibility in gaseous volume change.

With rapid developments in the field of micro-pattern gaseous detectors, the most successful detector is the gas electron multiplier (GEM) [7]. Following upon its development in 1996, many successive modifications and applications have been developed. Perhaps the most important is the development of the thick gas electron multiplier (THGEM) [8–10], which uses sub mm to mm sized insulator thickness while the standard GEM uses 50 μm insulator thickness. The hole diameter is usually scaled by a similar factor. Despite the increased hole diameter and insulator thickness, THGEMs have been shown to have similar or higher gain when compared to standard GEMs. Relevant to microdosimetry is that low-pressure operations (1–10 Torr) of THGEMs,

* Corresponding author. Tel.: +1 905 525 9140x24499; fax: +1 905 522 5982.
E-mail address: hanua@mcmaster.ca (A. Hanu).

0168-9002/$ - see front matter © 2010 Elsevier B.V. All rights reserved.
doi:10.1016/j.nima.2010.07.033

where the simulation size is comparable to the size of a DNA molecule, has been shown to produce gains of the order of 10^4–10^6 [11]. Furthermore, the fabrication of THGEM foils is much easier since the holes can be drilled mechanically while standard GEM holes are fabricated using various chemical or laser etching techniques [12,13].

Although the main application of standard GEMs and THGEMs has been imaging, gaseous photomultiplier and particle detection in high-energy physics [14–17], a THGEM based microdosimetric detector can be designed using the proper tissue-equivalent filling gas and wall material. Furthermore, a 2-D microdosimetry system can be fabricated without difficulty. Since 2008, we have developed a prototype THGEM microdosimetric detector [18] and investigated its signal performance. The successful results prompted further research in our THGEM prototype.

As shown in Fig. 1, the prototype design has a cross-sectional area of 5×5 cm^2 and houses a right cylindrical sensitive volume with a 5 mm diameter and 5 mm height. The gaseous sensitive volume is filled with propane-based tissue equivalent gas, which is composed of 55% C_3H_8, 39.5% CO_2 and 5.5% N_2 [19,20]. The pressure of the gas was set to 166.87 Torr at a temperature of 293.15 K, which results in gas density of 4.0×10^{-4} g cm^{-3}, effectively simulating the energy loss pattern in 2 μm of unit density tissue. In order to satisfy tissue equivalence in the wall material, A-150 conducting plastic was used as the cathode while Rexolite was used as the insulating material. The prototype THGEM structure is made from 0.1 mm thick copper coated G10/FR4 fiberglass epoxy insulator perforated using a mechanical drill with a 0.35 mm diameter. At a THGEM bias potential of 709 V, the pulse height of the prototype detector is similar to a standard TEPC [18], which proves that the avalanche gain is comparable. After multiplication, the electrons produced are collected by a common copper anode of 5 mm diameter.

As a microdosimetric detector, the THGEM detector must have responses as close as possible to those of soft tissue when exposed to an identical radiation field. Simulating the THGEM response is crucial in determining the feasibility of the detector for microdosimetry. Although a similar test can be conducted experimentally, an accurate detector model and simulation environment will provide a platform for testing various configurations, which cannot quickly and efficiently be studied experimentally. Moreover, a simulation allows for unraveling the contribution of the various detector components to the energy deposition, something which cannot be easily inferred in an experiment.

In this study, we simulate the microdosimetric response of the prototype THGEM detector to neutrons using the Geant4 [21] general purpose Monte Carlo code. The response patterns for various neutron energies were compared to reported experimental results from a standard TEPC detector. The angular response of the THGEM detector was simulated by varying the neutron incidence angle and as a result the original design showed a significant angular dependence for the neutron energy region above 100 keV. To overcome this problem, a modified detector design was created and its simulation was conducted.

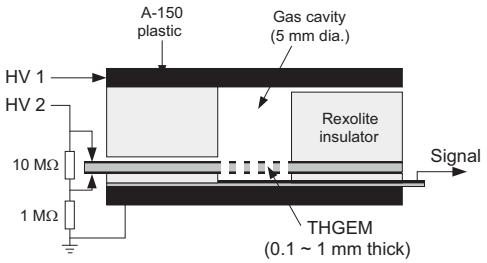

Fig. 1. The McMaster prototype THGEM microdosimetric detector assembly [18].

2. Monte Carlo simulation

In all cases, the Monte Carlo simulations were performed using Geant4 version 9.0 on a dedicated linux based cluster system readily available from Sharcnet [22]. The neutron-data library installed was G4NDL version 3.13, which is generated from the ENDF/B-VI [23] neutron cross-section library. The package installed to deal with photons, electrons and positrons was G4EMLOW version 4.3.

In Geant4, particles are transported according to the interactions specified in the physics list. Used in all simulations was the standard QGSP_BERT physics list, readily available in Geant4. During tracking, particles lose energy by the generation of secondary particles down to the energy corresponding to a cutoff value. In Geant4, the cutoff values for the production of secondary particles by electrons, positrons and photons are given in terms of a cut in range. With the cut in range specified, Geant4 calculates the corresponding energy, for all materials, at which the production of secondary particles stops. Following this, charged particles are tracked down to zero energy using the continuous slowing down approximation. For photons with an energy below the cutoff, all remaining energy is deposited locally. In this simulation, the default cut range of 1 mm was used for all materials.

For neutrons, the physics list defines the following processes G4Decay, G4UHadronElasticProcess, G4NeutronInelasticProcess, G4HadronFissionProcess and G4HadronCaptureProcess, which deal with the decay of unstable particles, elastic scattering, inelastic scattering, neutron induced fission and neutron capture interactions, respectively. Of interest are also the interactions of protons, alpha particles and other heavy ions. For alpha particles and other generic ions, the ionization process was handled using G4ionIonization process, which uses the G4BragglonModel to deal with energy loss and delta-electron production by heavy ions using the ICRU Report 49 [24] data. Similarly, proton stopping power data comes from ICRU Report 49 and the ionization process is handled using the G4hIonization with the G4BraggModel.

The detector geometry model employed in the simulation is shown in Fig. 2. Since the prototype detector was designed to be expanded to a two-dimensional array of sensitive volumes in the future, it features a larger cross-sectional area. Given that the intent of the Monte Carlo simulation is to study the response of a single sensitive volume, the width and length of the wall materials were set to have equal thicknesses (2 mm) of tissue equivalent material surrounding the sensitive volume. This thickness is sufficient for meeting the charged particle equilibrium condition while maintaining approximately equal neutron attenuation in all directions. The A-150 plastic layer was created from a 9×9 mm^2 slab, with a thickness of 2 mm. The THGEM was created using an insulator thickness of 0.6 mm with a hole diameter of 0.6 mm and a pitch of 1.2 mm. The THGEM copper layers were approximated to have a thickness of 50 μm. The prototype detector has flow channels in the Rexolite insulator for gas pumping and filling; however, these channels are not required in the simulation model.

With the general dimensions of the THGEM defined, the virtual detector model was created using the basic geometrical shapes offered by Geant4. In the model, the THGEM holes were created by making an array of cylinders representing the position of the holes and intersecting them with the insulator and conductor

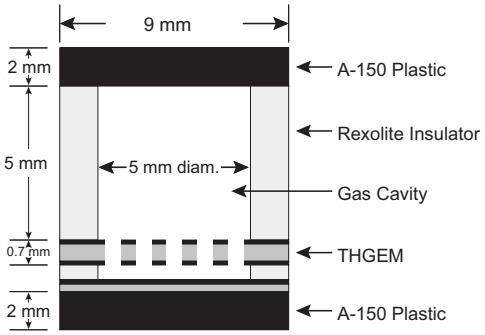

Fig. 2. The detector geometry employed for the response simulation.

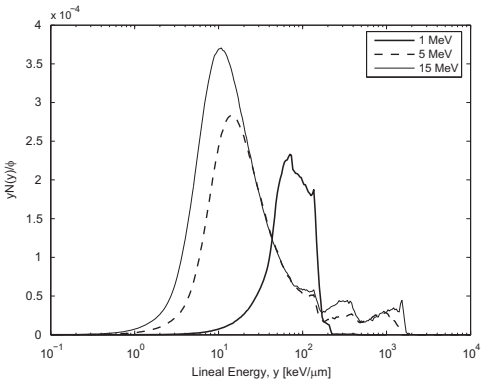

Fig. 3. A comparison of the simulated microdosimetric responses of the THGEM to various mono-energetic neutron beams.

layers. An algorithm was coded to allow the insulator thickness, pitch and hole size to be changed without having to manually recalculate the position of the holes.

Once the detector model was defined, the next step was to write the radiation source term. A planar neutron beam, with a 6 mm radius, was positioned at 10 cm from the top A-150 surface. The source position was sampled uniformly and the direction vector was fixed to normal incidence.

Since the THGEM detector measures the energy deposited in the gaseous sensitive volume for each interaction, the relevant information required from the simulation is the energy deposited in the sensitive volume per incident neutron. A tally was coded to create an output file reporting the energy deposited in the sensitive volume for each incident particle history. In order to keep computational times to a minimum, only for those histories which had a non-zero energy deposition, was the information recorded. A typical computation time of 3–4 days was required to get a 0.1% level statistical uncertainty in deposited energy.

In order to create and analyze the microdosimetric spectrum from the simulation results a data analysis code was written. The code converts the deposited energy to the lineal energy (y), a fundamental microdosimetric quantity, which is defined as the energy deposited in a volume by a single event divided by the mean chord length in that volume. For a 2 μm spherical or cylindrical tissue, the mean chord length is 1.33 μm. Subsequently, the lineal energy is subdivided into logarithmic bins created by evenly dividing a decade into 60 bins. The number of logarithmic bins was chosen in order to give sufficient smoothing of data while keeping the statistical fluctuation in each bin low. Following the redistribution of lineal energy, a semi-log plot is created where the ordinate is multiplied by y such that the area under the curve between two values of y is proportional to the fraction of dose in that region.

3. Results and discussion

3.1. Energy dependence of the THGEM detector response

To investigate the energy dependence of the microdosimetric response of the THGEM detector for neutrons, the energy deposition pattern was simulated for a mono-energetic neutron beam. The incident angle was fixed at zero degrees and the neutron energy was varied in a wide region ranging from 10 keV to 15 MeV.

Fig. 3 shows the simulated THGEM microdosimetric spectra for three different neutron energies. The units on the ordinate are $yN(y)$, which are normalized by the incident neutron fluence ϕ. Conventionally, a microdosimetric spectrum is plotted with a normalization of the total integration of unity. However, since in this study an absolute comparison between microdosimetric spectra is vital, the spectral data was left without further normalization. Hence, the integration of the dose spectrum curve is proportional to the total neutron dose. The simulated spectra in the figure were compared to the corresponding experimental results from a standard ½-inch TEPC in Ref. [1].

Overall, the patterns of the simulated microdosimetric spectra agree well with the experimental results. As expected, the predominant interaction is the elastic scattering of fast neutrons on hydrogen nuclei resulting in a proton peak as the most prominent feature in the plot. Synonymous with the proton peak is a sharp cutoff, known as the proton edge, which is characteristic of the maximum energy transfer by a recoil proton. The proton edge occurs when the recoil proton range is just equal to the diameter of the cavity being traversed. For a 2 μm simulation size, a proton edge with a lineal energy of 136 keV/μm is expected and is a very distinct feature of fast neutron microdosimetry spectra. As shown in Fig. 3, all three neutron energies result in a proton edge in exactly the same location, 135.8 keV/μm, which is consistent with both the theoretical expectation and experimental data. Above the proton edge, an alpha peak is observed due to alpha particles generated in (n,α) reactions. Considering the elemental composition of both the gas and surrounding wall material, the most probable reactions are ^{12}C(n,α), ^{14}N(n,α) and ^{16}O(n,α), which have very similar interaction cross-sections around the neutron energy used in the simulation. The threshold energies for these reactions are 6.18, 0.1649 and 2.355 MeV, respectively. This indicates that for energies below 2.355 MeV, the alpha peak is a result of the ^{14}N(n,α) reaction. Above this, the alpha component becomes significant due to increased contribution from the other reactions.

As shown in Fig. 3, an alpha edge is seen at 368 keV/μm, which corresponds to the maximum energy transfer of an alpha particle in the gas, and whose position agrees quite well with the expected value of 360 keV/μm. For lineal energies beyond the alpha edge, events from heavy recoil ions of carbon, nitrogen and hydrogen are observed. However, due to the rather similar stopping powers, the individual events from each ion cannot be resolved without further calculations. Overall, the peak locations due to the various interactions are consistent with both theoretical expectations and experimental data. A small discrepancy was identified in the

alpha peak where the simulated peak height is slightly underestimated compared to the reported experimental data for two neutron energies (5 and 15 MeV).

In order to validate the accuracy of the microdosimetric simulation with regard to the total neutron dose, each simulated spectrum was integrated and then multiplied with an appropriate constant, so that the neutron dose was obtained. Fig. 4 shows the plot of neutron doses obtained from the simulated spectra as a function of the neutron energy. As mentioned, the dose values were normalized by the incident neutron fluence. The corresponding reference values (solid line) in the figure are the recently evaluated neutron fluence-to-kerma conversion coefficient data [20] for TE-propane gas. Overall, the two data sets show a consistent pattern of the energy dependence. It is evident that the neutron doses simulated for the THGEM detector are lower than the evaluated kerma coefficients. The discrepancy between the two data sets is 20.5% on average and 47% maximum.

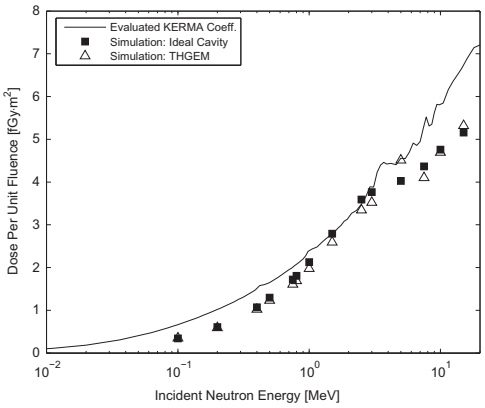

Fig. 4. A comparison between the simulated dose and the evaluated [20] neutron kerma coefficients for TE-propane. Triangles and squares represent the simulated dose per neutron fluence for the THGEM detector and an ideal spherical cavity, respectively.

To figure out whether this systematic discrepancy is caused by the fundamental limitation in the design of the THGEM microdosimetric detector or the inaccuracy in the Geant4 simulation process itself, another set of simulations was carried out for an ideal microdosimetric detector. The geometry of the ideal detector is a spherical cavity created from A-150 with a 15.4 mm diameter. The inside contains a spherical volume with a 12.7 mm diameter composed of TE-propane at a pressure of 65.70 Torr in order to simulate 2 μm of unit density tissue. The radiation source term was a planar neutron source, with an 8 mm radius, positioned 10 cm away from the centre of the sphere. Considering that the ideal detector satisfies charged particle equilibrium, the neutron kerma and dose should be identical. However, as shown in Fig. 4, the neutron dose for the simulated ideal detector is still lower than the kerma coefficients. On average, the ideal detector dose is about 17.8% lower than the experimental kerma coefficient while the average difference between the THGEM and the ½-inch cavity is less than 5%. The close agreement between the THGEM and the ideal detector indicates that there is little bias in the microdosimetric response of the THGEM detector.

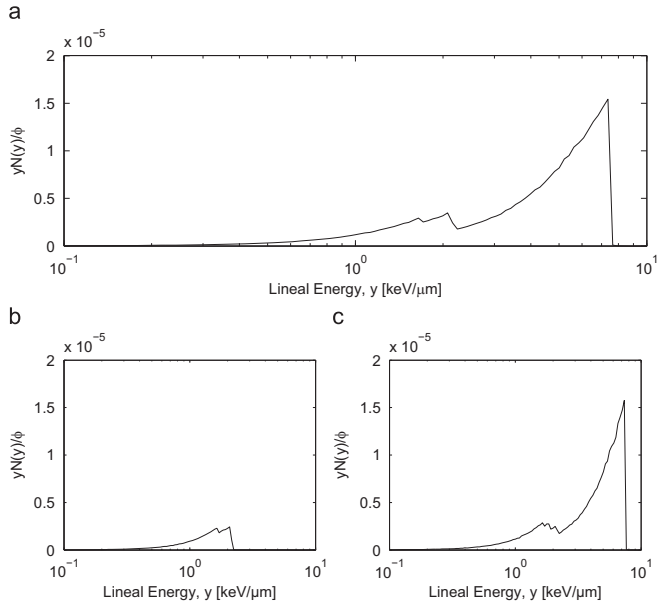

Fig. 5. A plot showing the microdosimetry spectrum of 10 keV neutrons for various gas compositions presented in percent atomic composition of the total mass. (a) TE-propane (10.27% ^{1}H, 3.5% ^{14}N, 56.89% ^{12}C, 29.34% ^{16}O), (b) the hydrogen component removed and redistributed into carbon component (3.5% ^{14}N, 67.16% ^{12}C, 29.34% ^{16}O), (c) the carbon composition halved, and the difference added onto nitrogen (10.27% ^{1}H, 31.94% ^{14}N, 28.45% ^{12}C, 29.34% ^{16}O).

As a subsequent investigation, the microdosimetric response for 10 keV neutrons was analyzed in terms of its various components and the interactions responsible. At this energy, the dominant mode of interaction is elastic scattering and should therefore produce a relatively simple spectrum. The resultant spectrum can therefore be used to verify that the expected interactions are indeed the ones contributing to the dose in the sensitive volume. The wall contribution, for 10 keV neutrons, is quite low ($\ll 1\%$) since the range of even the lightest product (^{1}H) of neutron interactions is about 0.2 μm in A-150. As a result, the spectrum produced is mainly the result of interactions produced in the gas cavity itself. Thus, by systematically changing the elemental composition of the gas, the mode of interaction can be determined by comparing the relative change in peak height to the change in elemental composition.

In order to find out the origin of each peak, the gas composition was varied while the location and height of the peaks were analyzed. In Fig. 5 (a), the spectrum shows a standard non-modified gas response with three distinct peaks located at about 1.64, 2.07 and 7.35 keV/μm. The source of all these peaks can be inferred based on kinematics and neutron interaction cross-sections for the constituent elements in the gas material. The TE-propane used is mainly composed of four elements, of which ^{1}H has the biggest neutron cross-section at 10 keV. In the case of neutron elastic scattering, the maximum recoil energy and thus the maximum lineal energy, can be calculated for a collision between a neutron with a given incident energy and a target nucleus. As such, one expects the maximum lineal energies of the four constituents of TE-propane (^{1}H, ^{12}C, ^{14}N and ^{16}O), to be 7.50, 2.13, 1.86 and 1.66 keV/μm, respectively. Thus, the big peak in Fig. 5(a) is the result of elastic neutron scattering on ^{1}H. The spectrum in Fig. 5(b), is the response of neutrons on a modified gas composition with the hydrogen component removed. The large peak at 7.35 keV/μm is no longer present, which indicates its presence is a result of the elastic neutron scattering on ^{1}H. Fig. 5(c) shows the response of neutrons on a gas with the carbon composition halved and redistributed to nitrogen. The results indicate a new peak at 1.86 keV/μm, which is due to the increased nitrogen contribution. As expected from interaction cross-sections, the spectrum produced in the simulation indicates that the dominant interaction in this energy range is indeed neutron elastic scattering on the elemental constituents of the sensing gas.

3.2. Angular dependence of the THGEM detector response

The angular dependence of the response is another important characteristic of a microdosimetric detector. Ideally, the response of a dosimetric detector should have an angle-independent response.

To investigate the angular response of the THGEM detector, the direction vector of the incident neutron beam was varied in the angular range 0–180°. The zero angle was defined when the beam hits the THGEM perpendicular to the top A-150 surface. The beam diameter and uniform sampling was kept the same for each angle.

Fig. 6 shows the neutron dose variation as a function of the incident angle of the neutron beam. For 100 keV neutrons, the neutron dose is nearly independent of angle while it decreases by a factor of two for 1 MeV neutrons. The angular response at 1.0 MeV is undesirable since the measured neutron dose will significantly vary depending on the incident direction of the neutron beam. Since the different angular dependences observed in Fig. 6 imply different contributions of the wall interactions, additional simulations were carried out for the geometry without the wall materials. Table 1 shows a comparison of the angular dependence between with the walls and without the walls. For 0.1 MeV, there is little discrepancy between the neutron doses with and without the walls for all angles,

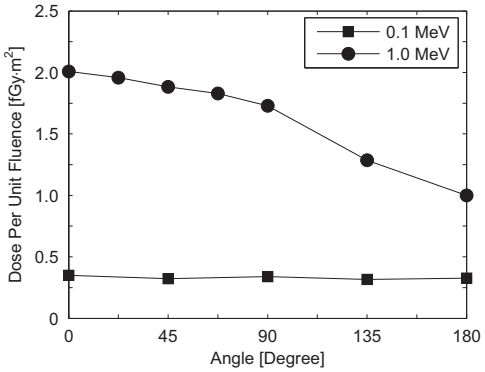

Fig. 6. Neutron dose as a function of the incident angle of the neutron beam.

Table 1
Comparison of the neutron dose between with the walls and without the walls as a function of incident neutron angle.

Angle (deg.)	Dose per fluence (fGy m^2)			
	0.1 MeV		1.0 MeV	
	With wall	Without wall	With wall	Without wall
0	0.3489	0.3609	2.0083	0.3678
45	0.3231	0.3609	1.8831	0.3678
90	0.3385	0.3603	1.7288	0.3685
135	0.3154	0.3632	1.2848	0.3712
180	0.3269	0.3611	0.9993	0.3678

which indicates that the wall contribution to the sensitive volume dose is negligible. In contrast, for 1.0 MeV, the neutron dose with the walls is significantly higher than the dose without the walls for all angles, which indicates that the wall interactions mainly contribute to the sensitive volume dose. Given that for large incident angles only the recoil particles from the rexolite wall can reach the sensitive volume, it is unavoidable to have an inferior angular response in this energy region with the current structure of the THGEM detector.

To overcome the severe angular dependence problem, the dose from backside interactions needed to be increased. Since the charged particles (mostly protons) were being obstructed by the THGEM, an additional tissue-equivalent wall is needed on top of the THGEM as shown in Fig. 7. As such, the charged particles produced in the modified layer, from the incident neutrons, are able to pass into the sensitive volume. The 2 mm thick modifier, composed of A-150, has holes drilled in the same geometric arrangement as the THGEM.

Fig. 8 shows the comparison of the angular responses between the original detector and the modified detector. In order to show the angular response more clearly, the neutron dose for each angle is normalized by the dose at the zero angle. The results in Fig. 8 indicate the A-150 modifier had the effect of increasing the dose for larger angles while maintaining the lower angle doses constant. The preliminary results were successful in keeping the relative dose variation within 10% as the incident angle increases.

4. Conclusion

A THGEM detector model was simulated for its application in microdosimetry using the Geant4 Monte Carlo code. The energy

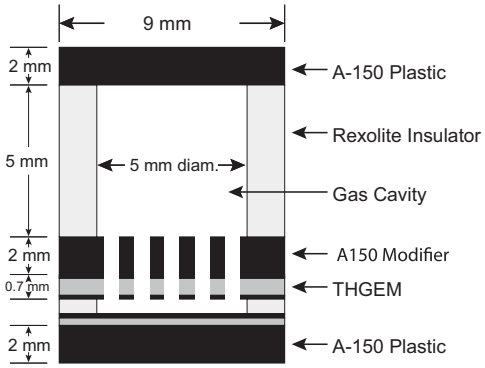

Fig. 7. The modified detector geometry used to enhance the angular response.

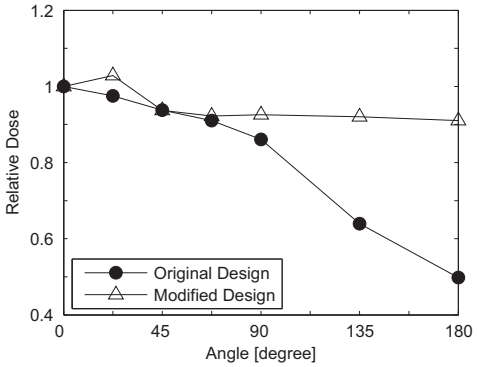

Fig. 8. A comparison of the angular response between the original and the modified THGEM designs for a 1.0 MeV incident neutron beam.

deposition pattern of various mono-energetic neutron beams was analyzed and compared with experimental results with reasonable agreements.

For quantitative validation, the neutron doses from the THGEM and the ideal microdosimetric detectors were compared at various neutron energies, which showed a discrepancy of 5%. The close agreement between the THGEM and the ideal microdosimetric detector indicates that there is a negligible difference in the THGEM energy response. On the other hand, when the THGEM neutron dose was compared to the evaluated neutron kerma coefficients, the discrepancy between the two data sets was 18% on average, which requires a further study to ascertain whether the discrepancy was caused by the inaccuracy in simulation algorithm or interaction data.

In the simulation of the angular dependence of the THGEM response, the angular dependence was negligible for 0.1 MeV while a notable angular dependence was observed for 1.0 MeV. To solve this serious problem, a modified THGEM detector design was created by adding a tissue-equivalent plastic layer on top of the THGEM. The simulation result for the modified detector showed a considerable improvement in the angular response. Further experimental tests need to be done to prove the simulation results.

To extend the simulation to the thermal neutron energy, the $^{14}N(n,p)$ reaction needs to be included in future. The detector response to gamma-ray is also being investigated.

References

[1] A. Waker, Radiat. Prot. Dosim. 61 (1995) 297.
[2] H. Schuhmacher, Radiat. Prot. Dosim. 44 (1992) 199.
[3] G.M. Spirou, S.H. Byun, W.V. Prestwich, IEEE Trans. Nucl. Sci. NS-55 (2008) 2621.
[4] D. Moro, P. Colautti, G. Gualdrini, M. Masi, V. Conte, L. De Nardo, G. Tornielli, Radiat. Prot. Dosim. 122 (2006) 396.
[5] J. Burmeister, C. Kota, R.L. Maughan, A.J. Waker, Radiat. Phys. Med. Biol. 47 (2002) 1633.
[6] J. Burmeister, C. Kota, R.L. Maughan, A.J. Waker, Med. Phys. 28 (2001) 1911.
[7] F. Sauli, Nucl. Instr. and Meth. A 386 (1997) 531.
[8] V. Peskov, et al., IEEE Trans. Nucl. Sci. NS-54 (2007) 1784.
[9] C. Shalem, R. Chechik, A. Breskin, K. Michaeli, Nucl. Instr. and Meth. A 558 (2006) 475.
[10] L. Periale, et al., Nucl. Instr. and Meth. A 478 (2002) 377.
[11] R. Chechik, A. Breskin, C. Shalem, D. Mörmann, Nucl. Instr. and Meth. 535 (2004) 303.
[12] F. Simon, et al., IEEE Trans. Nucl. Sci. NS-54 (2007) 2646.
[13] M. Inuzuka, H. Hamagaki, K. Ozawa, T. Tamagawa, T. Isobe, Nucl. Instr. and Meth. A 525 (2004) 529.
[14] G.P. Guedes, et al., Nucl. Instr. and Meth. A 513 (2003) 473.
[15] J. Maia, D. Mörmann, A. Breskin, R. Chechik, J.F.C.A. Veloso, J.M.F. dos Santos, Nucl. Instr. and Meth. A 580 (2007) 373.
[16] R. Chechik, A. Breskin, C. Shalem, Nucl. Instr. and Meth. A 553 (2005) 35.
[17] M. Cortesi, et al., Nucl. Instr. and Meth. A 572 (2007) 175.
[18] S.H. Byun, G.M. Spirou, A. Hanu, W.V. Prestwich, A.J. Waker, IEEE Trans. Nucl. Sci. NS-56 (2009) 1113.
[19] D. Srdoč, Radiat. Res. 43 (1970) 302.
[20] M.B. Chadwick, et al., Med. Phys. 26 (1999) 974.
[21] S. Agostinelli, et al., Nucl. Instr. and Meth. A 506 (2003) 250.
[22] Shared Hierarchical Academic Research Computing Network (SHARCNET), 〈http://www.sharcnet.ca〉.
[23] ENDF/B-VI, Report BNL-NCS-17541, National Nuclear Data Center, Brookhaven National Laboratory, USA, 1991.
[24] ICRU Report 49, Stopping Powers and Ranges for Protons and Alpha Particles, International Commission of Radiation Units and Measurements, Bethesda, Maryland, 1993.

A.6 Geant4 Microdosimetry Code

The following code, written in C++, implements the Geant4 microdosimetry simulation presented in the previous section. To generate the geometry of the THGEM detector, simple boolean operations are performed on basic geometric objects. The geometry code is provided in the `DetectorConstruction.cc` module. To modify the geometry during simulation, the `DetectorConstructionMessenger.cc` is implemented. During an interaction with the detector, energy information is extracted using the `RunAction.cc`, `EventAction.cc`, and `SteppingAction.cc` modules. The number of particles, type, and energy is controlled from the input macro file `run.mac` and passed into simulation through the `PrimaryGeneratorAction.cc` module.

The code provided here implements the Geant4 THGEM simulation in it's entirety.

THGEM.cc

```
// ********************************************************************
// A simulation of a single 0.5 mm Microdosimetric cavity with a THGEM
// detector.
// Simulation by: Andrei Hanu at McMaster University
// ********************************************************************

#include "DetectorConstruction.hh"
#include "PrimaryGeneratorAction.hh"
#include "RunAction.hh"
#include "EventAction.hh"
#include "SteppingAction.hh"
#include "G4RunManager.hh"
#include "QGSP_BERT_HP.hh"
#include "QGSP_BERT.hh"
#include "QGSP.hh"
#include "G4UImanager.hh"
#include "G4UIterminal.hh"

#ifdef G4UI_USE_TCSH
#include "G4UItcsh.hh"
#endif
#ifdef G4UI_USE_XM
#include "G4UIXm.hh"
#endif

#ifdef G4VIS_USE
#include "G4VisExecutive.hh"
#endif

int main(int argc,char** argv) {

  // Choose the Random engine
  CLHEP::HepRandom::setTheEngine(new CLHEP::RanecuEngine);

  // Run manager
  G4RunManager * runManager = new G4RunManager;

  // Mandatory initialization classes
  DetectorConstruction* detector = new DetectorConstruction;
  runManager->SetUserInitialization(detector);

  // Physics List
  QGSP* thePL = new QGSP;
  runManager->SetUserInitialization(thePL);

  // Custom Physics List
  //runManager->SetUserInitialization(new PhysicsList);

#ifdef G4VIS_USE
  // Visualization manager
  //
  G4VisManager* visManager = new G4VisExecutive;
  visManager->Initialize();
#endif

  // User action classes
  PrimaryGeneratorAction* primary = new PrimaryGeneratorAction();
  runManager->SetUserAction(primary);

  // User defined run action
  RunAction* run_action = new RunAction(detector, primary);
  runManager->SetUserAction(run_action);

  // User defined event action
  EventAction* event_action = new EventAction(detector,run_action);
  runManager->SetUserAction(event_action);
  //
  G4UserSteppingAction* stepping_action = new SteppingAction(detector,event_action);
  runManager->SetUserAction(stepping_action);

  // Initialize G4 kernel
  runManager->Initialize();

  G4UImanager* UI = G4UImanager::GetUIpointer();

  // Batch Commands
   G4UIsession * session = 0;
if(argc==1) // Define (G)UI terminal for interactive mode
  {
    // G4UIterminal is a (dumb) terminal
```

```
    //
    G4UIsession * session = 0;
#ifdef G4UI_USE_TCSH
      session = new G4UIterminal(new G4UItcsh);
#else
      session = new G4UIterminal();
#endif
    UI->ApplyCommand("/control/execute run.mac");
    session->SessionStart();
    delete session;
  }
  else // Batch mode
  {
    G4String command = "/control/execute ";
    G4String fileName = argv[1];
    UI->ApplyCommand(command+fileName);
  }

  // Job termination
#ifdef G4VIS_USE
  delete visManager;
#endif

  delete runManager;

  return 0;
}
```

DetectorConstruction.cc

```
// ********************************************************************
// The following module creates the geometrical volumes of the THGEM
// microdosimetric detector.
// Simulation by: Andrei Hanu at McMaster University
// ********************************************************************
#include "DetectorConstruction.hh"
#include "DetectorConstructionMessenger.hh"
#include "G4Box.hh"
#include "G4Colour.hh"
#include "G4LogicalVolume.hh"
#include "G4Material.hh"
// Include G4NistManager
#include "G4NistManager.hh"
#include "G4PVParameterised.hh"
#include "G4PVPlacement.hh"
#include "G4RunManager.hh"
#include "G4Tubs.hh"
#include "G4Sphere.hh"
#include "G4Cons.hh"
#include "G4VisAttributes.hh"
// Include Boolean Operations
#include "G4UnionSolid.hh"
#include "G4SubtractionSolid.hh"
#include "G4IntersectionSolid.hh"
// Scoring Components
#include "G4VSensitiveDetector.hh"
#include "G4SDManager.hh"

DetectorConstruction::DetectorConstruction():fpWorldLogical(0),fpWorldPhysical(0)
{
   // Default Parameters
   A150_Top_Thickness = 2.00*mm;
   A150_Bottom_Thickness = 2.00*mm;
   A150_Extra_Modifier = 0.*mm;
   SignalPad_Thickness = 0.2*mm;
   LowerInsulator_Thickness = 0.2*mm;
   SVDiameter = 5.0*mm; // Right Cylinder Approach (ie. Diameter=Height)
   GEM_Insulator_Thickness = 0.6*mm;
   GEM_Conductor_Thickness = 0.05*mm;
   GEM_Hole_Diameter = 0.6*mm;
   GEM_Hole_Pitch = 2*GEM_Hole_Diameter;
   GEM_Length = 9.00*mm;
   GEM_Width = 9.00*mm;
   GEM_Height = A150_Top_Thickness + SVDiameter + A150_Extra_Modifier + GEM_Conductor_Thickness*2 + GEM_Insulator_Thickness +
       LowerInsulator_Thickness + SignalPad_Thickness + A150_Bottom_Thickness;
   DetectorAngle = 0*deg;

   // materials
   DefineMaterials();
```

```
   // Create Interactive Commands For Detector
   detectorMessenger = new DetectorConstructionMessenger(this);
}

DetectorConstruction::~DetectorConstruction()
{
delete detectorMessenger;
}

G4VPhysicalVolume* DetectorConstruction::Construct()
{
  // Geometry Definition
  return SetupGeometry();
}

void DetectorConstruction::DefineMaterials()
{
  G4String symbol;
  G4double a, z, density;
  G4int ncomponents, natoms;
  G4double fractionmass;

  G4NistManager* manager = G4NistManager::Instance();

  // Define Elements
  G4Element* H = manager->FindOrBuildElement(1);
  G4Element* B = manager->FindOrBuildElement(5);
  G4Element* C = manager->FindOrBuildElement(6);
  G4Element* N = manager->FindOrBuildElement(7);
  G4Element* O = manager->FindOrBuildElement(8);
  G4Element* F = manager->FindOrBuildElement(9);
  G4Element* Na = manager->FindOrBuildElement(11);
  G4Element* Mg = manager->FindOrBuildElement(12);
  G4Element* Al = manager->FindOrBuildElement(13);
  G4Element* Si = manager->FindOrBuildElement(14);
  G4Element* K = manager->FindOrBuildElement(19);
  G4Element* Ca = manager->FindOrBuildElement(20);
  G4Element* Ti = manager->FindOrBuildElement(22);
  G4Element* Fe = manager->FindOrBuildElement(26);
  G4Element* Cu = manager->FindOrBuildElement(29);

  // Define A150(Plastic)
  G4Material* A150 = new G4Material("A150Plastic", density= 1.138*g/cm3, ncomponents=6);
  A150->AddElement(H,fractionmass=0.102);
  A150->AddElement(C,fractionmass=0.776);
  A150->AddElement(N,fractionmass=0.035);
  A150->AddElement(O,fractionmass=0.052);
  A150->AddElement(F,fractionmass=0.017);
  A150->AddElement(Ca,fractionmass=0.018);

  // Define Rexolite (a.k.a. Polystyrene)
  G4Material* Rexolite = new G4Material("Rexolite", density= 1.05*g/cm3, ncomponents=2);
  Rexolite->AddElement(H,fractionmass=0.077418);
  Rexolite->AddElement(C,fractionmass=0.922582);

  // Define SiO2
  G4Material* SiO2 = new G4Material("SiO2", density= 2.64*g/cm3, ncomponents=2);
  SiO2->AddElement(Si,natoms=1);
  SiO2->AddElement(O,natoms=2);

  // Define CaO
  G4Material* CaO = new G4Material("CaO", density= 3.34*g/cm3, ncomponents=2);
  CaO->AddElement(Ca,natoms=1);
  CaO->AddElement(O,natoms=1);

  // Define Al2O3
  G4Material* Al2O3 = new G4Material("Al2O3", density= 3.97*g/cm3, ncomponents=2);
  Al2O3->AddElement(Al,natoms=2);
  Al2O3->AddElement(O,natoms=3);

  // Define MgO
  G4Material* MgO = new G4Material("MgO", density= 3.60*g/cm3, ncomponents=2);
  MgO->AddElement(Mg,natoms=1);
  MgO->AddElement(O,natoms=1);

  // Define B2O3
  G4Material* B2O3 = new G4Material("B2O3", density= 2.55*g/cm3, ncomponents=2);
  B2O3->AddElement(B,natoms=2);
  B2O3->AddElement(O,natoms=3);

  // Define TiO2
```

```
G4Material* TiO2 = new G4Material("TiO2", density= 4.230*g/cm3, ncomponents=2);
TiO2->AddElement(Ti,natoms=1);
TiO2->AddElement(O,natoms=2);

// Define Na2O
G4Material* Na2O = new G4Material("Na2O", density= 2.270*g/cm3, ncomponents=2);
Na2O->AddElement(Na,natoms=2);
Na2O->AddElement(O,natoms=1);

// Define K2O
G4Material* K2O = new G4Material("K2O", density= 2.350*g/cm3, ncomponents=2);
K2O->AddElement(K,natoms=2);
K2O->AddElement(O,natoms=1);

// Define Fe2O3
G4Material* Fe2O3 = new G4Material("Fe2O3", density= 5.250*g/cm3, ncomponents=2);
Fe2O3->AddElement(Fe,natoms=2);
Fe2O3->AddElement(O,natoms=3);

// Define F2
G4Material* F2 = new G4Material("F2", density= 0.001580*g/cm3, ncomponents=1);
F2->AddElement(F,natoms=2);

// Define E-Glass Fiberglass
G4Material* E_Glass_Fiberglass = new G4Material("E_Glass_Fiberglass", density= 2.61*g/cm3, ncomponents=10);
E_Glass_Fiberglass->AddMaterial(SiO2,fractionmass = 0.54);
E_Glass_Fiberglass->AddMaterial(CaO,fractionmass = 0.19);
E_Glass_Fiberglass->AddMaterial(Al2O3,fractionmass = 0.13);
E_Glass_Fiberglass->AddMaterial(MgO,fractionmass = 0.025);
E_Glass_Fiberglass->AddMaterial(B2O3,fractionmass = 0.075);
E_Glass_Fiberglass->AddMaterial(TiO2,fractionmass = 0.008);
E_Glass_Fiberglass->AddMaterial(Na2O,fractionmass = 0.01);
E_Glass_Fiberglass->AddMaterial(K2O,fractionmass = 0.01);
E_Glass_Fiberglass->AddMaterial(Fe2O3,fractionmass = 0.005);
E_Glass_Fiberglass->AddMaterial(F2,fractionmass = 0.007);

// Diglycidyl Ether of Bisphenol A (C19H20O4)
G4Material* C19H20O4 = new G4Material("C19H20O4", density= 1.16*g/cm3, ncomponents=3);
C19H20O4->AddElement(C,natoms=19);
C19H20O4->AddElement(H,natoms=20);
C19H20O4->AddElement(O,natoms=4);

// 1,4-Butanediol Diglycidyl (C10H18O4)
G4Material* C10H18O4 = new G4Material("C10H18O4", density= 1.10*g/cm3, ncomponents=3);
C10H18O4->AddElement(C,natoms=10);
C10H18O4->AddElement(H,natoms=18);
C10H18O4->AddElement(O,natoms=4);

// 1,4-Hexanediamine 2,2,4-trimethyl (C9H22N2)
G4Material* C9H22N2 = new G4Material("C9H22N2", density= 0.865*g/cm3, ncomponents=3);
C9H22N2->AddElement(C,natoms=9);
C9H22N2->AddElement(H,natoms=22);
C9H22N2->AddElement(N,natoms=2);

// Define Epoxy Resin Epotek 301-1
G4Material* Epoxy_Resin_Epotek_301_1 = new G4Material("Epoxy_Resin_Epotek_301_1", density= 1.19*g/cm3, ncomponents=3);
Epoxy_Resin_Epotek_301_1->AddMaterial(C19H20O4,fractionmass = 0.56);
Epoxy_Resin_Epotek_301_1->AddMaterial(C10H18O4,fractionmass = 0.24);
Epoxy_Resin_Epotek_301_1->AddMaterial(C9H22N2,fractionmass = 0.20);

// Define G10-FR4 Insulator
G4Material* G10_FR4 = new G4Material("G10_FR4", density= 1.80*g/cm3, ncomponents=2);
G10_FR4->AddMaterial(E_Glass_Fiberglass,fractionmass = 0.60);
G10_FR4->AddMaterial(Epoxy_Resin_Epotek_301_1,fractionmass = 0.40);

// Define Copper Pad
G4Material* Copper = new G4Material("Copper", density= 8.96*g/cm3, ncomponents=1);
Copper->AddElement(Cu,fractionmass = 1.0);

// Define TEP Gas
G4double temperature = 293.15*kelvin;
G4double pressure = 0.21960092*atmosphere;
G4double TEPGas_density = 0.0004*g/cm3;
G4Material* TEP_Gas = new G4Material("TEPGas", TEPGas_density, ncomponents=4,kStateGas,temperature,pressure);
TEP_Gas->AddElement(H,fractionmass=0.1027);
TEP_Gas->AddElement(C,fractionmass=0.5689);
TEP_Gas->AddElement(N,fractionmass=0.035);
TEP_Gas->AddElement(O,fractionmass=0.2934);

// Define air
G4Material* air = new G4Material("Air", density= 1.290*mg/cm3, ncomponents=2);
air->AddElement(N, fractionmass=0.7);
```

```
  air->AddElement(O, fractionmass=0.3);
}

G4VPhysicalVolume* DetectorConstruction::SetupGeometry()
{
  ////////////////////////////////////////////////////////////////////////
  // G4 Starting Vector
  G4double G4PosX = 0.;
  G4double G4PosY = 0.;
  G4double G4PosZ = -10.055*cm; // Trying to Center The Sensitive Volume

  ////////////////////////////////////////////////////////////////////////
  // Grab All The Required Materials
  G4Material* a150 = G4Material::GetMaterial("A150Plastic");
  G4Material* rexolite = G4Material::GetMaterial("Rexolite");
  G4Material* copper = G4Material::GetMaterial("Copper");
  G4Material* tep_gas = G4Material::GetMaterial("TEPGas");
  G4Material* g10_fr4 = G4Material::GetMaterial("G10_FR4");
  G4Material* air = G4Material::GetMaterial("Air");

  ////////////////////////////////////////////////////////////////////////
  // Construct The World Volume
  G4Box* worldSolid = new G4Box("World_Solid", // Name
          1.5*cm, 1.5*cm, 13.0*cm); // Half lengths

  fpWorldLogical = new G4LogicalVolume(worldSolid, // Solid
                 air, // Material
                 "World_Logical"); // Name

  fpWorldPhysical = new G4PVPlacement(0, // Rotation matrix pointer
                G4ThreeVector(), // Translation vector
                fpWorldLogical, // Logical volume
                "World_Physical", // Name
                0,  // Mother volume
                false,  // Unused boolean parameter
                0);  // Copy number

  ////////////////////////////////////////////////////////////////////////
  // Geometry Details

  GEM_Height = A150_Top_Thickness + SVDiameter + A150_Extra_Modifier + GEM_Conductor_Thickness*2 + GEM_Insulator_Thickness +
      LowerInsulator_Thickness + SignalPad_Thickness + A150_Bottom_Thickness;

  ////////////////////////////////////////////////////////////////////////
  // A150 Base Plastic (Top and Bottom) Mother Volume
  G4Box* A150BaseSolid = new G4Box("A150Base_Solid", // Name
          GEM_Length/2, GEM_Width/2, GEM_Height/2); // Half lengths

  G4LogicalVolume* A150BaseLogical = new G4LogicalVolume(A150BaseSolid,
                                        a150,
                                    "A150Base_Logical");
  G4RotationMatrix* Rotation = new G4RotationMatrix();
  Rotation->rotateY(DetectorAngle); // Detector Rotational Angle
  A150BasePhysical = new G4PVPlacement(Rotation,
              G4ThreeVector(G4PosX,G4PosY,G4PosZ),
              A150BaseLogical,
              "A150Base_Physical",
                  fpWorldLogical,
              false,
              0,
              false);

  ////////////////////////////////////////////////////////////////////////
  // Signal Pad
  G4Box* SignalPadSolid = new G4Box("SignalPad_Solid", // Name
          GEM_Length/2, GEM_Width/2, SignalPad_Thickness/2); // Half lengths

  G4LogicalVolume* SignalPadLogical = new G4LogicalVolume(SignalPadSolid,
                                        copper,
                                    "SignalPad_Logical");

  G4PosZ += SignalPad_Thickness/2;
  SignalPadPhysical = new G4PVPlacement(0,
              G4ThreeVector(0,0,(A150_Bottom_Thickness+SignalPad_Thickness/2-GEM_Height/2)),
              SignalPadLogical,
              "SignalPad_Physical",
                  A150BaseLogical,
              false,
              0,
              false);
  ////////////////////////////////////////////////////////////////////////
  // Lower Insulator (Rexolite)
```

```
G4Box* LowerInsulatorSolid = new G4Box("LowerInsulator_Box", // Name
        GEM_Length/2, GEM_Width/2, LowerInsulator_Thickness/2); // Half lengths

G4LogicalVolume* LowerInsulatorLogical = new G4LogicalVolume(LowerInsulatorSolid,
                                        rexolite,
                                    "LowerInsulator_Logical");

LowerInsulatorPhysical = new G4PVPlacement(0,
           G4ThreeVector(0,0,(A150_Bottom_Thickness+SignalPad_Thickness+LowerInsulator_Thickness/2-GEM_Height/2)),
           LowerInsulatorLogical,
           "LowerInsulator_Physical",
               A150BaseLogical,
           false,
           0,
           false);

//////////////////////////////////////////////////////////////////////////
// Lower Insulator Gas Cylinder (TEP Gas)
G4VSolid* LowerInsulatorSolid_Cylinder = new
    G4Tubs("LowerInsulatorSolid_Cylinder",0.,SVDiameter/2,LowerInsulator_Thickness/2,0.,360.*deg);

G4LogicalVolume* LowerInsulator_Cylinder_Logical = new G4LogicalVolume(LowerInsulatorSolid_Cylinder,
                                        tep_gas,
                                    "LowerInsulator_Cylinder_Logical");

LowerInsulatorPhysical_Cylinder = new G4PVPlacement(0,
           G4ThreeVector(0,0,0),
           LowerInsulator_Cylinder_Logical,
           "LowerInsulatorPhysical_Cylinder",
               LowerInsulatorLogical,
           false,
           0,
           false);

//////////////////////////////////////////////////////////////////////////
// GEM

 // Starting Volumes
 G4VSolid* GEM_Hole_Cylinder = new G4Tubs("GEM_Hole_Cylinder",0.,GEM_Hole_Diameter/2,(GEM_Insulator_Thickness +
     2*GEM_Conductor_Thickness+A150_Extra_Modifier)/2,0.,360.*deg);
 G4VSolid* GEM_Insulator_Box = new G4Box("GEM_Insulator_Box", GEM_Length/2, GEM_Width/2, GEM_Insulator_Thickness/2);
 G4VSolid* GEM_Conductor_Top_Box = new G4Box("GEM_Conductor_Top_Box", GEM_Length/2, GEM_Width/2, GEM_Conductor_Thickness/2);
 G4VSolid* GEM_Conductor_Bottom_Box = new G4Box("GEM_Conductor_Bottom_Box", GEM_Length/2, GEM_Width/2, GEM_Conductor_Thickness/2);

 G4LogicalVolume* GEM_Hole_Cylinder_Logical = new G4LogicalVolume(GEM_Hole_Cylinder,
                                        tep_gas,
                                    "GEM_Hole_Cylinder_Logical");

 // Making GEM Holes
 G4int GEM_Hole_ID = 0;
 // GEM Hole Creation (Posititioning Variables)
 G4double GEM_Hole_Locx = -1*(SVDiameter/2+GEM_Hole_Diameter);
 G4double GEM_Hole_Locy = -1*(SVDiameter/2+GEM_Hole_Diameter);
 G4double GEM_Hole_Maxx = +1*(SVDiameter/2+GEM_Hole_Diameter);
 G4double GEM_Hole_Maxy = +1*(SVDiameter/2+GEM_Hole_Diameter);
 G4double GEM_Hole_Startx = GEM_Hole_Locx;
 while (GEM_Hole_Locy <= GEM_Hole_Maxy){
    GEM_Conductor_Bottom_Box = new G4SubtractionSolid("GEM_Conductor_Bottom_Box", GEM_Conductor_Bottom_Box, GEM_Hole_Cylinder,0,
        G4ThreeVector(GEM_Hole_Locx,GEM_Hole_Locy,0.));
    GEM_Conductor_Top_Box = new G4SubtractionSolid("GEM_Conductor_Top_Box", GEM_Conductor_Top_Box, GEM_Hole_Cylinder,0,
        G4ThreeVector(GEM_Hole_Locx,GEM_Hole_Locy,0.));
    GEM_Insulator_Box = new G4SubtractionSolid("GEM_Insulator_Box", GEM_Insulator_Box, GEM_Hole_Cylinder,0,
        G4ThreeVector(GEM_Hole_Locx,GEM_Hole_Locy,0.));


    // GEM Hole Placement
    new G4PVPlacement(0,
       G4ThreeVector(GEM_Hole_Locx,GEM_Hole_Locy,(A150_Bottom_Thickness + SignalPad_Thickness + LowerInsulator_Thickness +
           (GEM_Insulator_Thickness + 2*GEM_Conductor_Thickness+A150_Extra_Modifier)/2-GEM_Height/2)),
       GEM_Hole_Cylinder_Logical,
       "GEM_Hole_Cylinder_Physical",
         A150BaseLogical,
       false,
       GEM_Hole_ID,
       false);

    // Increment The Current X Position
    GEM_Hole_Locx += GEM_Hole_Pitch;
    if(GEM_Hole_Locx > GEM_Hole_Maxx){
       GEM_Hole_Locx = GEM_Hole_Startx;
       // Increase Current Y-Location
       GEM_Hole_Locy += GEM_Hole_Pitch;
```

```
   }
   GEM_Hole_ID++;
}

// Create the Lower Conductor
G4LogicalVolume* GEMConductorBottomLogical = new G4LogicalVolume(GEM_Conductor_Bottom_Box,
                                          copper,
                                    "GEMConductorBottomLogical");

GEMConductorBottomPhysical = new G4PVPlacement(0,
             G4ThreeVector(0,0,(A150_Bottom_Thickness + SignalPad_Thickness + LowerInsulator_Thickness +
                 GEM_Conductor_Thickness/2 - GEM_Height/2)),
             GEMConductorBottomLogical,
             "GEMConductorBottom_Physical",
                 A150BaseLogical,
             false,
             0,
             false);

// Create the Insulator
G4LogicalVolume* GEMInsulatorLogical = new G4LogicalVolume(GEM_Insulator_Box,
                                           g10_fr4,
                                     "GEMInsulatorLogical");

GEMInsulatorPhysical = new G4PVPlacement(0,
             G4ThreeVector(0,0,(A150_Bottom_Thickness + SignalPad_Thickness + LowerInsulator_Thickness + GEM_Conductor_Thickness
                 + GEM_Insulator_Thickness/2 - GEM_Height/2)),
             GEMInsulatorLogical,
             "GEMInsulator_Physical",
                 A150BaseLogical,
             false,
             0,
             false);

G4PosZ += GEM_Insulator_Thickness/2;

// Create the Top Conductor
G4LogicalVolume* GEMConductorTopLogical = new G4LogicalVolume(GEM_Conductor_Top_Box,
                                          copper,
                                    "GEMConductorTopLogical");

GEMConductorTopPhysical = new G4PVPlacement(0,
             G4ThreeVector(0,0,(A150_Bottom_Thickness + SignalPad_Thickness + LowerInsulator_Thickness + GEM_Conductor_Thickness
                 + GEM_Insulator_Thickness + GEM_Conductor_Thickness/2 - GEM_Height/2)),
             GEMConductorTopLogical,
             "GEMConductorTop_Physical",
                 A150BaseLogical,
             false,
             0,
             false);

// Create the Modifier
if (A150_Extra_Modifier/mm > 0.)
{
   G4VSolid* GEM_Modifier_Box = new G4Box("GEM_Modifier_Box", GEM_Length/2, GEM_Width/2, A150_Extra_Modifier/2);

   // Making GEM Holes
   G4int GEM_Hole_ID = 0;
   // GEM Hole Creation (Posititioning Variables)
   G4double GEM_Hole_Locx = -1*(SVDiameter/2+GEM_Hole_Diameter);
   G4double GEM_Hole_Locy = -1*(SVDiameter/2+GEM_Hole_Diameter);
   G4double GEM_Hole_Maxx = +1*(SVDiameter/2+GEM_Hole_Diameter);
   G4double GEM_Hole_Maxy = +1*(SVDiameter/2+GEM_Hole_Diameter);
   G4double GEM_Hole_Startx = GEM_Hole_Locx;
   while (GEM_Hole_Locy <= GEM_Hole_Maxy){
      GEM_Modifier_Box = new G4SubtractionSolid("GEM_Modifier_Box", GEM_Modifier_Box, GEM_Hole_Cylinder,0,
          G4ThreeVector(GEM_Hole_Locx,GEM_Hole_Locy,0.));

      // Increment The Current X Position
      GEM_Hole_Locx += GEM_Hole_Pitch;
      if(GEM_Hole_Locx > GEM_Hole_Maxx){
         GEM_Hole_Locx = GEM_Hole_Startx;
         // Increase Current Y-Location
         GEM_Hole_Locy += GEM_Hole_Pitch;
      }
      GEM_Hole_ID++;
   }

   G4LogicalVolume* GEMModifierLogical = new G4LogicalVolume(GEM_Modifier_Box,
                                    a150,
                                    "GEMModifierLogical");
```

```
    GEMModifierPhysical = new G4PVPlacement(0,
                  G4ThreeVector(0,0,(A150_Bottom_Thickness + SignalPad_Thickness + LowerInsulator_Thickness +
                      GEM_Insulator_Thickness + 2*GEM_Conductor_Thickness + A150_Extra_Modifier/2 - GEM_Height/2)),
                  GEMModifierLogical,
                  "GEMModifier_Physical",
                  A150BaseLogical,
                  false,
                  0,
                  false);
 }

//////////////////////////////////////////////////////////////////////
// Upper Insulator (Rexolite)

// Insulator Box
G4Box* UpperInsulatorSolid = new G4Box("UpperInsulator_Box", // Name
         GEM_Length/2, GEM_Width/2, SVDiameter/2); // Half lengths


G4LogicalVolume* UpperInsulatorLogical = new G4LogicalVolume(UpperInsulatorSolid,
                                         rexolite,
                                    "UpperInsulatorLogical");

UpperInsulatorPhysical = new G4PVPlacement(0,
           G4ThreeVector(0,0,(A150_Bottom_Thickness + SignalPad_Thickness + LowerInsulator_Thickness + GEM_Insulator_Thickness +
               2*GEM_Conductor_Thickness + A150_Extra_Modifier + SVDiameter/2 - GEM_Height/2)),
           UpperInsulatorLogical,
           "UpperInsulatorPhysical",
               A150BaseLogical,
           false,
           0,
           false);

// Sensitive Volume Cylinder
G4VSolid* UpperInsulator_SVCylinder = new G4Tubs("UpperInsulator_SVCylinder",0.,SVDiameter/2,SVDiameter/2,0.,360.*deg);

G4LogicalVolume* UpperInsulator_SVCylinder_Logical = new G4LogicalVolume(UpperInsulator_SVCylinder,
                                         tep_gas,
                                    "UpperInsulator_SVCylinder_Logical");

UpperInsulator_SVCylinder_Physical = new G4PVPlacement(0,
           G4ThreeVector(0,0,0),
           UpperInsulator_SVCylinder_Logical,
           "UpperInsulator_SVCylinder_Physical",
               UpperInsulatorLogical,
           false,
           0,
           false);

//////////////////////////////////////////////////////////////////////
// Output Geometry Information
SVCylinderMass = UpperInsulator_SVCylinder_Logical->GetMass();
G4cout  << "\n-------------------- START Geometry Details ----------------------------"
      << "\nGEM Height: " << GEM_Height/cm << " cm"
      << "\nGEM Width: " << GEM_Width/cm << " cm"
      << "\nGEM Length: " << GEM_Length/cm << " cm"
      << "\nTOP A150: " << A150_Top_Thickness/cm << " cm"
      << "\nBOTTOM A150: " << A150_Bottom_Thickness/cm << " cm"
      << "\nSignal Pad: " << SignalPad_Thickness/mm << " mm"
      << "\nLower Insulator: " << LowerInsulator_Thickness/mm << " mm"
      << "\nGEM Diameter: " << GEM_Hole_Diameter/mm << " mm"
      << "\nGEM Pitch: " << GEM_Hole_Pitch/mm << " mm"
      << "\nGEM Modifier Thickness: " << A150_Extra_Modifier/mm << " mm"
      << "\nDetector Angle: " << DetectorAngle/deg << " degrees"
      << "\nSensitive Volume Mass: " << SVCylinderMass/kg << " kg"
      << "\n-------------------- END Geometry Details ----------------------------\n"
      << G4endl;
//////////////////////////////////////////////////////////////////////
// Visualisation attributes
// A150
G4VisAttributes* A150Attributes = new G4VisAttributes(G4Colour(1.0,1.0,1.0,0.5));
A150Attributes->SetForceSolid(true);
A150BaseLogical->SetVisAttributes(A150Attributes);
// SignalPad
G4VisAttributes* SignalPadAttributes = new G4VisAttributes(G4Colour(1.0,0.,1.0,1.0));
SignalPadAttributes->SetForceSolid(true);
SignalPadLogical->SetVisAttributes(SignalPadAttributes);
// Insulator
G4VisAttributes* InsulatorAttributes = new G4VisAttributes(G4Colour(0.,1.0,0.,1.0));
InsulatorAttributes->SetForceSolid(true);
LowerInsulatorLogical->SetVisAttributes(InsulatorAttributes);
UpperInsulatorLogical->SetVisAttributes(InsulatorAttributes);
```

```
  // GEM Holes & Sensitive Volume
  G4VisAttributes* GEMHoleAttributes = new G4VisAttributes(G4Colour(1.0,0.,0.,1.0));
  GEMHoleAttributes->SetForceSolid(true);
  GEM_Hole_Cylinder_Logical->SetVisAttributes(GEMHoleAttributes);
  LowerInsulator_Cylinder_Logical->SetVisAttributes(GEMHoleAttributes);
  UpperInsulator_SVCylinder_Logical->SetVisAttributes(GEMHoleAttributes);

  //////////////////////////////////////////////////////////////////////////

  // Return world volume
  return fpWorldPhysical;
}

void DetectorConstruction::SetDetectorAngle(G4double val)
{
  // change Detector Rotational Angle
  DetectorAngle = val;
}

void DetectorConstruction::SetModifierThickness(G4double val)
{
  // change Detector Rotational Angle
  A150_Extra_Modifier = val;
}

void DetectorConstruction::UpdateGeometry()
{
   G4RunManager::GetRunManager()->DefineWorldVolume(SetupGeometry());
}
```

DetectorConstructionMessenger.cc

```
// ********************************************************************
// The following messenger module passes variables into the simulation
// without having to re-compile the code. Used for changing detector
// angle and moderator thickness.
// Simulation by: Andrei Hanu at McMaster University
// ********************************************************************
#include "DetectorConstruction.hh"
#include "DetectorConstructionMessenger.hh"

#include "G4UIdirectory.hh"
#include "G4UIcmdWithAString.hh"
#include "G4UIcmdWithAnInteger.hh"
#include "G4UIcmdWithADoubleAndUnit.hh"
#include "G4UIcmdWithoutParameter.hh"

DetectorConstructionMessenger::DetectorConstructionMessenger(DetectorConstruction* det)
:THGEMDetector(det)
{
   THGEMDir = new G4UIdirectory("/THGEM/");
   THGEMDir->SetGuidance("UI commands of THGEM");

   detDir = new G4UIdirectory("/N03/det/");
   detDir->SetGuidance("detector control");

   DetectorAngleCmd = new G4UIcmdWithADoubleAndUnit("/THGEM/det/SetDetectorAngle",this);
   DetectorAngleCmd->SetGuidance("Set angle of the detector inside beam");
   DetectorAngleCmd->SetParameterName("angle",false);
   DetectorAngleCmd->SetRange("angle>=0. && angle<180.");
   DetectorAngleCmd->SetDefaultValue(0.);
   DetectorAngleCmd->SetDefaultUnit("deg");
   DetectorAngleCmd->AvailableForStates(G4State_PreInit,G4State_Idle);

   DetectorModfierCmd = new G4UIcmdWithADoubleAndUnit("/THGEM/det/SetModifierThickness",this);
   DetectorModfierCmd->SetGuidance("Set thickness of the modifier inside");
   DetectorModfierCmd->SetParameterName("thickness",false);
   DetectorModfierCmd->SetRange("thickness>=0. ");
   DetectorModfierCmd->SetDefaultValue(0.);
   DetectorModfierCmd->SetDefaultUnit("mm");
   DetectorModfierCmd->AvailableForStates(G4State_PreInit,G4State_Idle);

   UpdateCmd = new G4UIcmdWithoutParameter("/THGEM/det/update",this);
   UpdateCmd->SetGuidance("Update THGEM geometry.");
   UpdateCmd->SetGuidance("This command MUST be applied before \"beamOn\" ");
   UpdateCmd->SetGuidance("if you changed geometrical value(s).");
   UpdateCmd->AvailableForStates(G4State_Idle);
}
```

```
DetectorConstructionMessenger::~DetectorConstructionMessenger()
{
   delete DetectorAngleCmd;
   delete DetectorModfierCmd;
   delete UpdateCmd;
}

void DetectorConstructionMessenger::SetNewValue(G4UIcommand* command,G4String newValue)
{
   if( command == DetectorAngleCmd )
   {
      G4cout  << "\nNew Detector Angle: " << newValue << " " << G4endl;
      THGEMDetector->SetDetectorAngle(DetectorAngleCmd->GetNewDoubleValue(newValue));
   }

   if( command == DetectorModfierCmd )
   {
      G4cout  << "\nNew Modifier Thickness: " << newValue << " " << G4endl;
      THGEMDetector->SetModifierThickness(DetectorModfierCmd->GetNewDoubleValue(newValue));
   }

   if( command == UpdateCmd )
   {
      THGEMDetector->UpdateGeometry();
   }
}
```

EventAction.cc

```
// ********************************************************************
// Module which runs at the beginning and end of each event.
// Simulation by: Andrei Hanu at McMaster University
// ********************************************************************
#include "EventAction.hh"
#include "DetectorConstruction.hh"
#include "RunAction.hh"
#include "math.h"
#include "G4Event.hh"
#include "G4TrajectoryContainer.hh"
#include "G4Trajectory.hh"
#include "G4VVisManager.hh"

EventAction::EventAction(DetectorConstruction* detector, RunAction* runAct)
:detector(detector), runAct(runAct)
{
   printModulo = 100000;
}

EventAction::~EventAction()
{
}

void EventAction::AddEnergy(G4double dE)
{
   //Accumulate the Energy Deposited
   EDepPerEvent += dE;
}

void EventAction::BeginOfEventAction(const G4Event* evt)
{
   // Initialize The Total Energy Deposited Per Event
   EDepPerEvent = 0.;

   // Get Event Number
   evtNb = evt->GetEventID();

}

void EventAction::EndOfEventAction(const G4Event* evt)
{
   if(EDepPerEvent > 0.) {
      runAct->fillPerEvent(EDepPerEvent);
   }

   if (evtNb%printModulo == 0){
      runAct->calculateDPUF(evtNb);
   }
}
```

PrimaryGeneratorAction.cc

```
// ********************************************************************
// Code which selects the General Particle Source (GPS) for entering
// source information.
// Simulation by: Andrei Hanu at McMaster University
// ********************************************************************
#include "PrimaryGeneratorAction.hh"
#include "DetectorConstruction.hh"

#include "G4Event.hh"
#include "G4ParticleDefinition.hh"
#include "G4GeneralParticleSource.hh"
#include "G4ParticleGun.hh"
#include "G4ParticleTable.hh"
#include "Randomize.hh"

PrimaryGeneratorAction::PrimaryGeneratorAction()
{
  particleGun = new G4GeneralParticleSource();
}

PrimaryGeneratorAction::~PrimaryGeneratorAction()
{
  delete particleGun;
}

void PrimaryGeneratorAction::GeneratePrimaries(G4Event* anEvent)
{
  particleGun->GeneratePrimaryVertex(anEvent);
}
```

RunAction.cc

```
// ********************************************************************
// Module which runs at the beginning and end of each run.
// Simulation by: Andrei Hanu at McMaster University
// ********************************************************************

#include "RunAction.hh"

#include "G4Run.hh"
#include "G4RunManager.hh"
#include "G4UnitsTable.hh"
#include "DetectorConstruction.hh"
#include "PrimaryGeneratorAction.hh"
#include "G4THitsMap.hh"
#include "time.h"
#include "G4UIcommand.hh"

RunAction::RunAction(DetectorConstruction* detector, PrimaryGeneratorAction* kin)
:detector(detector),Kin(kin)
{
}

RunAction::~RunAction()
{
}

void RunAction::BeginOfRunAction(const G4Run* aRun)
{
  G4cout  << "\n----------------------------------------------------"
         << "\nStart of Run " << aRun->GetRunID()
         << "\n----------------------------------------------------"
         << G4endl;

  // save Rndm status
  long seeds[2];
  time_t systime = time(NULL);
  seeds[0] = (long) systime;
  seeds[1] = (long) (systime*G4UniformRand());
  CLHEP::HepRandom::setTheSeeds(seeds);

  // Open a new CSV file for writing
  outputFile = G4UIcommand::ConvertToString(systime*G4UniformRand()) +
      G4UIcommand::ConvertToString((G4UniformRand()*ceil(G4UniformRand()*1000+100)))+".csv";
  pFile = fopen (outputFile,"w");

  // Zero Total Energy & Number of Interacting Particles
```

```
  //numInteractingParticles = 0;
  //totalEnergy = 0.;
}

void RunAction::fillPerEvent(G4double EAbs)
{
  if (EAbs > 0.)
  {
   // Increment the total Energy
   totalEnergy += EAbs;

   // Increment The Number of Interacting Particles
   numInteractingParticles++;

   // Output Energy To File
   std::ofstream outFile(outputFile,std::ios::out|std::ios::app);
   outFile << EAbs/eV<<";"<< "0" <<G4endl;
  }
}

void RunAction::calculateDPUF(G4int evtNb)
{
   fluence = evtNb/(pow(0.6,2)*3.14159265);
   dose = (totalEnergy/joule)/(detector->Mass_of_SV()/kg);
   DPUF = (dose/(fluence*10000))/0.000000000000001; // in fGy*m^2
   DPUF_uncertainty = DPUF*sqrt(numInteractingParticles)/numInteractingParticles;
   G4cout << "\nEvent: " << evtNb << " --> Dose Per Unit Fluence: " << DPUF << " +/- " << DPUF_uncertainty << " fGy*m^2" << G4endl;
}

void RunAction::EndOfRunAction(const G4Run* aRun)
{
  // Calculate The DPUF at the end of run
  calculateDPUF(aRun->GetNumberOfEvent());

  //Source Information
  G4double Ekin = Kin->GetGPS()->GetParticleEnergy();
  G4cout  << "\n---------------------- Run " << aRun->GetRunID() << " Information ------------------------------"
        << "\nIncident Particle: " << Kin->GetGPS()->GetParticleDefinition()->GetParticleName()
        << "\nIncident Energy: " << Ekin/keV << " keV"
        << "\nDetector Angle: " << (detector->GetDetectorAngle()/deg)<< " degree"
        << "\nTotal Energy Deposited in Sensitive Volume: " << totalEnergy/joule << " Joules"
        << "\n# of Interacting Particles: " << numInteractingParticles
        << "\n\nDose Per Unit Fluence: " << DPUF << " +/- " << DPUF_uncertainty << " fGy*m^2" << G4endl;

  // Close the current output
  fclose(pFile);
  // Rename the Output File
  G4String outputFileRename = G4UIcommand::ConvertToString(Ekin/keV) + "keV_" +
      G4UIcommand::ConvertToString(detector->GetDetectorAngle()/deg) + "deg_RUN_" + G4UIcommand::ConvertToString(aRun->GetRunID()) +
      "_Particles_"+G4UIcommand::ConvertToString(aRun->GetNumberOfEvent()) + "_" + outputFile;
  if ( rename(outputFile,outputFileRename) == 0 )
   G4cout  << "\nOutput File: " << outputFileRename
        << "\n---------------------- END Run " << aRun->GetRunID() << " Information ------------------------------\n"
        << G4endl;
  else
   G4cout  << "\nOutput File: " << outputFile
        << "\n---------------------- END Run " << aRun->GetRunID() << " Information ------------------------------\n"
        << G4endl;
}
```

SteppingAction.cc

```
// ********************************************************************
// Module which runs during each particle step.
// Simulation by: Andrei Hanu at McMaster University
// ********************************************************************

#include "SteppingAction.hh"

#include "DetectorConstruction.hh"
#include "EventAction.hh"
#include "RunAction.hh"
#include "G4Gamma.hh"
#include "G4Step.hh"

SteppingAction::SteppingAction(DetectorConstruction* det,
                               EventAction* evt)
:detector(det), eventaction(evt)
{ }
```

```
SteppingAction::~SteppingAction()
{ }

void SteppingAction::UserSteppingAction(const G4Step* aStep)
{
   G4StepPoint* point1 = aStep->GetPreStepPoint();
   G4StepPoint* point2 = aStep->GetPostStepPoint();

   // G4 Touchable Info
   G4TouchableHandle touch1 = point1->GetTouchableHandle();
   G4TouchableHandle touch2 = point2->GetTouchableHandle();

   // Current Volume
   G4VPhysicalVolume* volume1 = touch1->GetVolume();
   G4VPhysicalVolume* volume2 = touch2->GetVolume();

   // Energy Deposited
   G4double eDeposit = aStep->GetTotalEnergyDeposit();

   // Adding the Delta Energy
   if (volume1 == detector->GetAbsorber() && eDeposit > 0.){
      eventaction->AddEnergy(eDeposit);
   }
}
```

run.mac

```
#########################################################################
# Macro file used as input to the THGEM simulation. Input parameters such
# as detector angle, modifier thickness, particle type, energy, number of
# particles, are controlled here.
#
# Simulation by: Andrei Hanu at McMaster University
#########################################################################

# Detector Configuration
/THGEM/det/SetDetectorAngle 0 deg
/THGEM/det/SetModifierThickness 2 mm
/THGEM/det/update

# Create a Plane Source
/gps/pos/type Plane
/gps/pos/shape Circle
/gps/pos/radius 6. mm
/gps/pos/centre 0. 0. +10. cm

# Energy 1
/gps/particle neutron
/gps/energy 1000 keV
/run/beamOn 2000000000
```

References

Alexeev, M. *et al.* (2010). Micropattern gaseous photon detectors for Cherenkov imaging counters. *Nuclear Instruments and Methods in Physics Research Section A: Accelerators, Spectrometers, Detectors and Associated Equipment*, **623**(1), 129 – 131.

Anjomani, Z., Hanu, A., Prestwich, W., and Byun, S. (2013). Optimization of a THick Gas Electron multiplier-based multielement microdosimetric detector design using Geant4. *Nuclear Instruments and Methods in Physics Research Section A: Accelerators, Spectrometers, Detectors and Associated Equipment*.

Bachmann, S., Kappler, S., Ketzer, B., Müller, T., Ropelewski, L., Sauli, F., and Schulte, E. (2002). High rate X-ray imaging using multi-GEM detectors with a novel readout design. *Nuclear Instruments and Methods in Physics Research Section A: Accelerators, Spectrometers, Detectors and Associated Equipment*, **478**(1-2), 104 – 108.

Bamberger, A., Desch, K., Renz, U., Titov, M., Vlasov, N., Wienemann, P., and Zwerger, A. (2007). Readout of GEM detectors using the Medipix2 CMOS pixel chip. *Nuclear Instruments and Methods in Physics Research Section A: Accelerators, Spectrometers, Detectors and Associated Equipment*, **573**(3), 361 – 370.

Barbosa, A. F. (1996). Use of a multilayer printed circuit board as the position sensing electrode in an MWPC. *Nuclear Instruments and Methods in Physics Research Section A: Accelerators, Spectrometers, Detectors and Associated Equipment*, **371**(3), 368 – 374.

Belau, E., Klanner, R., Lutz, G., Neugebauer, E., Seebrunner, H., Wylie, A., Böhringer, T., Hubbeling, L., Weilhammer, P., Kemmer, J., *et al.* (1983). Charge collection in silicon strip detectors. *Nuclear Instruments and Methods in Physics Research*, **214**(2), 253–260.

Bellazzini, R., Spandre, G., Minuti, M., Baldini, L., Brez, A., Latronico, L., Omodei, N., Razzano, M., Massai, M., Pesce-Rollins, M., SgrÃş, C., Costa, E., Soffitta, P., Sipila, H., and Lempinen, E. (2007). A sealed Gas Pixel Detector for X-ray

astronomy. *Nuclear Instruments and Methods in Physics Research Section A: Accelerators, Spectrometers, Detectors and Associated Equipment*, **579**(2), 853 – 858.

Bock, R. K. and Vasilescu, A. (1998). *The particle detector briefbook*. Springer.

Breskin, A., Buzulutskov, A., and Chechik, R. (2002). GEM photomultiplier operation in CF4. *Nuclear Instruments and Methods in Physics Research Section A: Accelerators, Spectrometers, Detectors and Associated Equipment*, **483**(3), 670 – 675.

Breskin, A., Alon, R., Cortesi, M., Chechik, R., Miyamoto, J., Dangendorf, V., Maia, J., and Santos, J. D. (2009). A concise review on THGEM detectors. *Nuclear Instruments and Methods in Physics Research Section A: Accelerators, Spectrometers, Detectors and Associated Equipment*, **598**(1), 107 – 111.

Breskin, A., Cortesi, M., Alon, R., Miyamoto, J., Peskov, V., Bartesaghi, G., Chechik, R., Dangendorf, V., Maia, J., and dos Santos, J. (2010). The THGEM: A thick robust gaseous electron multiplier for radiation detectors. *Nuclear Instruments and Methods in Physics Research Section A: Accelerators, Spectrometers, Detectors and Associated Equipment*, **623**(1), 132 – 134.

Bressan, A., Labbé, J., Pagano, P., Ropelewski, L., and Sauli, F. (1999). Beam tests of the gas electron multiplier. *Nuclear Instruments and Methods in Physics Research Section A: Accelerators, Spectrometers, Detectors and Associated Equipment*, **425**(1), 262–276.

Byun, S., Spirou, G., Hanu, A., Prestwich, W., and Waker, A. (2009). Simulation and First Test of a Microdosimetric Detector Based on a Thick Gas Electron Multiplier. *Nuclear Science, IEEE Transactions on*, **56**(3), 1108–1113.

Charpak, G., Bouclier, R., Bressani, T., Favier, J., and Zupančič, Č. (1968). The use of multiwire proportional counters to select and localize charged particles. *Nuclear Instruments and Methods*, **62**(3), 262–268.

Chechik, R., Breskin, A., Shalem, C., and Mörmann, D. (2004). Thick GEM-like hole multipliers: properties and possible applications. *Nuclear Instruments and Methods in Physics Research Section A: Accelerators, Spectrometers, Detectors and Associated Equipment*, **535**(1), 303–308.

Corradi, G., Murtas, F., and Tagnani, D. (2007). A novel High-Voltage System for a triple GEM detector. *Nuclear Instruments and Methods in Physics Research Section A: Accelerators, Spectrometers, Detectors and Associated Equipment*, **572**(1), 96–97.

Cortesi, M., Alon, R., Chechik, R., Breskin, A., Vartsky, D., and Dangendorf, V. (2007). Investigations of a THGEM-based imaging detector. *Journal of Instrumentation*, **2**(09), P09002.

Davidson, D., Fröjdh, C., O'Shea, V., Nilsson, H.-E., and Rahman, M. (2003). Limitations to flat-field correction methods when using an X-ray spectrum. *Nuclear Instruments and Methods in Physics Research Section A: Accelerators, Spectrometers, Detectors and Associated Equipment*, **509**(1), 146–150.

Guedes, G., Breskin, A., Chechik, R., Vartsky, D., Bar, D., Barbosa, A., and Marinho, P. (2003). Two-dimensional GEM imaging detector with delay-line readout. *Nuclear Instruments and Methods in Physics Research Section A: Accelerators, Spectrometers, Detectors and Associated Equipment*, **513**(3), 473 – 483.

Hanu, A., Byun, S., and Prestwich, W. (2010). A Monte Carlo simulation of the microdosimetric response for thick gas electron multiplier. *Nuclear Instruments and Methods in Physics Research Section A: Accelerators, Spectrometers, Detectors and Associated Equipment*, **622**(1), 270–275.

Heitler, W. (1954). *The quantum theory of radiation*. Courier Dover Publications.

Ivaniouchenkov, Y., Fonte, P., Peskov, V., and Ramsey, B. (1999). Breakdown limit studies in high-rate gaseous detectors. *Nuclear Instruments and Methods in Physics Research Section A: Accelerators, Spectrometers, Detectors and Associated Equipment*, **422**(1), 300–304.

Kaminski, J., Kappler, S., Ledermann, B., Muller, T., and Ronan, M. (2005). Study of various anode pad readout geometries in a GEM-TPC. *Nuclear Science, IEEE Transactions on*, **52**(6), 2900–2906.

Kemmochi, M. (1976). Measurement of W-values for alpha particles in tissue equivalent gases. *Health Physics*, **30**(6), 439–446.

Klyachko, A., Friesel, D., Kline, C., Liechty, J., Nichiporov, D., and Solberg, K. (2011). Dose imaging detectors for radiotherapy based on gas electron multipliers. *Nuclear Instruments and Methods in Physics Research Section A: Accelerators, Spectrometers, Detectors and Associated Equipment*, **628**(1), 434–439.

Krajcar-Bronić, I. and Srdoč, D. (1994). A comparison of calculated and measured W values in tissue-equivalent gas mixtures. *Radiation research*, **137**(1), 18–24.

Lauer, T. (2002). Deconvolution with a spatially-variant PSF. In *Astronomical Telescopes and Instrumentation*, pages 167–173. International Society for Optics and Photonics.

Marinho, P., Barbosa, A., and Guedes, G. (2005). Using a multilayer printed circuit board as position sensing electrode in a triple-GEM detector. *Nuclear Science, IEEE Transactions on*, **52**(6), 2917–2922.

Millman, J. and Taub, H. (1956). *Pulse and Digital Circuits*. McGraw-Hill Electrical and Electronic Engineering Series. McGraw-Hill.

Oed, A. (1988). Position-sensitive detector with microstrip anode for electron multiplication with gases. *Nuclear Instruments and Methods in Physics Research Section A: Accelerators, Spectrometers, Detectors and Associated Equipment*, **263**(2), 351–359.

Oliveira, R., Peskov, V., Pietropaolo, F., and Picchi, P. (2007). First tests of thick GEMs with electrodes made of a resistive kapton. *Nuclear Instruments and Methods in Physics Research Section A: Accelerators, Spectrometers, Detectors and Associated Equipment*, **576**(2-3), 362 – 366.

Orchard, G. M. (2010). *Development of a Thick Gas Electron Multiplier Detector for Microdosimetry*. Ph.D. thesis, McMaster University.

Periale, L., Peskov, V., Carlson, P., Francke, T., Pavlopoulos, P., Picchi, P., and Pietropaolo, F. (2002). Detection of the primary scintillation light from dense Ar, Kr and Xe with novel photosensitive gaseous detectors. *Nuclear Instruments and Methods in Physics Research Section A: Accelerators, Spectrometers, Detectors and Associated Equipment*, **478**(1), 377–383.

Peskov, V. and Fonte, P. (2009). Research on discharges in micropattern and small gap gaseous detectors. *arXiv preprint arXiv:0911.0463*.

Petrov, A., Amirov, R., and Samoylov, I. (2009). On the Nature of Copper Cathode Erosion in Negative Corona Discharge. *Plasma Science, IEEE Transactions on*, **37**(7), 1146–1149.

Raether, H. (1964). *Electron avalanches and breakdown in gases*. Butterworths London.

Richardson, W. H. (1972). Bayesian-based iterative method of image restoration. *JOSA*, **62**(1), 55–59.

Sauli, F. (1997). GEM: A new concept for electron amplification in gas detectors. *Nuclear Instruments and Methods in Physics Research Section A: Accelerators, Spectrometers, Detectors and Associated Equipment*, **386**(2), 531–534.

Sauli, F. (1998). Gas detectors: Recent developments and future perspectives. *Nuclear Instruments and Methods in Physics Research Section A: Accelerators, Spectrometers, Detectors and Associated Equipment*, **419**(2-3), 189 – 201.

Schmitz, J. (1992). Results on Monte Carlo simulations of a microstrip gas counter. *Nuclear Instruments and Methods in Physics Research Section A: Accelerators, Spectrometers, Detectors and Associated Equipment*, **323**(3), 638–644.

Seibert, J. A., Boone, J. M., and Lindfors, K. K. (1998). Flat-field correction technique for digital detectors. In *Medical Imaging*, pages 348–354. International Society for Optics and Photonics.

Shalem, C., Chechik, R., Breskin, A., and Michaeli, K. (2006). Advances in Thick GEM-like gaseous electron multipliers. Part I: atmospheric pressure operation. *Nuclear Instruments and Methods in Physics Research Section A: Accelerators, Spectrometers, Detectors and Associated Equipment*, **558**(2), 475–489.

Sibarita, J.-B. (2005). Deconvolution microscopy. In *Microscopy Techniques*, pages 201–243. Springer.

Sobottka, S. E. and Williams, M. B. (1988). Delay line readout of microchannel plates. *Nuclear Science, IEEE Transactions on*, **35**(1), 348–351.

Uchida, T. (2008). Hardware-based TCP processor for gigabit ethernet. *Nuclear Science, IEEE Transactions on*, **55**(3), 1631–1637.

VMEbus International Trade Association (2008). *FPGA Mezzanine Card (FMC) standard*. New York, NY.

Zhou, Y., Li, C., and Sun, Y. (2009). Study of delay-line readout for GEM detector. *Nuclear Instruments and Methods in Physics Research Section A: Accelerators, Spectrometers, Detectors and Associated Equipment*, **604**(1), 71–76.

Ziegler, M., Sievers, P., and Straumann, U. (2001). A triple GEM detector with two-dimensional readout. *Nuclear Instruments and Methods in Physics Research Section A: Accelerators, Spectrometers, Detectors and Associated Equipment*, **471**(12), 260 – 263.